EFFECT OF CONDUCTIVE NETWORK FORMATION AND PARTICLE MORPHOLOGY ON THE ELECTRICAL PROPERTIES OF COMPOSITES

A Dissertation
Presented to
The Academic Faculty

by

Morgan R. Watt

In Partial Fulfillment
of the Requirements for the Degree
Doctor of Philosophy in the
School of Materials Science and Engineering

Georgia Institute of Technology
December 2020

EFFECT OF CONDUCTIVE NETWORK FORMATION AND PARTICLE MORPHOLOGY ON THE ELECTRICAL PROPERTIES OF COMPOSITES

Approved by:

Dr. Rosario A. Gerhardt, Advisor
School of Materials Science and Engineering
Georgia Institute of Technology

Dr. Satish Kumar
School of Materials Science and Engineering
Georgia Institute of Technology

Dr. Kyriaki Kalaitzidou
School of Mechanical Engineering
Georgia Institute of Technology

Dr. Jud Ready
School of Materials Science and Engineering
Georgia Institute of Technology

Dr. Jonathan Colton
School of Mechanical Engineering
Georgia Institute of Technology

Date Approved: November 30, 2020

ACKNOWLEDGMENTS

I would like to express my appreciation and sincere thanks to my advisor, Dr. Gerhardt, for her guidance and support throughout my PhD. Her support, encouragement, and advise was invaluable. I want to express my gratitude to my committee members to Dr. Kalaitzidou, Dr. Colton, Dr. Kumar, and Dr. Ready for all their knowledge, support, and advice throughout this thesis process.

I would like to acknowledge the funding and financial support from the National Science Foundation via DMR- 1207323, GTRC-IP Grant, and a Graduate Assistance in Areas of National Need (GAANN) Fellowship for this project.

I would like to thank Dr. Chaitanya Deo for use of his SPS and Dr. Kalaitzidou for use of her melt mixer. I also want to thank Dr. Jan Ilavsky for operating the USAXS/SAXS/WAXS equipment at the 9ID-C beamline at ANL and analysis of the resultant data. I want to acknowledge David Tavakoli for collecting the XRD data, along with Dr. Chanchal Ghosh and Dr. Steve Jett at the Center of Integrated Nanotechnology (CINT) for sample analysis using TEM.

I want to acknowledge my fellow graduate students Thomas Rudzik, Ning Xia, Youngho Jin, and Sivaramakrishna Sethuraman for training, support, and helping make graduate school an enjoyable experience. I also want to thank Gillian Brown for SEM analysis.

Finally, I would like to thank my parents, Susan and David Watt, and my friends for their unwavering support throughout my education. I never would have made it without them.

TABLE OF CONTENTS

LIST OF TABLES

LIST OF FIGURES

LIST OF SYMBOLS AND ABBREVIATIONS

PMMA	Polymethymethacrylate
CNT	Carbon nanotubes
MWCNT	Multi-wall carbon nanotubes
SWCNT	Single-wall carbon nanotubes
SiC	Silicon carbide
SiC_w	Silicon carbide whiskers
mSiC	Micron- silicon carbide
nSiC	Nano- silicon carbide
SiC_{nw}	Silicon carbide nanowires
SEM	Scanning electron microscopy
TEM	Transmission electron microscopy
Vol %	Volume percent
Phr	Per hundred resin
Wt %	Weight percent
Z’	Real part of impedance
Z”	Imaginary part of impedance
Y’	Real part of admittance
Y”	Imaginary part of admittance
M’	Real part of modulus
M”	Imaginary part of modulus
E’ or ε’	Real part of dielectric permittivity
E” or ε”	Imaginary part of dielectric permittivity

Tan d or Tan δ	Tan delta
|Z|	Magnitude of Impedance
Θ	Phase Angle
R	Resistance/Resistor
L	Inductance/ Inductor
C	Capacitance/Capacitor
CPE	Constant phase element
σ	Conductivity
ρ	Resistivity
p_c	Percolation threshold
s	Exponent insensitive to microstructure (percolation)
f	Frequency
ω	Angular frequency
SPS	Spark plasma sintering
HP	Hot-pressed
I	Current
V	Voltage
nm	Nanometer
XRD	X-ray diffraction
AC	Alternating current
SAXS	Small angle X-ray scattering
USAXS	Ultra-small angle X-ray scattering
WAXS	Wide angle X-ray scattering
FTIR	Fourier transform infrared

SUMMARY

Materials are often classified into three primary groups: metals, ceramics, and polymers. Two or more dissimilar materials can be combined to create a unique composite material with the intent to incorporate the "best" properties of each individual material component and to bring new emerging characteristics. These resultant properties of composites are highly dependent on the types of materials, the processing/arrangement of these materials, and many other conditions. The most common engineered composites (e.g. reinforced concrete, fiber-reinforced polymers) are often used in structural applications. This thesis will explore the electrical properties of ceramic-polymer composites as a function of particle morphologies, composite compositions, and processing techniques. More specifically, MWCNT/PMMA, SiC/PMMA, and SiC/glass composites were fabricated to investigate the effect of particle morphology and processing steps on the conductive filler network formation and resultant microstructural and electrical properties. Understanding of these effects would allow for tailoring composites for specific applications and properties and avoid unnecessary trial and error. Equivalent circuit fitting is applied to the electrical data to quantify the individual contributions of the filler and matrix materials with knowledge of the microstructural features.

The MWCNT/PMMA composites were made using three different mixing methods (mechanical, melt, and solution) to create three different networks of conductive fillers within an insulating matrix (segregated network, distributed network, and agglomerated microstructures) and study their effect on electrical properties. Of the three mixing methods, mechanical mixing resulted in composites with the lowest percolation threshold

(0.087 phr). When the impedance data were fit to equivalent circuits, before percolation, the circuits were the same for all composites. After percolation, the circuits varied but were very similar because the same two precursors were used. The melt mixed samples were the most different due to the even dispersal of the MWCNT which allowed PMMA to have a stronger effect.

To compare the effect of the filler particle morphologies, three types of SiC (micron-sized, nano-sized, and whisker) were used to make SiC/ PMMA composites by mechanical mixing. The nano- SiC/PMMA composite formed the most defined segregated network composite and provided stable results, the highest conductivity, and a low percolation threshold of 2.35 phr. Conversely, the SiC_w /PMMA composite had the highest percolation threshold of 10 phr. Despite these differences, the SiC/PMMA composites could all be fitted by the same circuits representing them since they were made with the same type of material and processing. The differences in values of the circuit elements present directly correlates to the interaction between the matrix and filler.

Two sizes of anisotropic SiC (whisker and nanowire) were incorporated into glass matrix composites to compare the effect of anisotropic filler size. It was theorized that the smaller size of the SiC nanowires would allow it to segregate into the grain boundaries more easily and create a lower percolation threshold due to a higher aspect ratio aiding the chance of making network connections. This case proved true in that the SiC_{nw}/glass composites did have a lower percolation threshold than the SiC_w/glass composites. However, the maximum conductivity value achieved was lower for the SiC_{nw}/glass composites, and samples became too fragile to continue increasing the concentration. Circuit fitting showed that SiC_w / glass composites had a variety of circuits as concentration

increased. Conversely the SiC_{nw}/glass composites only needed two circuit models to represent their electrical properties as concentration was changed. This difference will be explained in the thesis.

During the course of this study, it was discovered that the SiC/glass samples had a strong sensitivity to the humidity at the time of testing. For SiC_w/glass composites from 0-2.5 phr, the conductivity increased with increasing humidity. For 7.5 and 12.5 phr, there was an initial sharp increase then a gradual decrease in conductivity with increasing humidity. For better understanding of the mechanism of conduction with both water and SiC contributing to the electrical paths, normalized M" and Z" were plotted together. The separate M" and Z" peaks indicated both localized and long-range conductivity.

This thesis demonstrated that very small differences in material characteristics and processing methods used to fabricate the composites may result in very different electrical properties. This study provided direct comparisons between processing methods and filler morphologies to verify the changes observed in electrical and microstructural properties. It is proven that equivalent circuit fittings correlate the contributions of the filler and matrix materials and help establish structure - processing - property relationships in conductive filler, insulating matrix composites.

1 INTRODUCTION

Composites are multi-phase systems that have a filler and a matrix material. Their properties are a combination of the properties of the individual materials plus they sometimes have extra properties not from the original materials. The overall properties of composites vary depending on multiple conditions including processing and particle morphologies which will be explored in this study. A point of interest is the change in properties with increasing concentration of filler. Minimizing the amount of filler needed to achieve desired properties may decrease production costs. Modeling the exact change as the concentration increases is also important to allow for tailoring of composites for specific applications without too much trial and error.

1.1 Percolation in Composites

Percolation occurs when a filler material spans across the matrix material to form an interconnected path through a composite. The critical concentration at which this path forms is the percolation threshold, p_c. Once the percolation threshold has been achieved, a sudden change which may cause multiple magnitudes of increase or decrease in properties such as electrical, mechanical, and thermal properties occurs [1]. An example of this is shown in Figure 1 using MWCNT as the filler and PMMA as the matrix material [2]. In this case, when a critical concentration is reached, p_c or percolation threshold, the resistivity decreases multiple orders of magnitude, indicating that the filler (MWCNT) formed a path through the matrix (PMMA) to conduct the current.

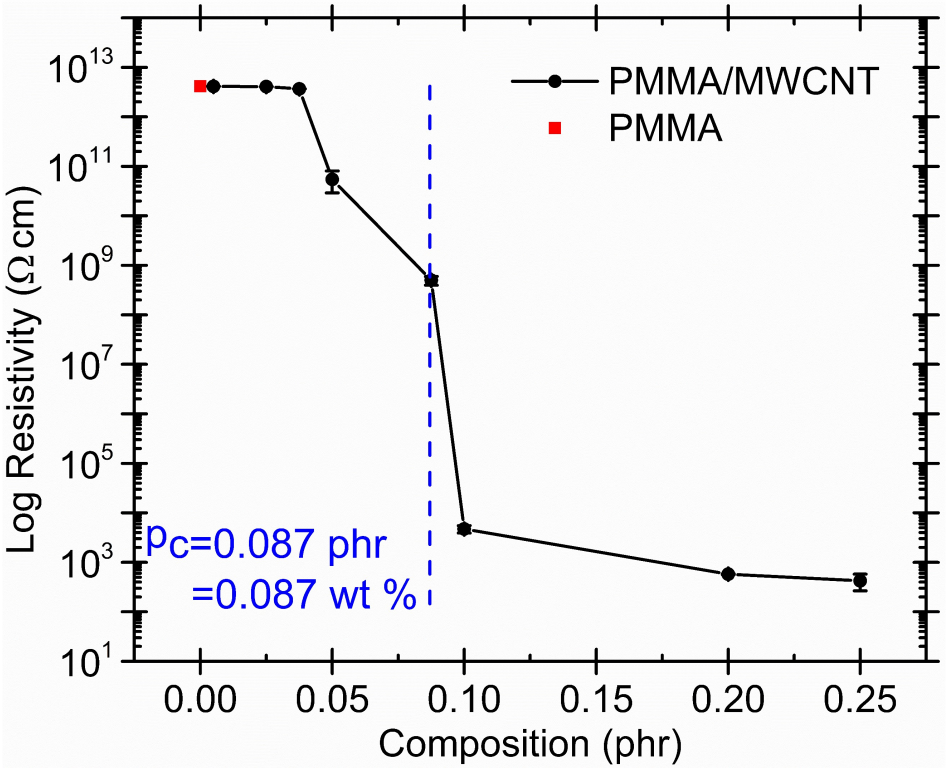

Figure 1 – Percolation of PMMA/MWCNT shown using a resistivity versus composition graph [2].

While the previously described percolation definition is good for roughly determining the percolation point by looking at percolation graphs, percolation theory is necessary to obtain a more accurate measure of p_c. Equation 1 may be used to calculate the percolation threshold by using experimental data.

$$\sigma_M \propto A(p - p_c)^s \tag{1}$$

where σ_M is the property of the mixture, A is proportionality constant, p is the probability of a site being filled, p_c is the percolation threshold, and s is an exponent that is insensitive to the microstructure [3-5].

1.2 Influence of Microstructure on Percolation Threshold

The percolation threshold, p_c, is dependent on multiple properties including the network formation of the filler across the microstructure. The type of network that forms is dependent on the processing and resultant microstructure. Three microstructures that can be obtained are dispersed, segregated, and agglomerated [6]. Dispersed microstructures are commonly made using melt mixing because it evenly distributes the filler across the matrix [6-8]. Segregated microstructures, where the filler segregates to the outside of the matrix particles, may be made using mechanical mixing [6, 9-12]. Solution mixing may create all three microstructures depending on the chemicals used [2, 6, 10, 13-23].

The percolation thresholds of composites made from the same two precursors create microstructures that are very different from each other. Figure 2 shows a summary of a large number of composites that contain MWCNT within polymer composites. This graph compares the percolation thresholds for a number of MWCNT/polymer composite systems made by using the three mixing methods, which are represented by different symbols [2, 6-9, 12, 13, 16, 18-55]. The polymers included are PMMA, polyethylene (PE), polycarbonate (PC), polypropylene (PP), polyamide (PA), and epoxy. This summary does not take into account the sizes of MWCNT or matrix particles. Across the polymer systems, it is easy to see that melt mixed samples (represented by circles) had the highest percolation thresholds [6-8, 24-41, 43-45, 54-56]. This is likely because they formed the dispersed

microstructures which separated the fillers and made it more difficult to form a percolated network. The solution mixing method (represented by upward pointing triangles) had percolation thresholds mostly below 1 wt%. As stated before, solution mixing has the highest variability in microstructures. Solution mixing commonly uses functionalization which depending on the method used may help or hinder the formation of a network [6, 10, 13-23]. Lastly, the mechanically mixed composites (represented by squares) consistently showed percolation thresholds below 0.5 wt% [6, 9-12]. The grain-like, segregated structure gathers the fillers on the edges of the matrix particles, therefore aiding the formation of a filler network [2, 10].

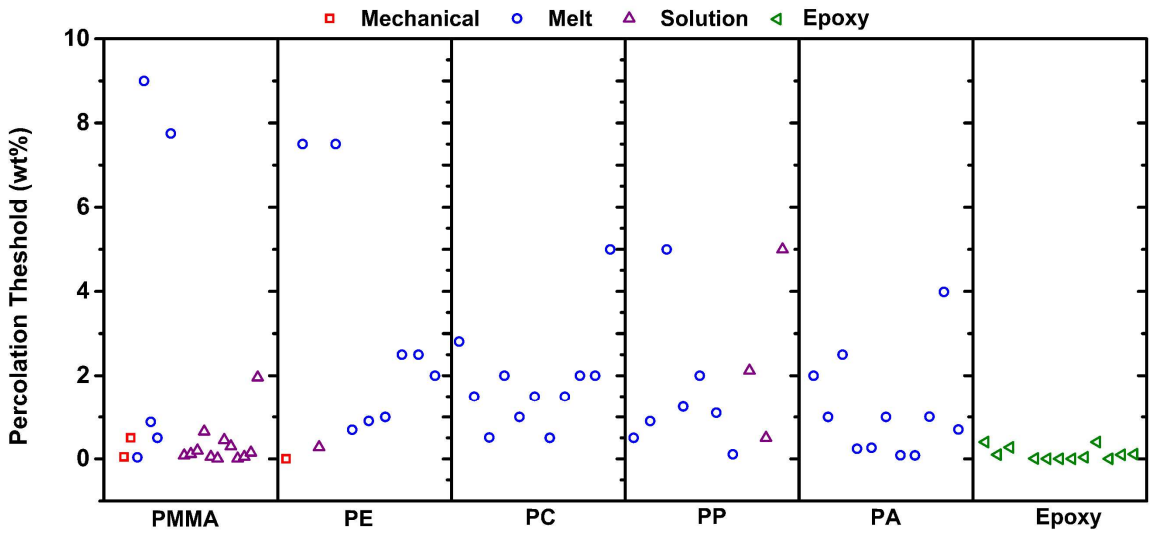

Figure 2 – Percolation thresholds for several carbon nanotube/polymer composites with different processing conditions [2, 6-9, 12, 13, 16, 18-55]

1.3 Influence of Particle Morphology on Percolation

The size and shape of the filler and matrix particles have a strong influence on the point of percolation and the reproducibility of the composite [3, 19, 57, 58]. Another influence is whether the matrix is monodisperse (similar size particles) or polydisperse (mix of different size particles) [59].

With segregated networks, the percolation threshold generally decreases with increasing ratio between matrix and filler particles ($p_c \propto 1/(r_{matrix}/r_{filler})$) [59, 60]. Figure 3 shows the resistivity versus composition for nano- and micron- indium tin oxide (ITO) filler in PMMA from the same source as this work [61, 62]. The diameters of the particles were 31 nm and 3.5 μm for the nano- and micron- sized ITO, respectively. As can be seen, the nano-ITO had a percolation threshold around 3 phr, while the micron-ITO had a threshold around 5 phr. Therefore, a smaller filler (larger ratio) was able to achieve percolation at a lower threshold [61, 62].

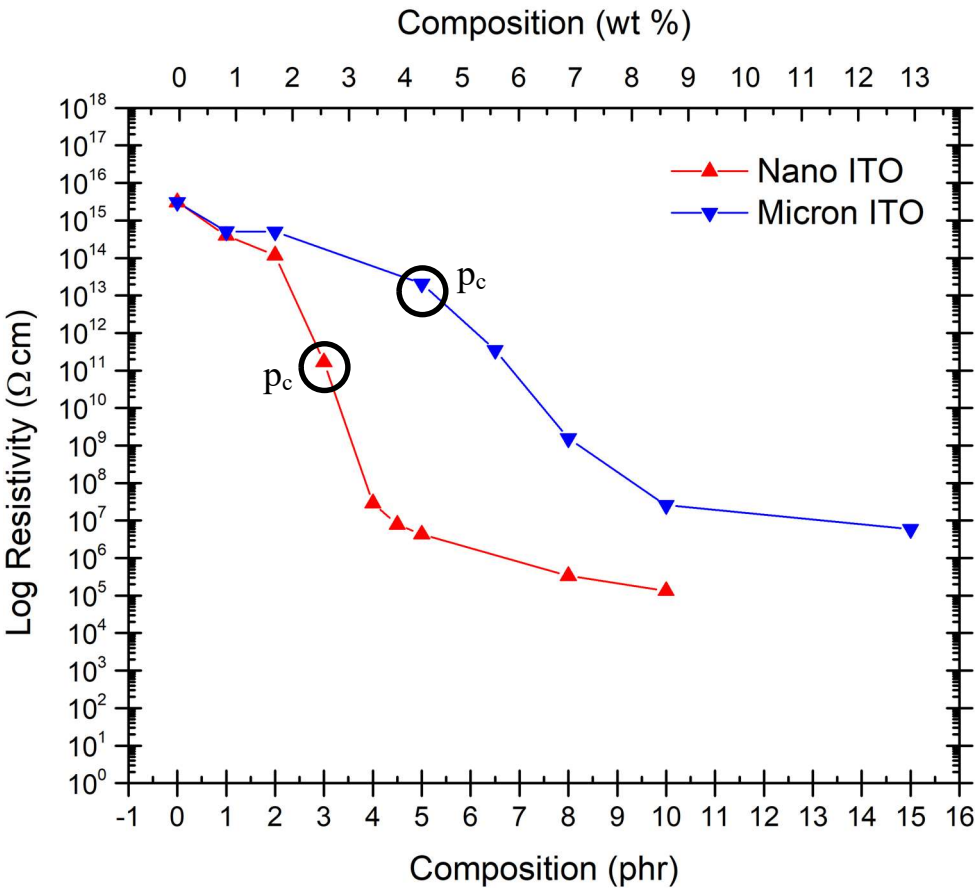

Figure 3 – Resistivity of nano- and micron- sized ITO /PMMA composites [61, 62] with estimated p_c

The shape of the particles also has a strong effect on the percolation threshold. Figure 4 shows an example of the change of percolation with graphitic filler size within PMMA composites [62, 63]. The MWCNT percolated at a lower concentration than the other four graphitic fillers, including the pure black (PB) which is about the same size or smaller in diameter than the MWCNT. The anisotropy of the MWCNT allowed the MWCNT to segregate to the boundaries easily due to their small diameter and form connections more easily due to their length.

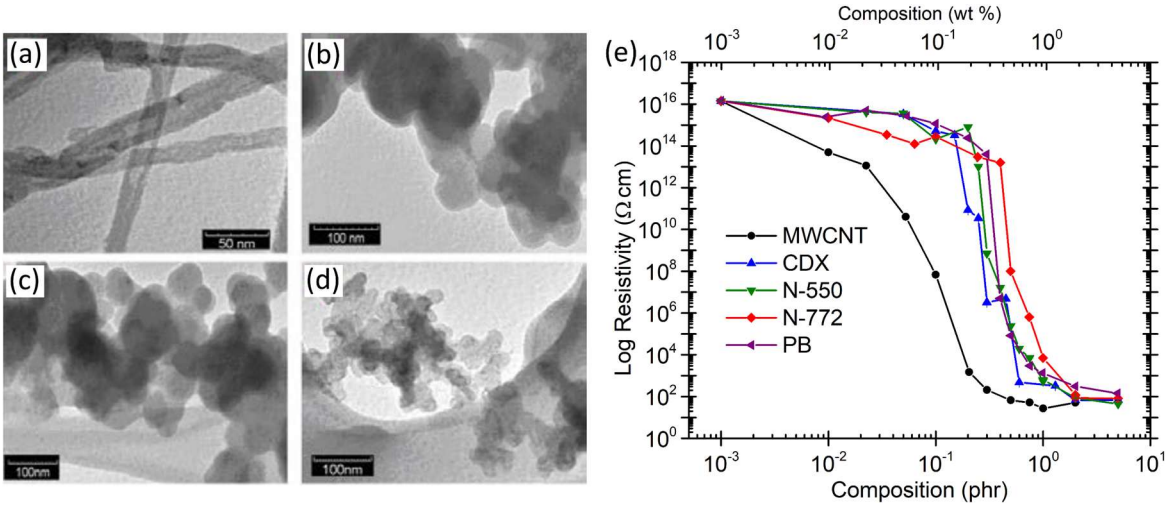

Figure 4 – TEM images of (a) multiwall carbon nanotubes, (b) N-550 carbon black, (c) N-772 carbon black and (d) pure black. (e) Resistivity of MWCNT, CDX, N-550, N-772, and pure black filler with PMMA matrix composites [62, 63].

Figure 5 shows the impedance magnitude (|Z|) versus frequency to show the difference between monodisperse and polydisperse PMMA matrix using the same filler, antimony tin oxide (ATO) [59]. Both percolate (drop in |Z| where lower frequencies show a flattening in |Z|) at the same concentration of 0.99 wt%; however, the monosize PMMA composites had a couple of magnitudes lower of |Z| and therefore lower resistance at percolation than the polydisperse PMMA composites. It also achieved lower resistance at the highest concentration shown of 9.09 wt% [59].

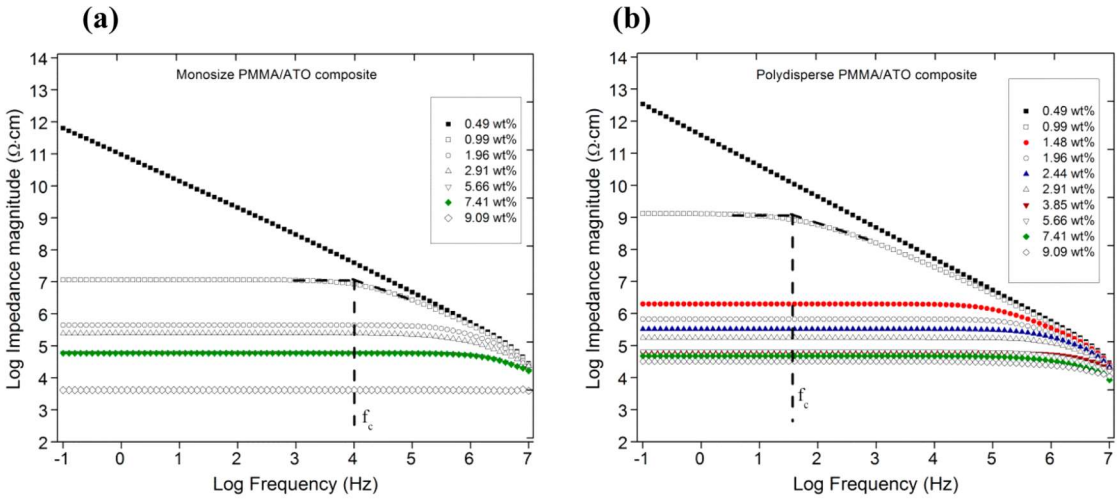

Figure 5 –Impedance magnitude versus log frequency of PMMA/ATO nanocomposites for different ATO contents using (a) monosize PMMA and (b) polydisperse PMMA [59]

1.4 AC Impedance Spectroscopy

AC impedance spectroscopy is a method that measures the current, voltage, and phase angle over a wide range of frequencies. It is strongly affected by interfaces (pores, grain-boundaries, multiphase interfaces, etc) since each has an electrical response corresponding to specific frequency ranges [64]. Therefore, as a characterization tool, measuring a range of frequencies with impedance spectroscopy allows differentiation between different microstructural features.

Impedance spectroscopy is able to characterize powders, composites, and other forms of materials without harming the samples. The complex impedance (Z*) is determined by the current (I), voltage (V), and the phase angle (Θ) between the current and

voltage over a frequency (f) range [64, 65]. Equations 2-9 show the relationship between complex impedance and the phase angle.

$$Z^* = \frac{V(\omega)}{i(\omega)} = Z' - jZ^{"} \tag{2}$$

$$V(\omega) = V_m \sin \omega t \tag{3}$$

$$i(\omega) = I_m \sin(\omega t + \theta) \tag{4}$$

$$\omega = 2\pi f \tag{5}$$

$$Z' = |Z| \cos \theta \tag{6}$$

$$Z^{"} = |Z| \sin \theta \tag{7}$$

$$\theta = \tan^{-1}\left(\frac{Z^{"}}{Z'}\right) \tag{8}$$

and

$$|Z| = \left[(Z')^2 + ((Z^{"})^2)\right]^{1/2} \tag{9}$$

where Z' and Z" are the real and imaginary part of impedance that represents the energy passing through and energy lost or stored in the material, respectively, and ω is the angular frequency. V_m and I_m are the applied AC voltage and current. j is $\sqrt{-1}$, and |Z| is the impedance magnitude [64, 65].

1.4.1 Nyquist and Bode Plots

The common way to plot impedance data is to use Nyquist (frequency implicit or complex) and Bode plots (frequency explicit). For Nyquist plots, the real and imaginary impedance are plotted on the x and y axis, respectively, with the negative values of the imaginary impedance in the first quadrant.

Bode plots are normally plotted as the real impedance (Z') or imaginary (Z") impedance versus log frequency. The impedance magnitude (|Z|) versus log frequency is another common Bode plot (as seen in Figure 5). The change in impedance magnitude with frequency can indicate capacitive (decrease with increasing frequency), inductive (increase with increasing frequency), and resistive (no change with frequency, typically at low frequencies) behavior [66]. Another Bode plot is the phase angle (Θ) versus log frequency where the angle ranges from -90° (capacitive) to 0° (resistive) to 90° (inductive). Again, the negative phase angle is typically plotted in the first quadrant.

1.4.2 Conversions into Other Dielectric Functions

Plotting complex and Bode impedance graphs only shows certain characteristics of the samples under test. To understand the full range of a material's electrical properties, permittivity (E* or ε*), dielectric modulus (M*), admittance (Y*), and tanδ (or tand) are also important to analyze. These functions are calculated by using Equations 10-14 [64, 66].

$$\varepsilon^* = \varepsilon' - j\varepsilon'' \tag{10}$$

$$M^* = M' + jM'' = \frac{1}{\varepsilon^*} \tag{11}$$

$$Y^* = Y' + jY'' = \frac{1}{Z^*} \tag{12}$$

$$Z^* = \frac{1}{j\omega C_0 \varepsilon^*} \tag{13}$$

and

$$\tan\delta = \frac{\varepsilon'}{\varepsilon''} = \frac{M'}{M''} = \frac{Z'}{Z''} = \frac{Y'}{Y''} \tag{14}$$

where ε' and ε" are real and imaginary permittivity, M' and M" are real and imaginary dielectric modulus, Y' and Y" are real and imaginary admittance, C_0 is geometric capacitance, ω is the angular frequency, and $j = \sqrt{-1}$.

1.4.3 Equivalent Circuit Modeling

Fitting the electrical data to equivalent circuit models is one way to connect the microstructure with electrical data. Pruyn, et. al. developed a circuit, shown in Figure 6, that explains electrical behavior of a grain-like microstructure composite of antimony tin oxide (ATO) / glass [67]. The circuit elements described in Figure 6 are L for inductors, R for resistors, and CPE for constant phase elements. CPE is used rather than capacitors (C) because they represent imperfect capacitors. They take into account varying thickness,

varying composition, or non-uniform current distribution [68]. The circuit elements are attributed to the intrinsic particle properties and interactions between particles (filler-filler, filler-glass). The contribution of the ATO is assigned to an inductor and resistor in series (indicates conductive behavior), and the contribution of the glass is assigned to a CPE and resistor in parallel (indicates insulating behavior). The rest of the resistors and capacitors within the circuit indicate the contribution of the glass and ATO interacting. This same circuit is applied to the insulating MWCNT/PMMA composites of this work due to having similar grain-like microstructures. Previous work had modeled conductive composites as an inductor and resistor in series [57, 67], indicating, like the circuit in Figure 6, that the conductive filler electrical data may be simplified to an inductor and resistor in series within segregated network composites. Breaking down the contribution to the electrical properties of each material in the composite will aid in understanding the interactions between materials (filler-filler, matrix-matrix, and filler-matrix) and the intrinsic properties of the materials, which is the objective of this thesis.

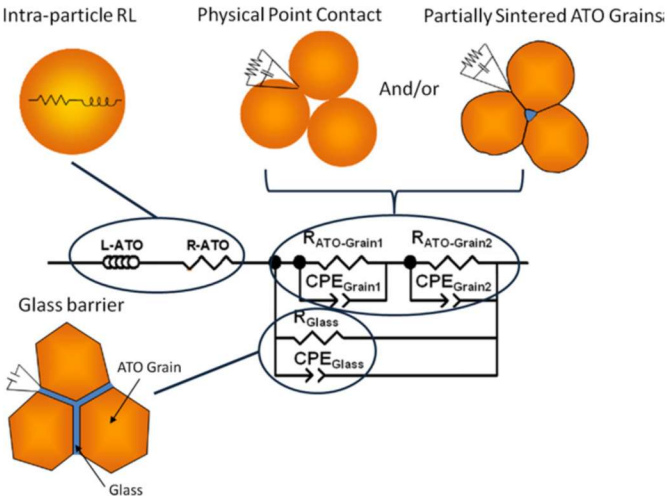

Figure 6 – Schematics of the possible filler interfaces present in ATO/Glass composites and equivalent circuit model [67].

1.5 Background on Materials used in the Composites

Multiwall carbon nanotubes (MWCNT) and four types of silicon carbide (SiC) were used as conducting and semiconducting filler materials. PMMA and borosilicate glass were used as insulating matrix materials. This section will give some background on the properties of these materials and why they were chosen.

1.5.1 Multiwall Carbon Nanotubes

MWCNT have superior properties including excellent mechanical strength along with high electrical and thermal conductivity that make them a material of interest in composite fabrication [54]. They are able to improve the electrical, mechanical, thermal, and optical properties among others when added to insulating matrices since composites

exhibit a combination of the filler and matrix properties [54]. MWCNTs have low resistance which gives them a higher electrical conductivity than copper [69]. Possible applications for MWCNT composites include electromagnetic interference (EMI) shielding, transparent conducting films, gas sensors, and more [55, 70, 71]. MWCNTs may have different diameters and aspect ratios, which may impact the properties of composites [54]. MWCNT powders showing polydispersity in size are shown in Figure 7 with an inset that shows the MWCNT wall thickness [2].

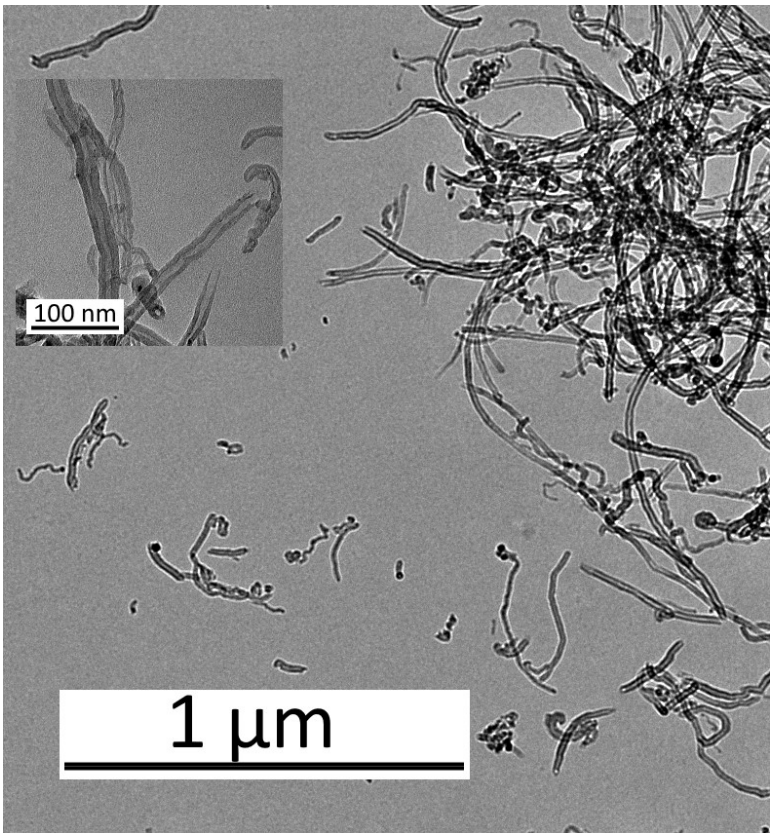

Figure 7 –TEM image of multi-walled carbon nanotubes (MWCNT) powder. Inset image was obtained at a higher magnification [2]

1.5.2 Silicon carbide

SiC has high thermal conductivity that allows dispersion of heat [72]. This property and the ability to absorb microwave energy and convert it into heat allows them to be useful for microwave applications [73, 74]. SiC crystallizes in a number of different crystal structures: (β) 3C-SiC, 4H-SiC, and (α) 6H-SiC, which are shown in Figure 8 [75]. From Figure 9, where thermal conductivity is plotted versus temperature, it can be seen that using different crystal structures may result in slightly different properties.

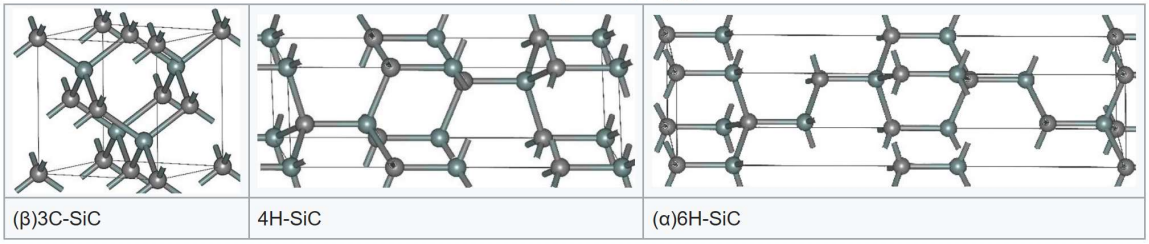

Figure 8 – Crystal structures of silicon carbide [75]

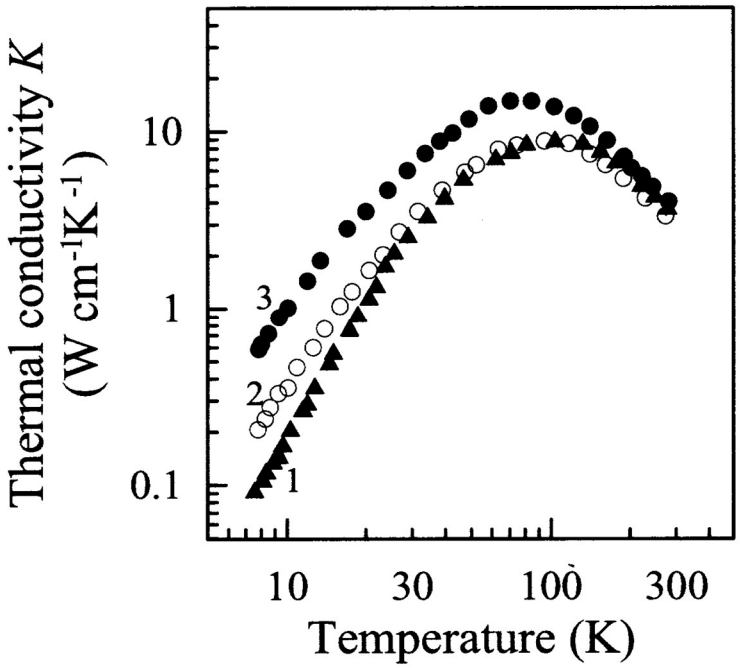

Figure 9 – Thermal conductivity versus temperature for 1) 4H-SiC, 2) 3C-SiC, 3) 6H-SiC [72]

1.5.3 PMMA

PMMA is a commonly used matrix for polymer composites [6, 8, 9, 16, 18-22, 54, 55]. The molecular structure of PMMA is shown in Figure 10 [76]. It is an amorphous material with a glass transition temperature in the range of 100-120 °C [77, 78].

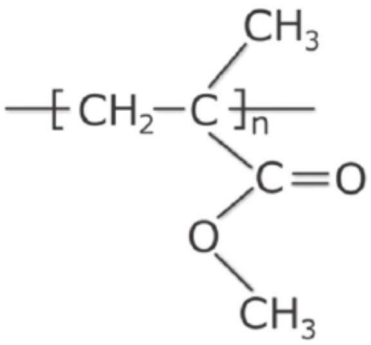

Figure 10 – Molecular structure of PMMA [76]

1.5.4 Borosilicate Glass

Borosilicate glass has a range of properties that makes it useful as a matrix material for composites. These include low thermal expansion (and therefore thermal shock resistance), glass transition temperatures around 500-600°C, chemical durability, and low melting temperatures [79].

1.6 Hypothesis and Objectives

The main objective of this thesis is to develop an understanding of how conductive networks form inside insulating matrix composites through microstructural analysis, impedance spectroscopy, and equivalent circuit models. The hypothesis is that using equivalent circuit models to represent the electrical data of the individual materials and their composites will enhance our understanding of conductive filler network formation in insulating matrices using various processing and material types. Applying the equivalent circuit models is hypothesized to show the influence of the individual materials on the overall electrical properties of the composites. This understanding should be useful to tailor

composites for specific applications with a reduction of trial and error. Composites, in general, allow for a combination of the matrix and filler materials properties. This is especially useful for when the filler is expensive as only a small amount of filler would be needed to achieve properties similar to the properties of the innate filler properties. Therefore, this thesis will focus on factors that affect the formation of a conductive filler network through an insulating matrix material. These factors are the processing of polymer composites, filler shape, filler size, and humidity. AC impedance spectroscopy and microscopy are used to study the effects of those factors, then circuit fitting is applied to break down the contribution of the individual materials within the composites.

This thesis will first describe the experimental procedures (Chapter 2) and summarize the composites fabricated (Chapter 3). Then the effect of the processing method, specifically mixing of the powders, will be discussed using MWCNT/PMMA composites (Chapter 4). The mixing methods discussed are mechanical, melt, and solution mixing. Next an impedance study of silicon carbide powders properties is conducted (Chapter 5). Four types of silicon carbide powders (nano-sized, micron-sized, whisker, and nanowire SiC) are compared using FTIR, XRD, and microscopy. In Chapter 6, three of the SiC types (nano-, micron-, and whisker SiC) are used to identify the effect of filler shape on the electrical and microstructural properties of SiC/PMMA, mechanically mixed composites. This is followed by a study using SiC whiskers and SiC nanowires as fillers in a borosilicate glass. Composites were fabricated using SPS to determine the effect of the aspect ratio of the filler on the electrical and microstructural properties (Chapter 7). During this investigation, it was observed that the ambient humidity affected the electrical data of the glass composites. This observation led to the study of the effect of humidity on the

electrical properties of SiC_w/glass composites, which is discussed in Chapter 8. Chapter 9 shows the fits of equivalent circuit models to data presented in Chapters 4-8 to break down the electrical data into the roles of each material and microstructure in the overall electrical properties. Chapter 10 provides conclusions and suggestions for future work.

2 EXPERIMENTAL METHODS

This chapter provides details concerning the main fabrication steps used to fabricate the composites described in this thesis and the methods to characterize them. To have a variety of composites to fit equivalent circuits to, multiple methods and materials were used to fabricate the composites. Impedance spectroscopy and microscopy were the main characterization methods used. Other methods (XRD, XPS, FTIR) were used as needed.

2.1 Materials

In this study, two different matrix materials were used along with several fillers to make the composites described in this study. Table 1 contains a list of all the matrix and filler materials used in this research. The images of those materials are shown in Figure 11.

Table 1 – Materials Used

Matrix Material	**Particle Size**	**Manufacturer**
Polydisperse PMMA	10-100 μm [59]	Buehler Ltd., Transoptic powder
Borosilicate Glass Microspheres	45-53 μm [80]	Mo-Sci Corporation
Filler Material	**Particle Size**	**Manufacturer**
Nanoparticle β-SiC	10-70 nm	US Research Nanomaterials, Inc
Micron-sized β-SiC	1-2 μm	Alfa Aesar
Whisker β-SiC	L: 10-50 μm, D: 1 μm	Advanced Composite Materials
β-SiC Nanowires	D: 10-122 nm	Fabricated from MWCNT
Multiwall CNTs	L: 0.5-2 μm, D: ~20 nm, Purity >95%	Cheaptubes.com
PMMA – polymethyl methacrylate SiC – silicon carbide CNT – carbon nanotube		

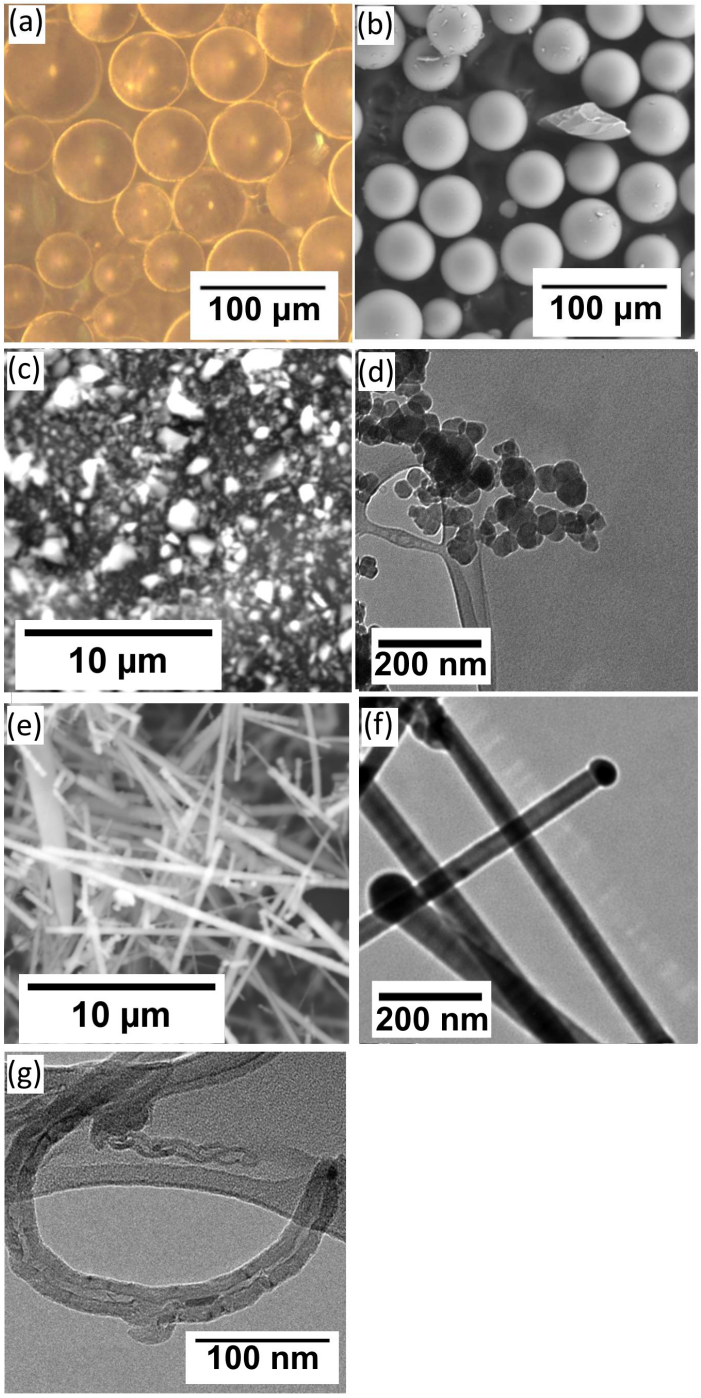

Figure 11 – (a) Polymethylmethacrylate (PMMA), (b) Borosilicate glass microspheres [80], (c) micron-sized silicon carbide (SiC) [81], (d) nano-sized SiC, (e) SiC whiskers [81], (f) SiC nanowires, (g) multiwall carbon nanotubes (MWCNT)

2.2 Mixing Precursors

Mechanical mixing was performed using three different methods. For mixing the SiC/PMMA, a blender was used for 15 minutes at room temperature until fully mixed. It was run in intervals to avoid heating the mix. For mixing CNT/PMMA and SiC nanowire/glass, a FlackTek Inc Speedmixer was used at 3500 rpm for 10 s. Lastly, the SiC_w/glass were mixed using a rotary ball mill with 5mm alumina media (99.5%),[82] then later remixed in a speedmixer at 3500 rpm for 10 s. Figure 12a shows a general schematic of mechanical mixing.

Melt mixing was accomplished using a DSM 15cc micro compounder (vertical, co-rotating twin-screw micro-extruder) at 225 ^{o}C for 3 minutes after the powder was initially mixed using a speedmixer [6]. The resulting strands were then broken by hand and put in a blender to break them into smaller pieces. The blending allowed for a more homogeneous compound where the conductive paths are more randomly distributed.

In solution mixing, the PMMA solvent was ethyl acetate with a solid-to-solvent weight ratio of 1:6 [10]. The speedmixer was run for 20 seconds intervals repeatedly until the PMMA was dissolved. Then the CNT was added and mixed in. Lastly, the dispersion was cast into a Petri dish and left to dry. When mostly dried, it was cut into small pieces using a razor blade and then compacted. This process is shown in Figure 12c.

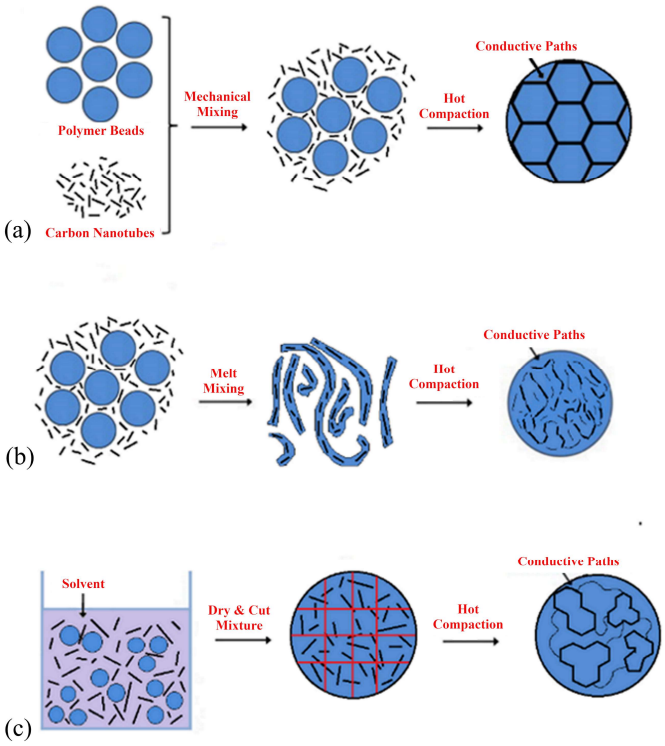

Figure 12 – Schematic of mixing methods (a) mechanical, (b) melt, and (c) solution mixing and final compacted microstructure [6]

2.3 Compaction

Two methods were used to compact the powders into pellets for electrical measurements using the parallel plate method. For polymer composites, the powders were pressed while heated. For glass composites, spark plasma sintering (SPS) was used to form the pellets.

2.3.1 Pressing

For polymer matrix composites and neat PMMA, after all mixing methods were completed, two grams of each mixture were compression molded using a Struers Prontopress 2 (Figure 13) at 170 °C and 20 kN. The result was pellets of 31.7 mm in diameter and approximately 2 mm in thickness.

Figure 13 – Struers Prontopress 2

2.3.2 SPS Procedure

A Fuji Electronic Industrial Co., LTD Dr. Sinter model SPS-211Lx, Figure 14, was used to fabricate the glass matrix composites. Settings used were 50 °C/min to 610 °C with

a 5 minute hold at a uniaxial pressure of 23.4 MPa under vacuum based on past work by Thomas Rudzik [80]. The powder mixes were placed in graphite foil-lined graphite dies. A schematic of the die is shown in Figure 15. The temperature was monitored from a thermocouple placed in a hole next to the powder. This ensures the temperature read is close to the temperature of the sample.

Figure 14 – Dr Sinter Lab™ Spark Plasma Sintering System

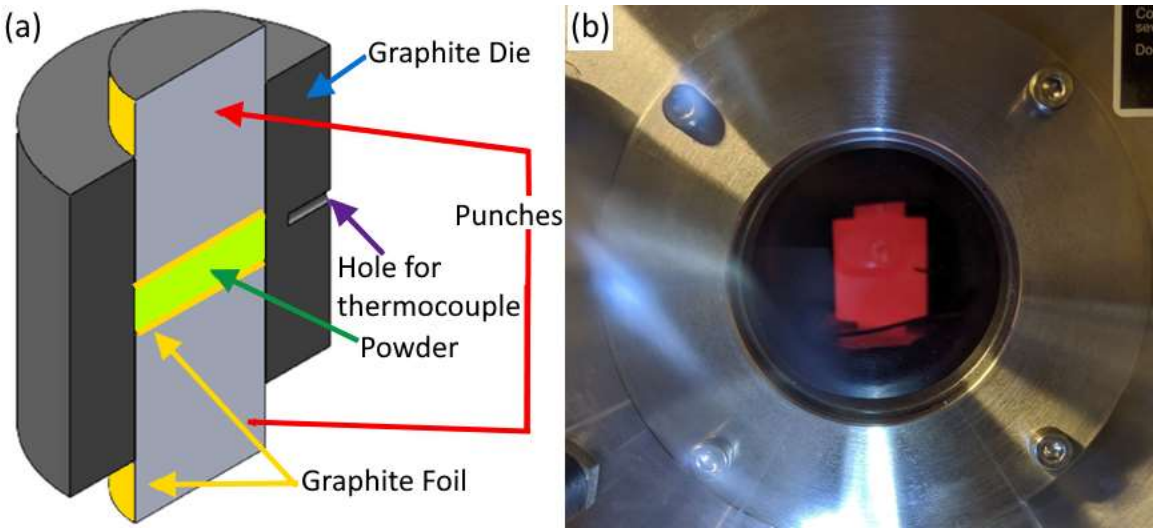

Figure 15 – (a) Schematic of die setup (modified from [80]) and (b) picture of live run at 610°C

2.4 Sectioning, Polishing and Electrode Deposition

Since the polymer composites were soft, only the edges of the samples were polished using a Buehler Ecomet 250 Grinder Polisher (Figure 16) while the large flat faces were left alone. For the glass composites, SiC 180 grit SiC pads were used to remove excess carbon and diamond pads and paste were used to smooth the sample surfaces for both electrical and microstructural examination. Additionally, some polymer composite samples were fractured by hand at room temperature to expose fractured cross-sections without polishing disruption.

Figure 16 – Buehler Ecomet 250 Grinder Polisher

For those sections and all other composites, silver electrodes were deposited onto the large flat faces (parallel-plate configuration). This was accomplished by sputtering Ag (nominal purity of 99.9%-Alfa Aesar) with an argon plasma in a Denton Vacuum Desk II Turbo Sputter Coater (Figure 17) for 16 minutes to ensure good conductivity of electrodes. Scotch tape was used to protect the sides from the silver while silver was sputtered on both faces of the pellets. If silver got onto the sides despite the tape, the silver was polished off.

Figure 17 – Denton Vacuum Desk II Turbo Sputter Coater

2.5 Molten Salt Mediated Synthesis

For comparison between two sizes of anisotropic SiC (nano- and micron- sized), SiC nanowires were fabricated. Wu et al. developed a method for synthesizing silicon carbide nanowires from carbon nanotubes [83]. Figure 18 shows a schematic of the method. Silicon, sodium fluoride, and sodium chloride were mixed using the speedmixer at 3500 rpm for 10 seconds and then placed into an alumina boat. Rather than using carbon paper with holes, a plain carbon cloth (1071 HCB, Fuel Cell Store) was used because it naturally has holes unlike carbon paper. A thin layer of CNT was spread across the top of the carbon fabric which was then placed on top of the alumina boat and into a high temperature tube furnace. The tube furnace was run at 1250 °C for 8 hrs with argon gas flow.

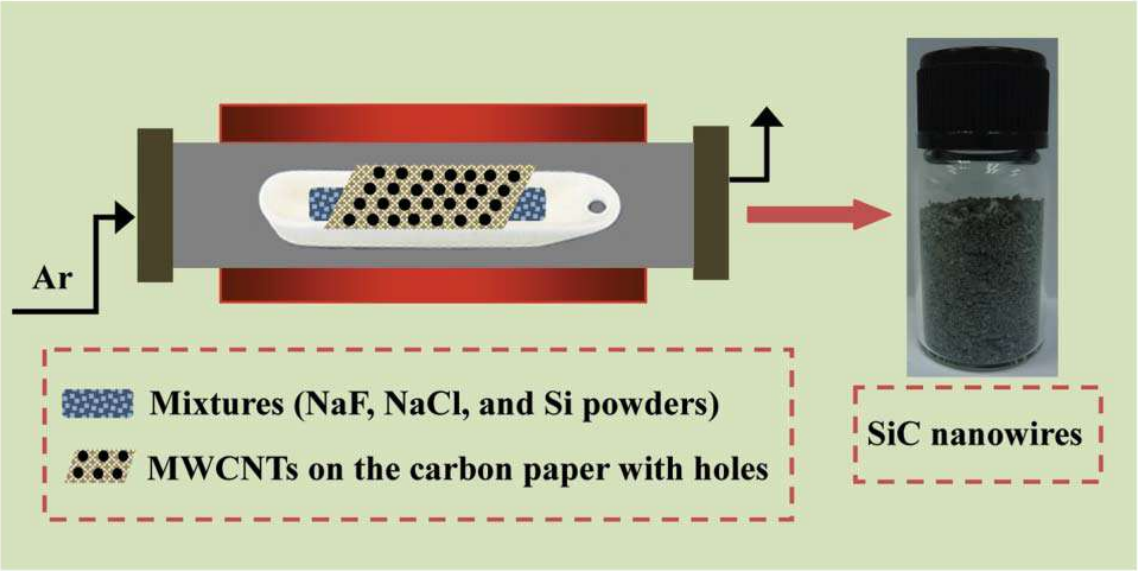

Figure 18 – Schematic of Molten-salt-mediated synthesis of silicon carbide (SiC_{nw}) [83]. In this study, carbon cloth was used instead of carbon paper.

2.6 Characterization

The characterization methods used to analyse the powders and composites are discussed in this section.

2.6.1 Powders

Scanning and transmission electron microscopy (SEM & TEM), optical microscopy, x-ray diffraction (XRD), and in-situ AC impedance spectroscopy were used to analyse the powders used in this study.

2.6.1.1 Optical and Electron Microscopy

SEM and TEM were used to determine the sizes of the powders used in this research. A Hitachi S-3700N VP-SEM (Hitachi High Technologies America Inc., Dallas, TX) was used by Thomas Rudzik to image glass, micron sized SiC, and whisker SiC [81]. The size of the MWCNTs, nano-sized SiC, and SiC nanowires were studied using a Hitachi-HT7700 TEM. The TEM was also used to verify the transformation of MWCNT into SiC nanowires. The PMMA powder was imaged using a Celestron PentaView LCD Digital Microscope (Figure 19).

Figure 19 – Celestron PentaView LCD Digital Microscope

2.6.1.2 X-ray Diffraction

The crystalline structures of the SiC powders were verified using XRD data gathered using a Malvern PANalytical Empyrean (Figure 20) by David Tavakoli at the Materials Characterization Facility (MCF) at Georgia Tech [84]. The equipment conditions used for XRD testing were a Cu Kα incident beam, a divergence slit of 0.38 mm, and a receiving slit of 1.52 mm with an angle range from 10 to 100 degrees.

Figure 20 – Malvern PANalytical Empyrean [84]

2.6.1.3 AC Impedance Spectroscopy of Compressed Powders

The electrical properties of the filler powders were measured in-situ under pressure through a custom setup shown in Figure 21 located in a 12-ton model-C uniaxial Carver press (Carver Inc., Wabash, IN) [5, 80]. The steel pistons were insulated from the Carver

press by using electrical tape as seen in Figure 21. The electrical connections were set up using two probes – one each for the top and bottom that allows the current to run through the pistons and compacted powder. The impedance was measured at pressures between 0 MPa to 300 MPa, typically in increments of 50 MPa. A Solartron 1260 analyzer (Solartron Analytical, Farnborough, Hampshire, U.K.) was used to scan at 100 mV ac voltage with a frequency range of 10 MHz – 100 mHz.

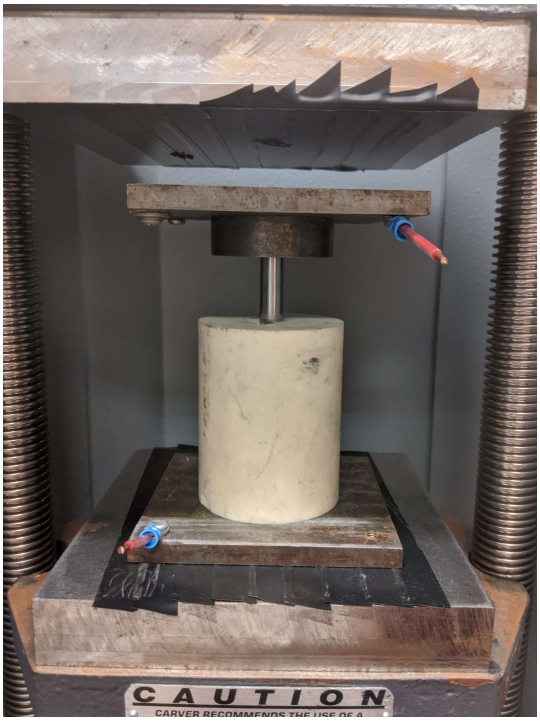

Figure 21 – Alumina die used for electrical characterization of powder materials under pressure [5, 80]

2.6.2 Composite Samples

The microstructures and electrical properties of the resulting composite samples were studied using the methods described in this section.

2.6.2.1 Microstructural Analysis

The samples for microstructural analysis were imaged using a Leica DM IRM inverted microscope and Celestron PentaView LCD Digital Microscope. For carbon nanotube composites, samples with compositions after percolation that had at 10^4 Ω-cm resistivity were selected for further analysis using a scanning electron microscope (SEM), specifically a Hitachi SU-8230 SEM, and transmission electron microscopes (TEM). For SiC/glass composites, a Phenom ProX Scanning Electron Microscope (Figure 22) was used by Gillian Brown to image select samples along with energy-dispersive x-ray spectroscopy (EDX).

Figure 22 – Phenom ProX Scanning Electron Microscope [85]

For MWCNT/PMMA composite samples analysed using the TEMs, Dr. Steve Jett and Dr. Chanchal Ghosh prepared by microtoming and then imaged the same samples that were studied using SEM at the Center for Integrated Nanotechnology at Sandia National Labs. The lamellas were collected on 3 mm carbon coated copper grids. The samples were further coated with a very fine layer of carbon (~ 5 nm) to provide better stability under the electron beam. The TEM studies were carried out by Dr. Chanchal Ghosh and Dr. Steve Jett using a Tecnai F30 TEM operated at 300 kV (for solution and melt mixed) and a FEI Talos operated at 120 kV (for mechanically mixed). At high magnification specimen damage due to the electron beam radiation is very high.

2.6.2.2 Small Angle X-ray Scattering

Ultra-small angle X-ray scattering (USAXS) and SAXS were used to examine the CNT/PMMA samples. These measurements and their analysis were achieved with the help of Dr. Jan Ilavsky at the 9ID-C beamline at Argonne National Lab. SAXS is capable of delivering structural information of dimensions between 1 and 100 nm, while USAXS is able to resolve larger dimensions [86-88]. Figure 23 shows a cartoon of the angles of the X-ray scattering [89].

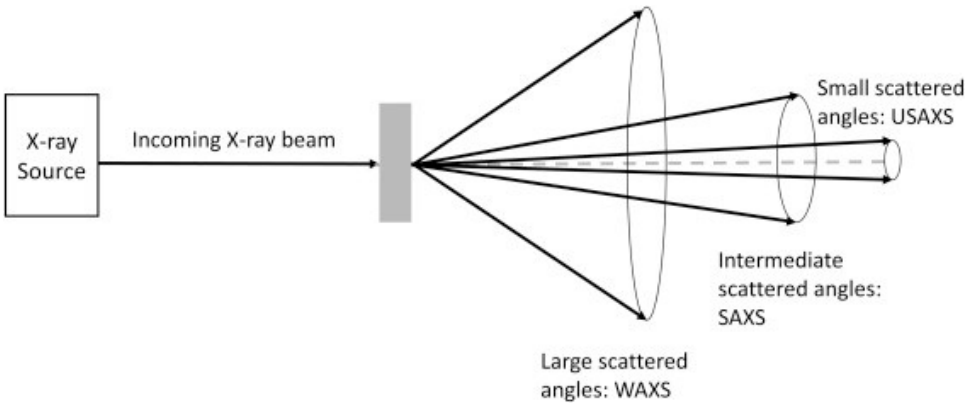

Figure 23 – X-ray scattering angles [89]

2.6.2.3 AC Impedance Spectroscopy of Composites

Electrical characterization through the thickness of the composites was performed using impedance spectroscopy. A Solartron 1260 analyzer was used in conjunction with a Solartron 1296 Dielectric Interface (Solartron Analytical, Farnborough, Hampshire, U.K., Figure 24a) for the measurements using a parallel plate setup (Figure 24b). The dimensions of the samples were measured using a digital caliper (Mitutoyo Corp., model 500-196) and used to calculate the resistivity. The majority of scans were taken with a 500mV ac voltage and a frequency range of 10 MHz-100 mHz. For glass composites, the humidity at the time of measurement was controlled by conducting the measurements within a humidity chamber.

Figure 24 – (a) A Solartron 1260 analyzer with a Solartron 1296 Dielectric Interface (Solartron Analytical, Farnborough, Hampshire, U.K.) and (b) a parallel plate setup.

2.7 Summary

This chapter described the materials used, methods of composite fabrication and characterization for composites and powders. Impedance spectroscopy and microscopy were the main characterization methods used. Other methods (XRD, XPS, FTIR) were used as needed. The next chapter will show the compositions of each set of composites made and which methods were used to fabricate them.

3 SAMPLES FABRICATED

This chapter outlines the composite samples made for this thesis along with the methods used to fabricate each set of composites. In all cases, the compositions were expressed in phr (parts per hundred resin), which is a measurement of concentration, similar to weight percent and calculated according to the equation: Phr = [(mass of filler) / (mass of polymer + mass of filler)] x 100. For convenience, volume and weight percent will also be provided.

Overall, three samples at minimum were electrically measured. This amount of samples was selected due to the high repeatability of impedance testing. Impedance spectroscopy is very sensitive to the microstructural changes within a composite. The deviation between samples are typically very small except around percolation. Therefore, it directly relates to the repeatability of fabricating the samples. Around percolation, there is the minimum mount of filler needed to form a conductive pathway through the composite. This means that the pathway is not always formed around percolation due to having a small amount of filler. The electrical measurements show this variation around percolation by having larger standard deviations. In the cases where the samples have a larger difference from each other, more samples were made to accurately determine the average electrical properties of the composites.

3.1 CNT/PMMA Composites

The CNT/PMMA composites were mixed using three methods: mechanical, melt, and solution mixing. 10 grams of each mixture were made in order to make 3-7 pellets per concentration for measurement and characterization. The concentrations used for mechanically mixed samples were 0.005, 0.025, 0.0375, 0.05, 0.0875, 0.1, 0.15, 0.2, 0.25 phr as seen in Table 2. All PMMA composites were fabricated as described in Chapter 2 Section 2.3.1. Concentrations above 0.25 phr were attempted but fractured on or before removal from the compression molder. The concentrations used for melt mixed samples were 0.01, 0.1, 0.5, 1, 2, 3, 4, 6, 8, 10, 12, and 15 phr (Table 3), and the concentrations used for solution mixed samples were 0.01, 0.1, 1, 1.5, 1.75, 2, 2.25, 2.5, 3, 4, and 5 phr (Table 4). At minimum, three samples were made per concentration. Often the concentrations around percolation required more samples to reduce the error.

Table 2 – Concentrations used to make mechanically mixed MWCNT/PMMA composites

Mechanically Mixed MWCNT/PMMA			
Phr	Wt. %	Vol. %	# of Samples
0.005	0.005	0.003	4
0.025	0.025	0.014	4
0.0375	0.038	0.021	4
0.05	0.050	0.028	4
0.0875	0.087	0.049	4
0.1	0.100	0.056	4
0.15	0.150	0.084	4
0.2	0.200	0.112	4
0.25	0.249	0.140	4

Table 3 – Concentrations used to make melt mixed MWCNT/PMMA composites

Melt Mixed MWCNT/PMMA			
Phr	Wt. %	Vol. %	# of Samples
0.01	0.010	0.006	4
0.1	0.100	0.056	4
0.5	0.498	0.280	4
1	0.990	0.556	7
2	1.961	1.102	7
3	2.913	1.637	7
4	3.846	2.161	7
6	5.660	3.181	3
8	7.407	4.162	4
10	9.091	5.108	4
12	10.714	6.020	3
15	13.044	7.329	4

Table 4 – Concentrations used to make solution mixed MWCNT/PMMA composites

Solution Mixed MWCNT/PMMA			
Phr	Wt. %	Vol. %	# of Samples
0.01	0.010	0.006	4
0.1	0.100	0.056	4
1	0.990	0.556	4
1.5	1.478	0.830	3
1.75	1.720	0.966	3
2	1.961	1.102	5
2.25	2.201	1.237	3
2.5	2.439	1.371	3
3	2.913	1.637	5
4	3.846	2.161	3
5	4.762	2.676	3

3.2 SiC/PMMA Composites

For SiC/PMMA composites, the powders were mixed using a blender. 10 grams of each mixture were made in order to make 4-6 pellets per concentration for measurement and characterization. Three types of SiC were used: nano-sized, micron-sized, and whisker SiC. The concentrations made were 0.1, 0.5, 1, 2, 3, 7.5, 10, 12, and 15 phr for all three types plus 5 phr made for micron-sized SiC. At minimum, three samples were made per concentration. All PMMA composites were fabricated as described in Chapter 2 Section 2.3.1.

Table 5 – Concentrations used to make SiC/PMMA composites

SiC/PMMA					
Phr	Wt. %	Vol. %	# of mSiC Samples	# of nSiC Samples	# of SiC_w Samples
0.1	0.100	0.037	4	4	4
0.5	0.498	0.183	4	4	4
1	0.990	0.364	4	4	4
2	1.961	0.721	4	4	4
3	2.913	1.071	4	4	4
7.5	6.977	2.565	4	5	4
10	9.091	3.342	4	4	4
12	10.714	3.939	6	5	4
15	13.044	4.795	4	4	4

3.3 SiC Whisker and SiC Nanowire/Borosilicate Glass Composites

The powders were mixed (and remixed for the SiC_w/glass that was previously ball milled) using a speedmixer at 3500 rpm for 15 seconds. The glass composites were

fabricated using SPS at 50°C per minute to 610°C with a 5 minute hold. The compositions created were 0.01, 0.1, 0.25, 1, 1.5, 2.5, 5, 7.5, 10, and 12.5 phr for SiC whisker composites. A larger sample of 10 phr was made then cut to study the conductivity and microstructure across the sample. For SiC nanowire composites, the concentrations made were 0.01, 0.05, 0.1, 0.325, 0.5, 1, 1.5, 3, and 4 phr. At least three samples of each concentration were made. For the SiC_w composites, there was a limited amount of mixed powder and no more samples were made after the amount was used. New composite mixes did not match the electrical data of the previous composites which may be due to a change in glass composition. The SiC nanowire used was made according to what was shown in Chapter 2 Section 2.5.

Table 6 – Concentrations used to make SiC_w/Glass composites

SiC_w/Borosilicate Glass			
Phr	Wt. %	Vol. %	# of Samples
0.01	0.010	0.007	3
0.1	0.100	0.068	3
0.25	0.249	0.171	3
1	0.990	0.679	3
1.5	1.478	1.013	3
2.5	2.439	1.672	3
5	4.762	3.264	3
7.5	6.977	4.782	3
10	9.091	6.231	3
12.5	11.111	7.615	3

Table 7 – Concentrations used to make SiC nanowire/Glass composites

SiC_{nw}/Borosilicate Glass			
Phr	Wt. %	Vol. %	# of Samples
0.01	0.010	0.007	3
0.05	0.050	0.034	3
0.1	0.100	0.068	3
0.325	0.324	0.222	4
0.5	0.498	0.341	3
1	0.990	0.679	3
1.5	1.478	1.013	3
3	2.913	1.996	3
4	3.846	2.636	3

3.4 Summary

To provide a thorough examination of the effect of processing and particle morphology, three types of composites were fabricated for this thesis (CNT/PMMA, SiC/PMMA, and SiC/Glass). This chapter listed the compositions made for each composite along with the methods used to fabricate them. In the next chapter, the differences in processing will be discussed using the CNT/PMMA composites.

4 EFFECT OF THREE DIFFERENT MIXING METHODS ON ELECTRICAL AND MICROSTRUCTURAL PROPERTIES (CNT/PMMA)

The mixing method used to fabricate composites strongly affects the network formation of the fillers (MWCNT in this case). This chapter will show that three different mixing methods created three different microstructures while keeping all other factors (materials and compression molding) the exact same. These resultant microstructures also cause a change in electrical properties which will be discussed in Chapter 9.

4.1 Microstructure (Optical, SEM, and TEM)

The MWCNT/PMMA composites were imaged using a Leica DM IRM inverted microscope. The microstructures shown in Figure 25, Figure 26, and Figure 27 show that the three mixing methods created distinctly different microstructures [6]. To illustrate the change of microstructures with concentration of MWCNT, microstructures of samples before, at, and after percolation are included in Figure 25, Figure 26, and Figure 27. In Figure 25 a-c, the mechanically mixed samples have segregated microstructures with clearly defined grain-like boundaries. Whereas the melt mixed samples, in Figure 26 a-c, have a distributed microstructure. Lastly, the solution mixed samples show large aggregates in the microstructure, Figure 27 a-c.

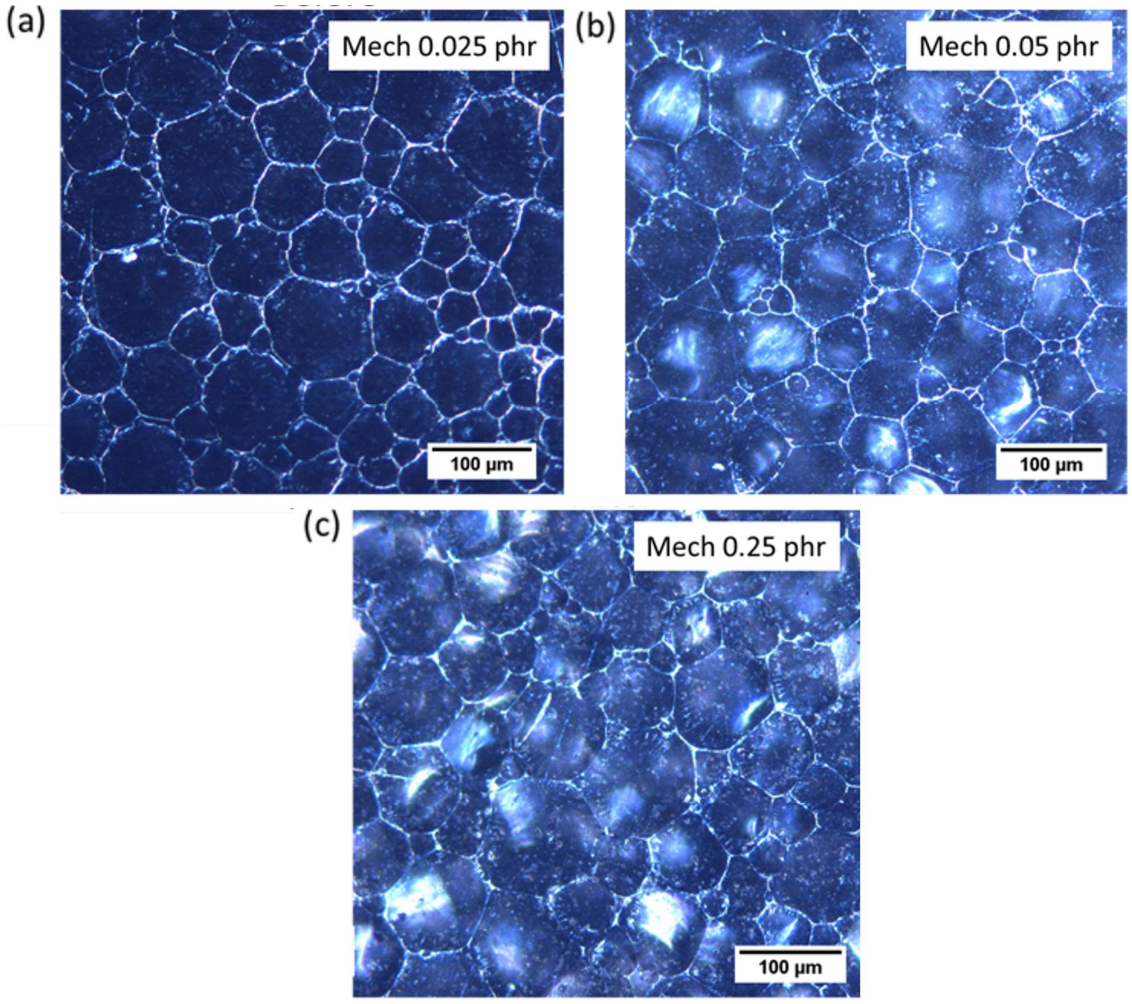

Figure 25 – Topography of mechanically mixed MWCNT/PMMA composites taken using an inverted microscope; (a) 0.025, (b) 0.05, and (c) 0.25 phr, before, at, and after percolation [6]

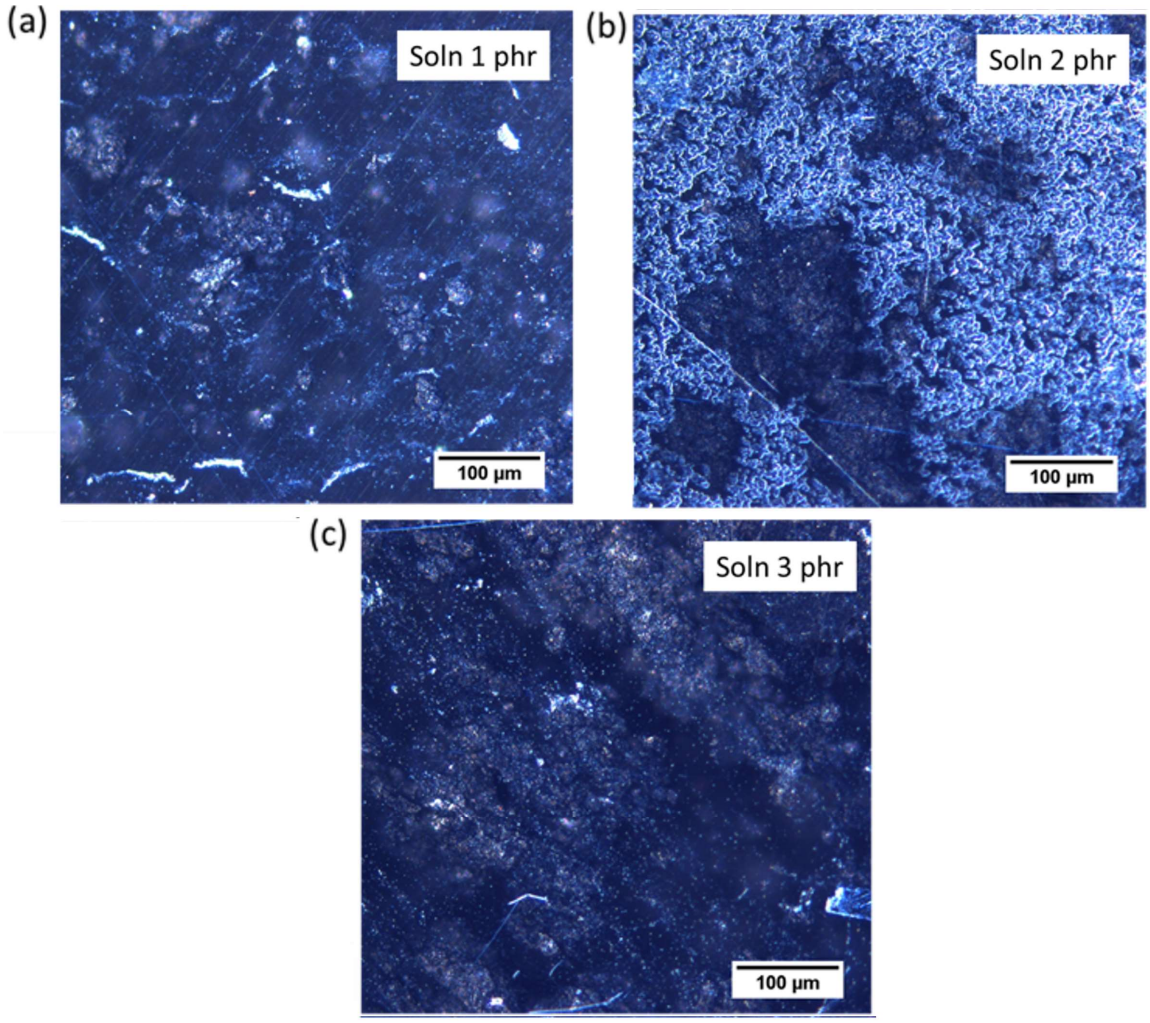

Figure 26 – Topography of solution mixed MWCNT/PMMA composites taken using an inverted microscope; (a) 1, (b) 2, and (c) 3 phr, before, at, and after percolation [6]

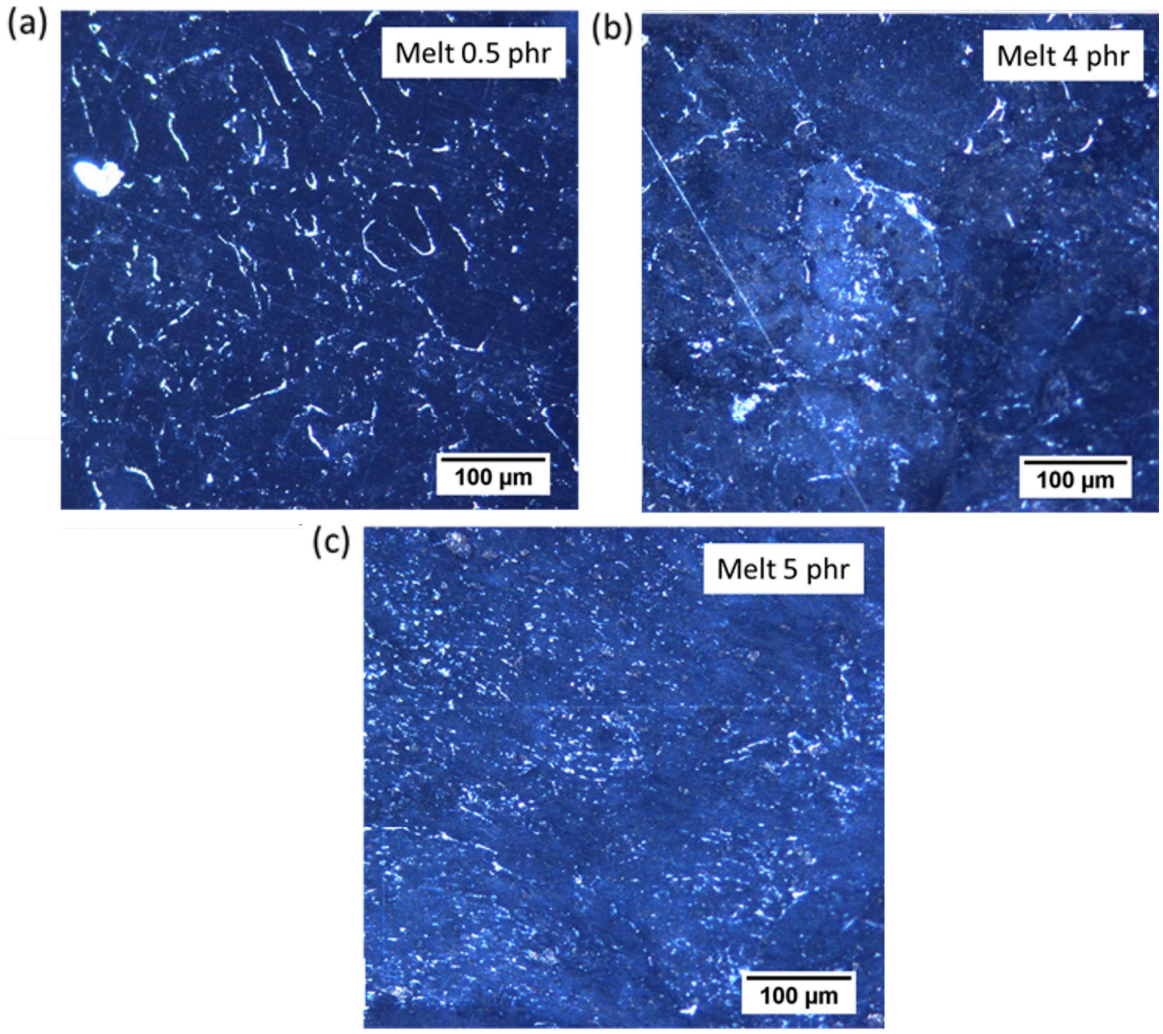

Figure 27 – Topography of melt mixed MWCNT/PMMA composites taken using an inverted microscope; (a) 0.5, (b) 4, and (c) 5 phr, before, at, and after percolation [6]

To study the placement of MWCNT within the PMMA matrix more closely, the samples were examined using a Zeiss Ultra60 FE-SEM. Samples that had a resistivity of 10^4 Ω-cm (after percolation which is explained in section 4.3) from all three mixing methods were chosen for closer study since the network would be fully formed at those concentrations [6]. Figure 28 shows the SEM topographical and fracture surfaces of the

MWCNT/PMMA composites for each method. Figure 28 a and d show a sample made via mechanical mixing. When looking at the fracture surface, it can be seen that the CNTs were segregated to the boundaries, breaking along the grain-like boundaries. Whereas in the melt mixed samples, CNTs are visible on both surfaces and the polymer is mixed with the CNT creating a random distribution, Figure 28 b and e. Lastly, the solution mixed samples formed agglomerates of CNT/PMMA which left the immediate area around the agglomerate deficient in CNT, Figure 28 c and f [6].

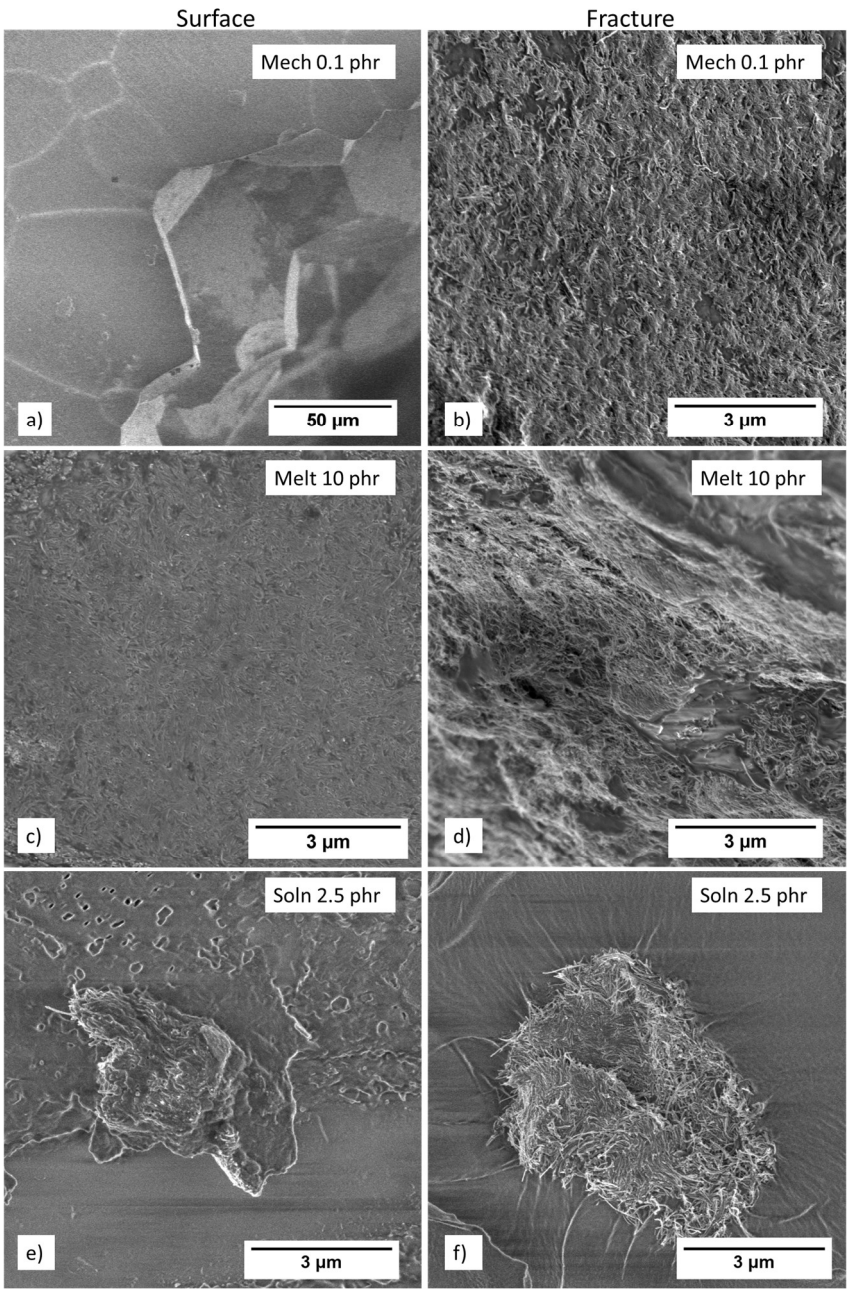

Figure 28 – Surface and fracture SEM images of (a, b) 0.1 phr mechanically mixed, (c, d) 10 phr melt mixed, and (e, f) 2.5 phr solution mixed PMMA composite samples that all had the same resistivity of 10^4 Ω-cm (obtained after percolation), modified from [6]

The same samples were studied using TEM. For comparison, the first row of Figure 29 displays SEM images while the other two are TEM images at increasing magnification. In all three cases, the CNTs are 12-15 nm in diameter while the length varies. In the bright-field TEM micrographs, dark spots can be observed that are the CNTs. The contrast in the amorphous matrix is mainly due to rumpling. The microtoming marks can also be observed in the polymer matrix. From the SEM images in Figure 29 a-c, the general microstructure is visible for each sample type. The TEM images in Figure 29 d-i show the placement of MWCNT within the PMMA much clearer. For mechanically mixed samples, the CNT is segregated to the boundaries with very few CNT outside the boundaries (Figure 29 d and g). For solution mixed samples, the CNT is contained in the agglomerates (Figure 29 e and h), leaving an area devoid of CNT surrounding the agglomerates. Lastly, Figure 29 f and i show that while the CNT is distributed in the PMMA with melt mixed samples, there are agglomerates within the microstructure also.

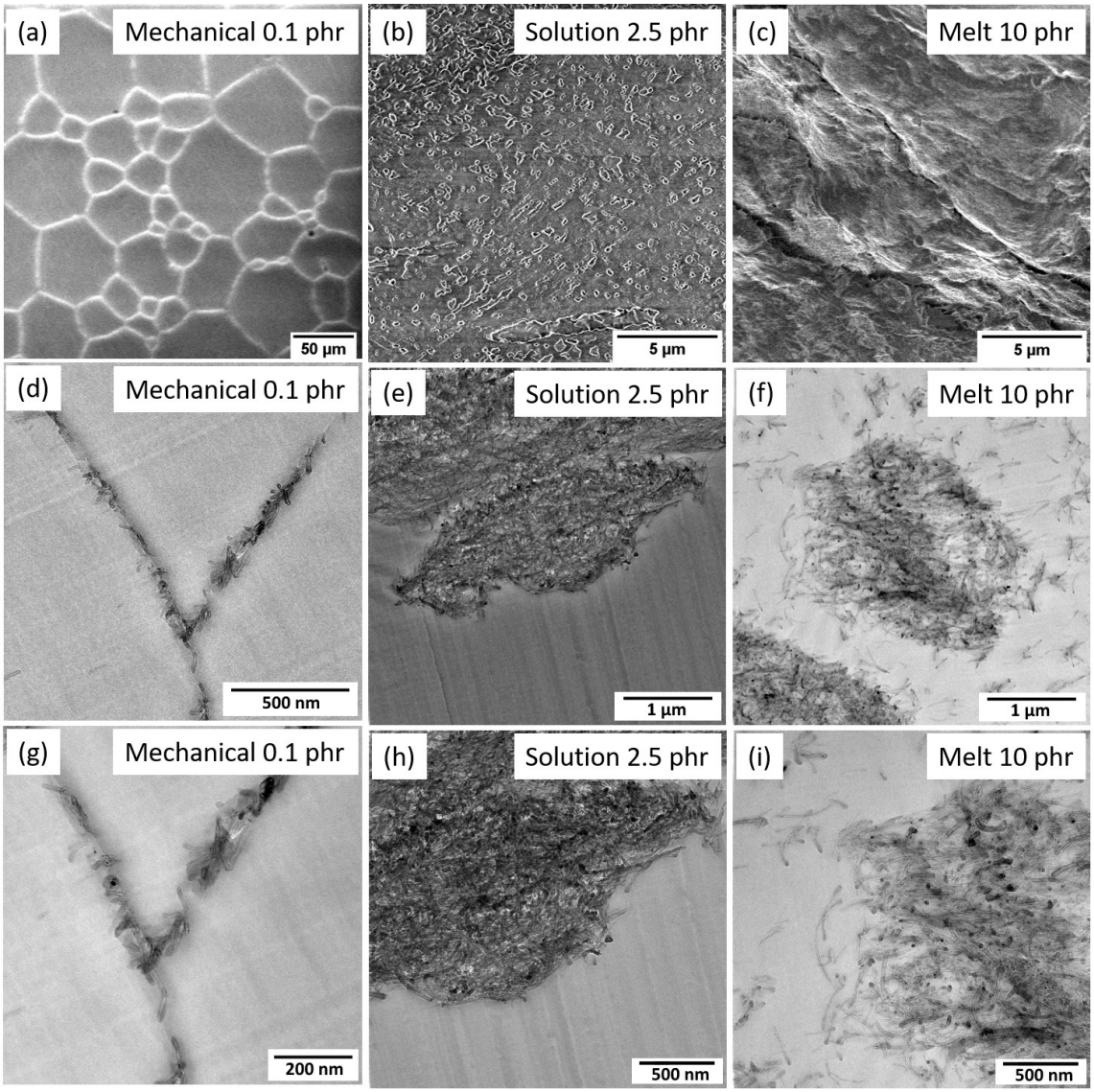

Figure 29 – (a-c) SEM and (d-i) TEM images of MWCNT/PMMA composites for mechanical, solution, and melt mixed samples just after percolation at 10^4 Ω-cm resistivity

To further explore the presence of agglomerates within the melt mixed MWCNT/PMMA composites, 0.5 phr and 4 phr samples were also imaged using TEM by

the CINT team (Figure 30). Even within the 0.5 phr composite, agglomerates are visible although they were smaller than for the higher concentration composites. Since no chemical was used to reduce the tendency of MWCNT to agglomerate, it is not surprising that agglomerates are visible at low concentrations.

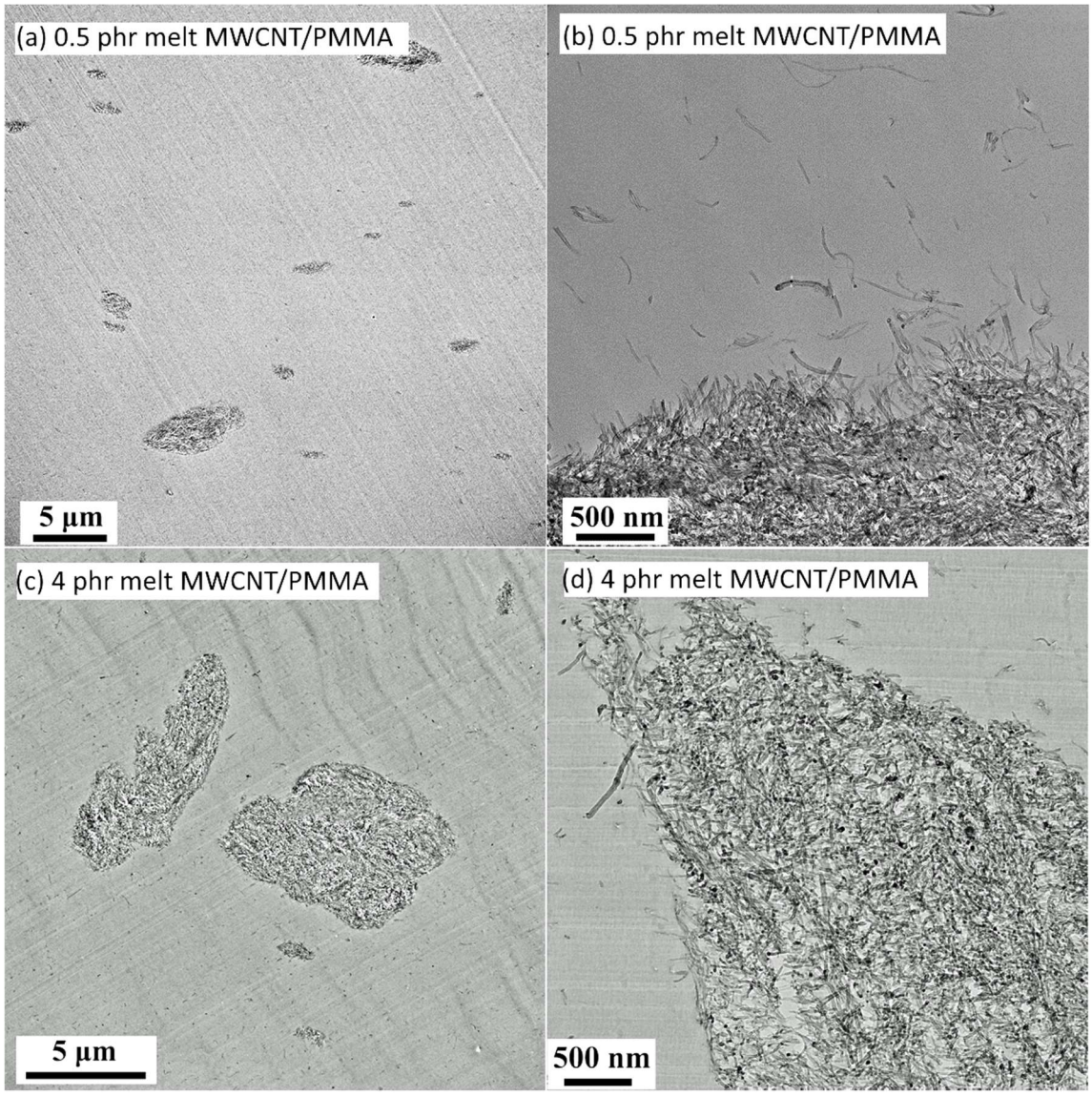

Figure 30 – TEM images of melt mixed MWCNT/PMMA composites

Selected area diffraction (SAD) analysis and diffraction contrast imaging were carried out on the solution and melt mixed samples. Both produced the same pattern which is shown in Figure 31, and the planes and interplanar spacings are summarized in Table 8. The patterns were analyzed and the interplanar spacing of the corresponding interplanar spacing are marked in Figure 31 which shows the diffraction pattern for MWCNT. The ring nature of the pattern indicates that the crystals themselves do not have any specific angular relationship. The radius of the rings provides the interplanar spacings which are then compared to CNT data within the ICDD database to verify the pattern represents MWCNT.

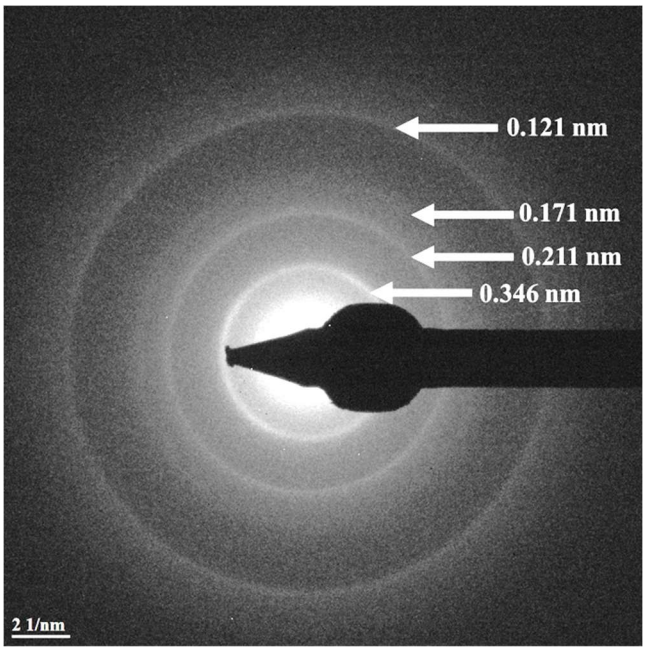

Figure 31 – Selected-area diffraction (SAD) of MWCNT in 10 phr melt mixed MWCNT/PMMA. The measured interplanar spacings are marked in the image. The beam stop is used because the specimen is thin, and the rings are therefore faint.

Table 8 – SAD interplanar spacing and planes (ICDD database) of MWCNT within PMMA matrix

Interplanar spacing (nm)	Planes
0.121	$11\bar{2}0$
0.171	0004
0.211	$10\bar{1}1$
0.346	0002

4.2 SAXS and USAXS of MWCNT/PMMA Composites

Ultra-small angle X-ray scattering (USAXS) and small angle X-ray scattering (SAXS) were used to examine the CNT/PMMA samples as mentioned in Section 2.6.2.2. SAXS is capable of delivering structural information of dimensions between 1 and 100 nm, while USAXS is able to resolve larger dimensions [86-88]. Figure 32 , Figure 33, and Figure 34 shows the intensity versus scattering vector, Q, which ranges between 10^{-4} – 1.5 $Å^{-1}$ for the mechanically, melt, and solution mixed CNT/PMMA composites, respectively. Each showed a very similar behavior. The data in Figure 32, Figure 33, and Figure 34 were then fit to a unified fit [90].

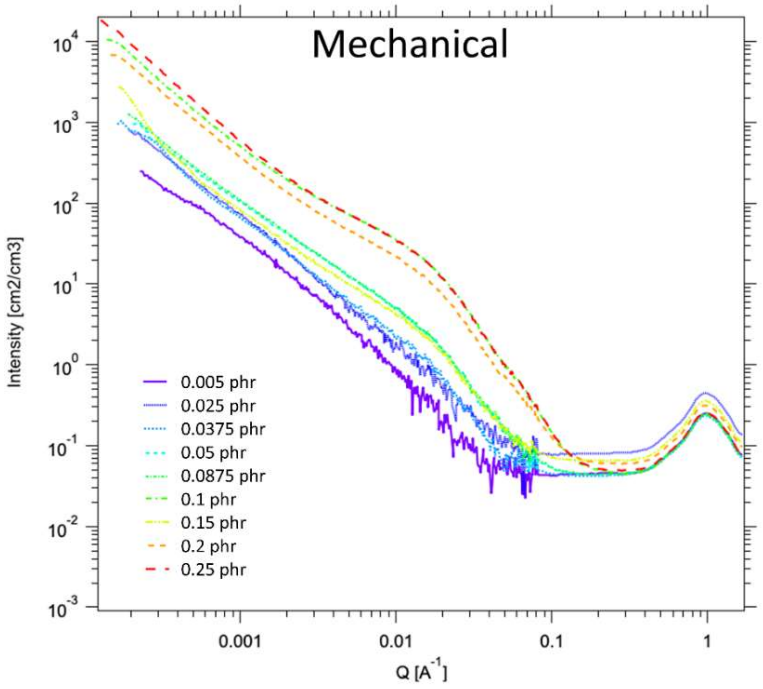

Figure 32 – Intensity versus scattering vector, Q, for mechanical mixing MWCNT/PMMA composites

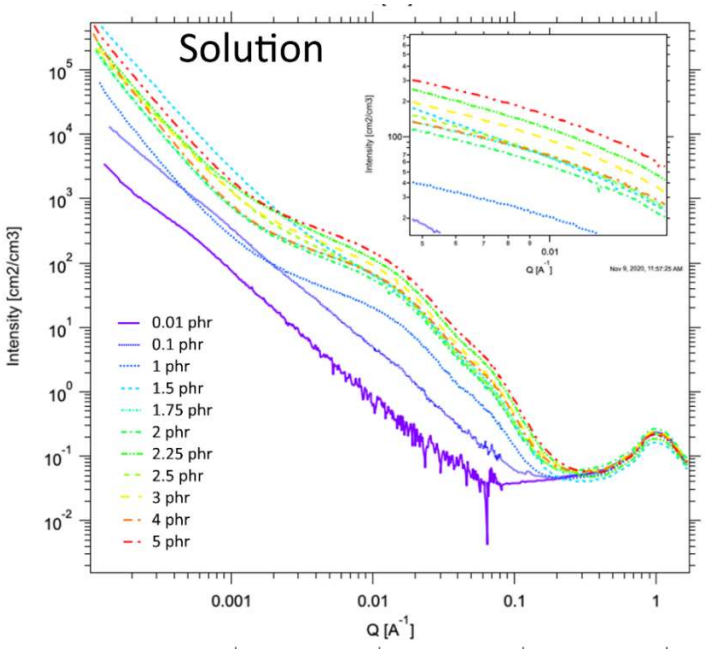

Figure 33 – Intensity versus scattering vector, Q, for solution mixing MWCNT/PMMA composites

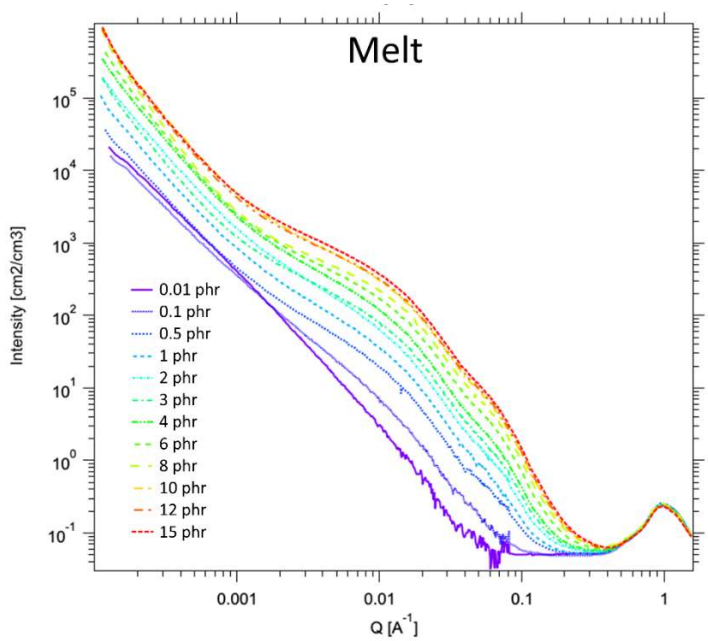

Figure 34 – Intensity versus scattering vector, Q, for melt mixing MWCNT/PMMA composites

Figure 35 show the unified fit data for 8 phr melt mixed CNT/PMMA as a representation of the fit data since it is a good case example. All the data in Figures 32-34 were fit similarly to the data in Figure 35. The data is fit in multiple stages (levels) where the lowest level indicates the smallest features and the highest level indicates the largest features [90]. Level 1 fitting of all composites reveals that the radius of gyration, R_g, is around 3 nm. This may correspond to the MWCNT wall thickness (Figure 11). Level 2 fitting also has the same R_g for all composites. For Level 2, the R_g is around 10 nm which may correspond to the radius of the MWCNT (Table 1). Figure 36 shows the change in R_g (Level 1 and 2) with increasing concentration of MWCNT for all the MWCNT/PMMA composites using all three mixing methods. Overall, there is no significant change in R_g with concentration, which supports the conclusion that the Level 1 and Level 2 R_g values are measuring the wall thickness and radius of the MWCNT. Level 3 and 4 fits for the composites would show larger features and are inconclusive. Since the R_g remains the same for all three mixing methods and at all concentrations, the methods of mixing have not affected the diameters or wall thicknesses of the MWCNT.

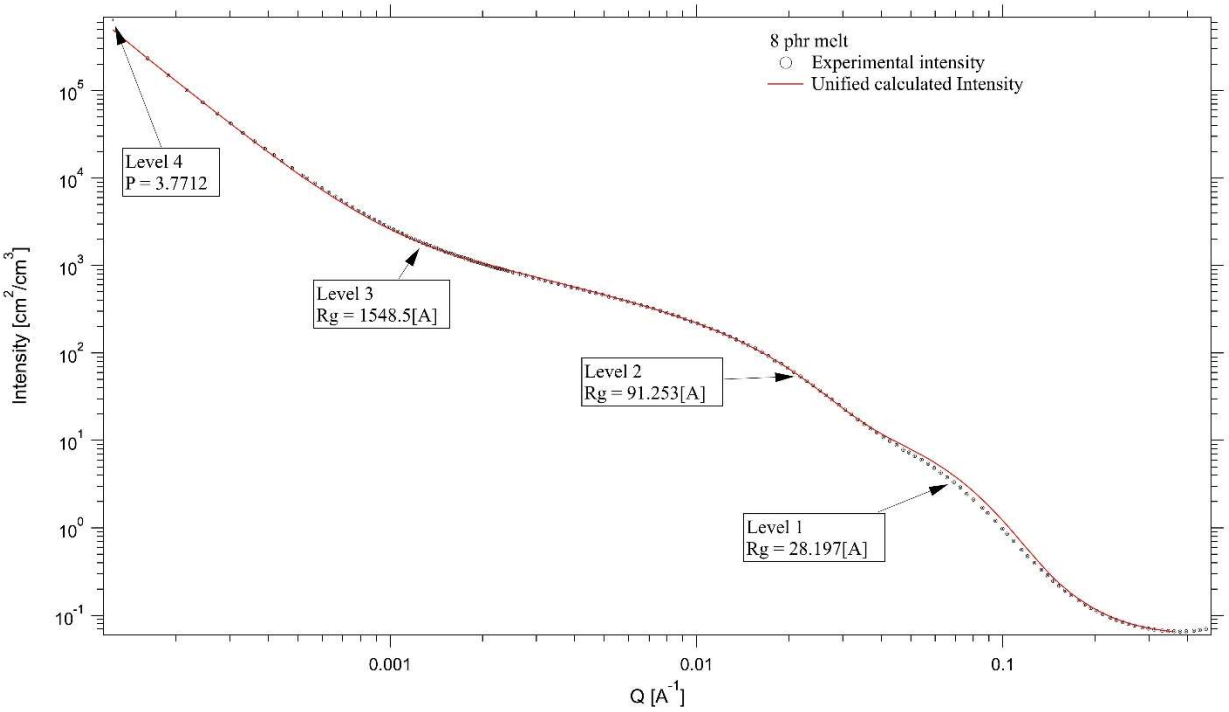

Figure 35 – Intensity versus Q data and unified fit for 8 phr MWCNT/PMMA melt mixed composite

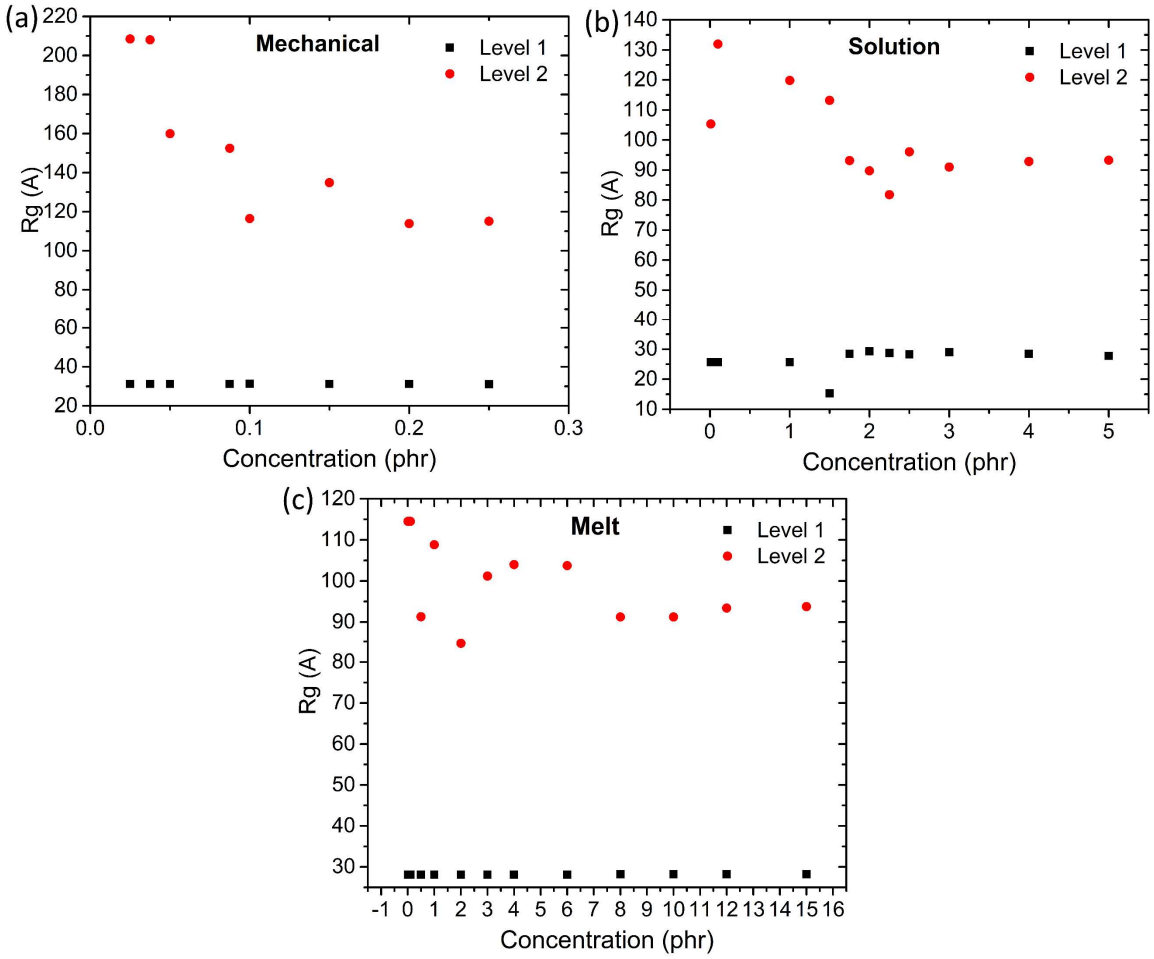

Figure 36 – Radius of gyration of (a) mechanically, (b) solution, and (c) melt mixed MWCNT/PMMA composites

4.3 Electrical Characterization

The impedance properties of the MWCNT powder were explored to give a baseline for the composites. As described in Chapter 2, MWCNT was compressed under increasing pressure from 1 to 325 MPa and the electrical properties were measured in-situ. Figure 37

shows the complex admittance of the MWCNT from 1 to 325 MPa. When lightly compressed at 1 MPa, the conductivity is much lower than at the higher pressures used.

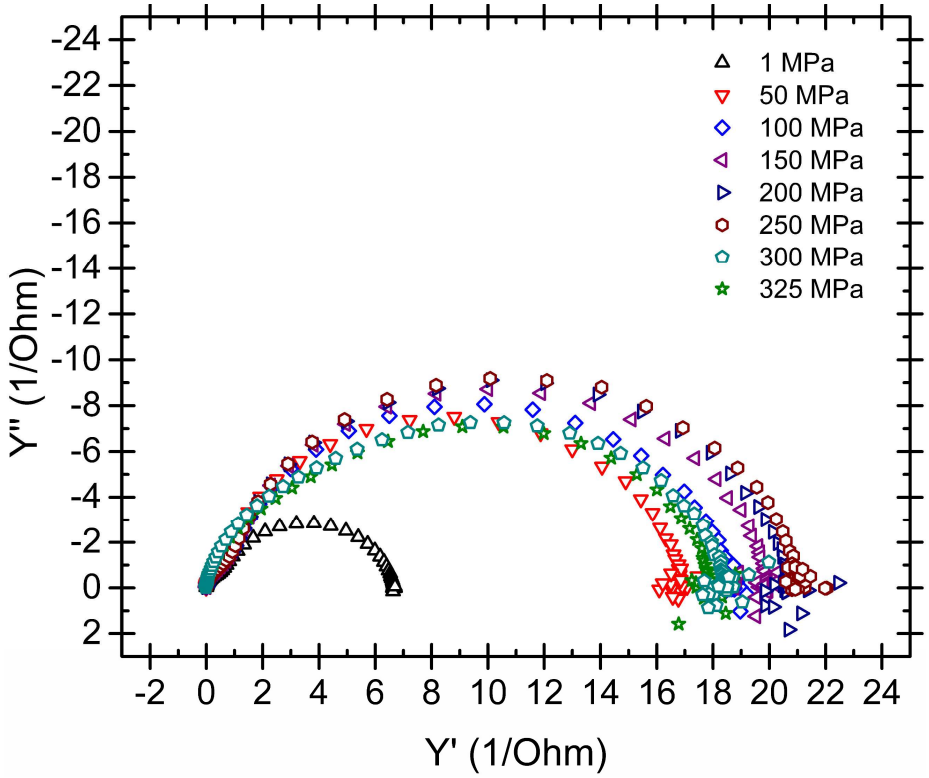

Figure 37 – Complex admittance of MWCNT compressed and measured in-situ at different compaction pressures

Figure 38 displays the impedance magnitude and phase angle versus frequency for all samples made by all three methods [6]. The points shown are an average of at least three samples. For the phase degree graphs, -90° indicates capacitive behaviour, 0° indicates resistive behaviour, and 90° indicates inductive behaviour. In all cases the samples go from capacitive behaviour (-90°) to inductive behaviour (90°) as the CNT content increases as seen in Figure 38 b, d, and f. For mechanical mixing, Figure 38 a-b, the change starts at

0.05 phr. It loses capacitive behaviour until 0.1 phr, where it switches to inductive behaviour. The point where it starts to deviate from capacitive behaviour is the percolation point where the CNTs are starting to form a conductive network. The same behaviour is shown in both the melt and solution mixed samples, starting at 4 and 2 phr, shown in Figure 38 c-d and e-f, respectively. The electrical responses for CNT only and PMMA only samples are included on each graph. It can be seen that the mechanically mixed samples at 0.25 phr ($\sim 10^{1}$ Ω) come the closest to achieving the value of pure CNT impedance ($\sim 10^{-1}$ Ω), but never quite reach it because the amount of MWCNT in the composite is so small.

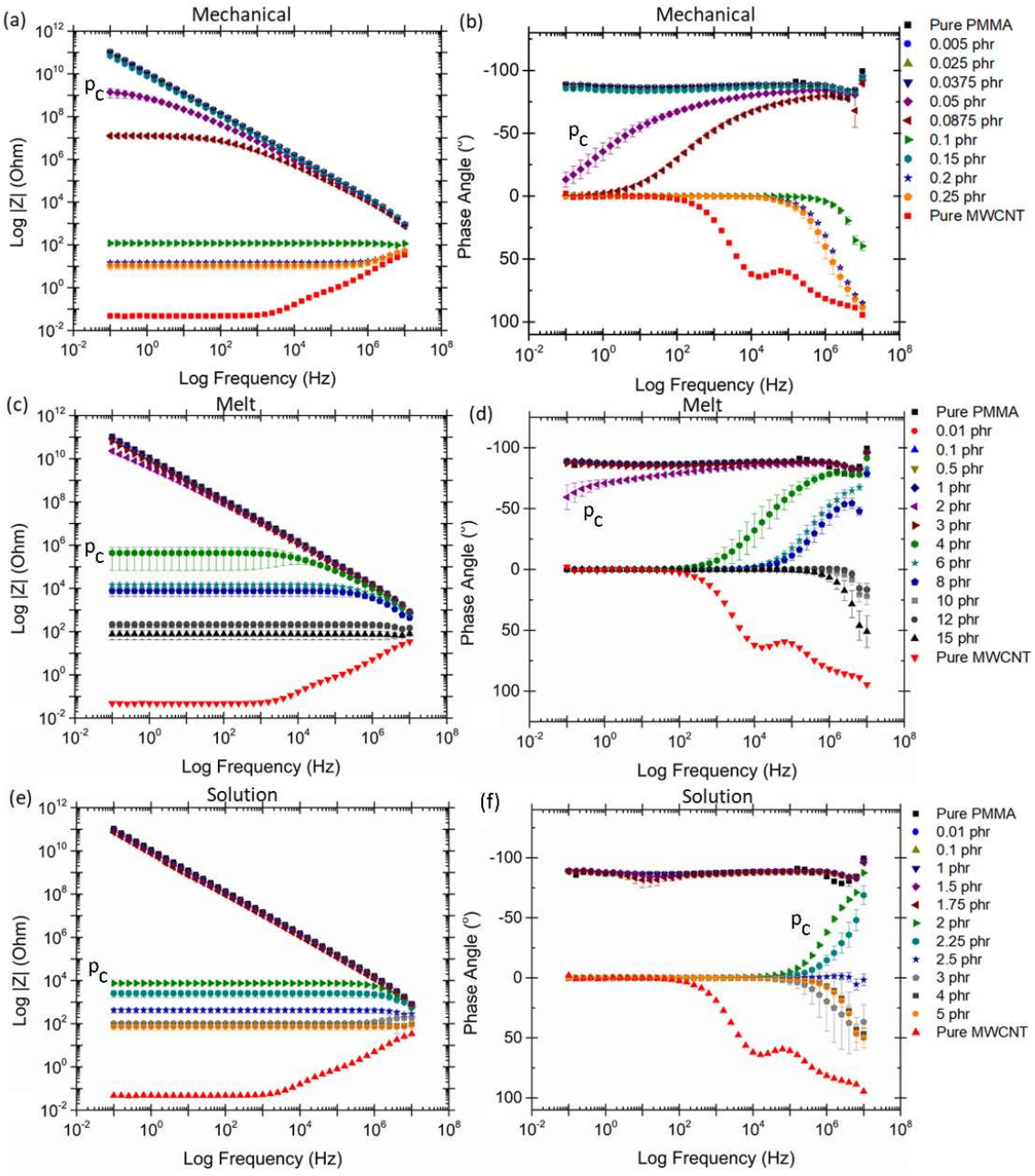

Figure 38 – Impedance magnitude and phase angle vs frequency for (a, b) mechanically, (c, d) melt, and (e, f) solution mixed CNT-PMMA composites. p_c is percolation threshold, updated from [6]

The data in Figure 39 were calculated from the real admittance at 0.1 Hz and sample dimensions. All three methods of mixing at low concentrations of MWCNT match the conductivity of PMMA, while the highest concentrations are close but do not reach the conductivity of pure MWCNT. The graph clearly shows the change from insulating to conducting behavior, or in other words the percolation point, of each set of mixing method samples. Mechanically mixed samples are the first to percolate at around 0.05 phr. The solution mixed samples percolate at about 2 phr, and the melt mixed samples percolate at about 4 phr. Since melt mixing causes an even distribution of MWCNT throughout the PMMA matrix, it requires more MWCNT to form a network. Conversely, mechanically mixing segregates the MWCNT into the boundaries which forms the network at lower concentrations.

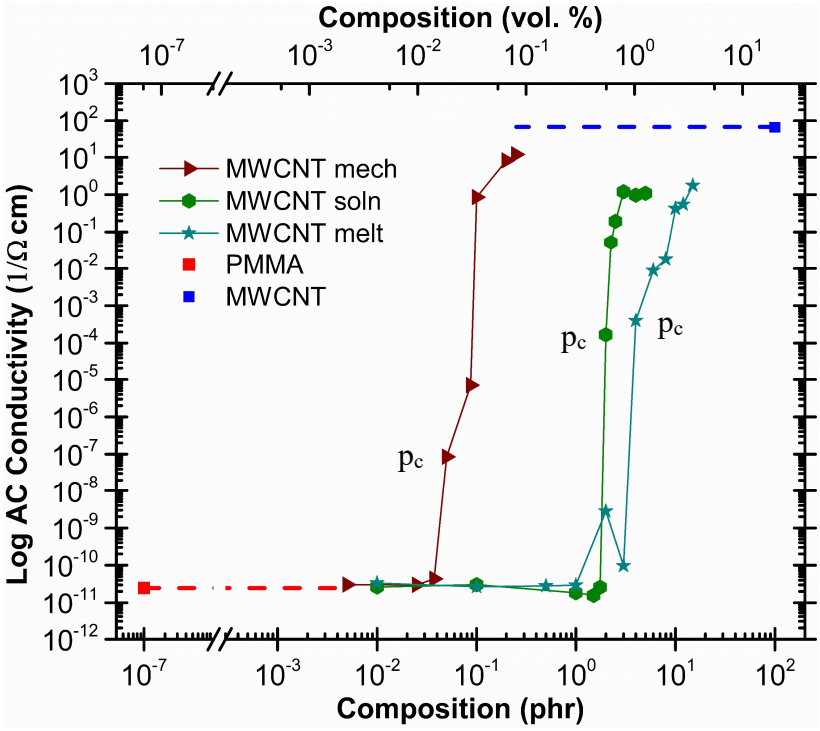

Figure 39 – AC Conductivity versus concentration for MWCNT/PMMA along with PMMA and CNT individually for reference, where p_c is percolation threshold

Percolation theory was applied to the conductivity data to determine the point of percolation more accurately. Equation 1, Section 1.1, is the percolation theory equation used for the calculations.

$$\sigma_M \propto A(p - p_c)^s \tag{1}$$

where σ_M is the property of the mixture, A is a constant, p is the probability of a site (or bond) being filled, p_c is the percolation threshold, and s is an exponent. p and p_c can be thought of in terms of composition (volume % or phr). In the case of MWCNT/PMMA

composites, p is the composition of the conductor in the composite while p_c is the composition required to achieve percolation.

Applying Equation 1 produced the graphs in Figure 40. The equations used ($\sigma_M = y = A(p - p_c)^s, x = p - p_c$), R^2 (accuracy of fit), and percolation threshold, p_c, are in the corner of each graph. The calculated percolation thresholds are 0.087 phr for mechanically mixed, 2.1 phr for solution mixed, and 3.55 phr for melt mixed MWCNT/PMMA composites, which are close to the previous estimates. The two highest concentrations of the solution mixed data were excluded due to a possible second percolation after 3 phr. Incorporating the two highest points results in an unacceptable R^2 value, which suggested that a second percolation occurred. It could be that the first percolation is from agglomerates touching to form a network while the second could be the agglomerates growing further by agglomerates merging as depicted in Figure 41.

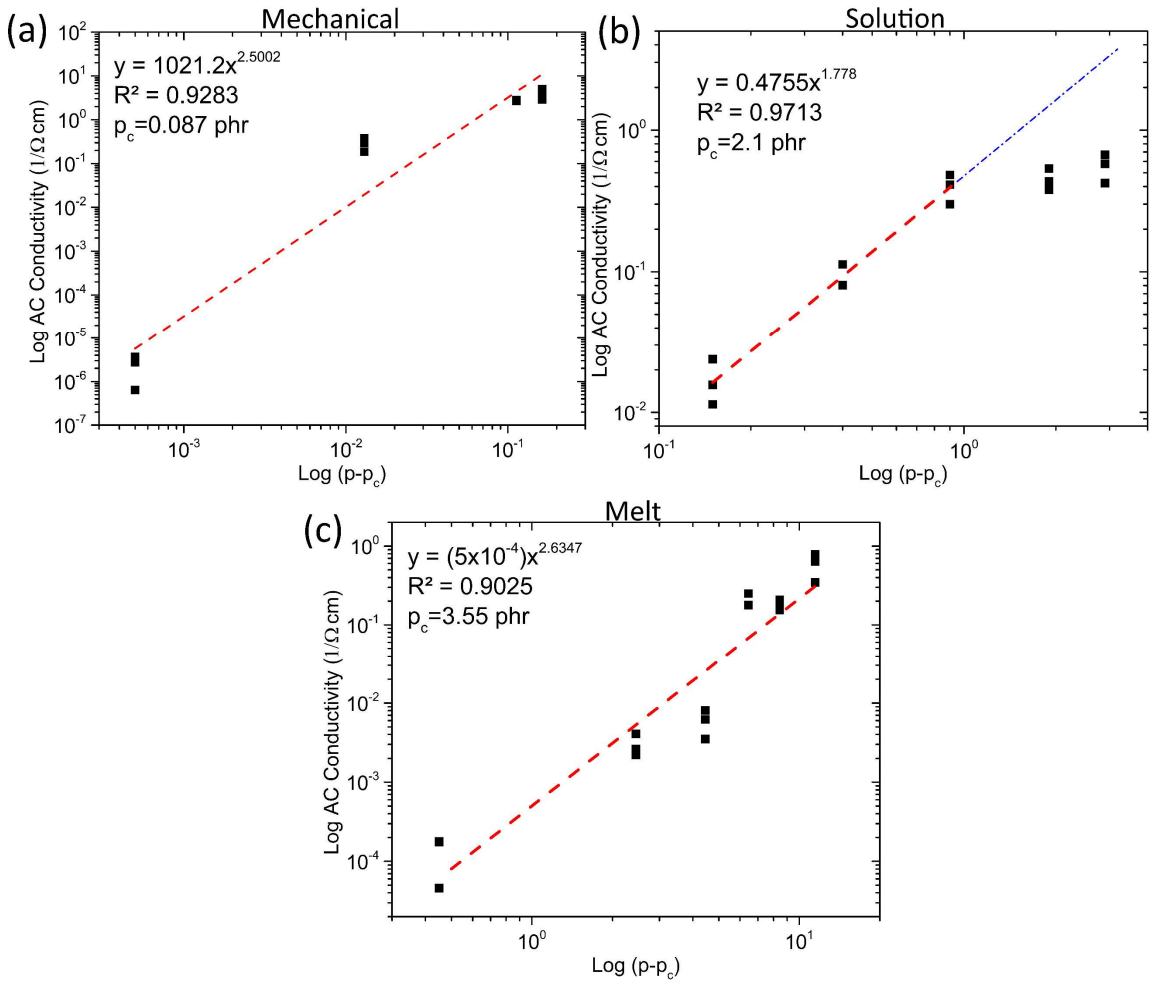

Figure 40 – AC conductivity of MWCNT/PMMA composites fit using percolation theory equations shown in the corners of each graph.

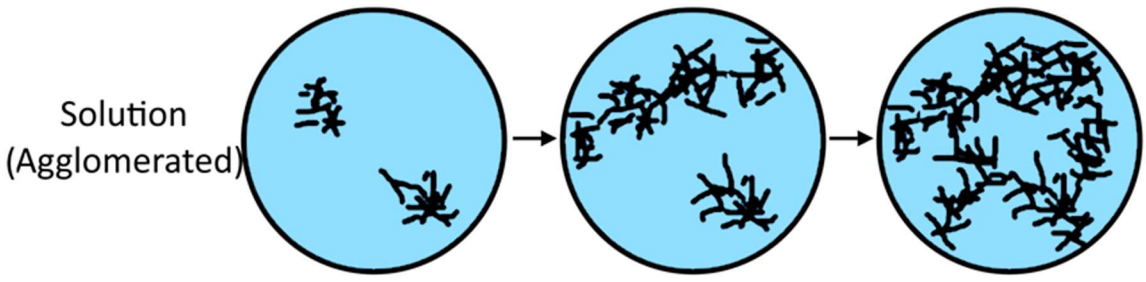

Figure 41 – Schematic of agglomerates forming a network

4.4 Summary

The processing method has a strong effect on the resultant microstructure and properties. The comparison of three different mixing methods revealed three different microstructures with very different electrical properties [6]. The percolation thresholds and maximum conductivity reached is summarized in Table 9. Impedance spectroscopy and percolation theory was used to determine the percolation thresholds to be 0.087 phr (0.049 vol % MWCNT), 2.1 phr (1.16 vol % MWCNT), and 3.55 phr (1.93 vol % MWCNT) for the mechanically, solution, and melt mixed samples, respectively. Solution mixing had a possible second percolation after 3 phr. Optical microscopy, SEM and TEM were used to analyse the microstructure and filler placement. This showed that the mechanically mixed samples had the MWCNT segregated to the boundaries, which resulted in fewer MWCNTs to be used to achieve formation of the percolated network. The melt mixed samples had both agglomerates and distributed MWCNTs which required more MWCNTs to form the network through the matrix material. Lastly, solution mixed samples had agglomerates with a lack of MWCNT in the surrounding area of each. Overall, higher conductivity and lower percolation threshold of the mechanically mixed MWCNT/PMMA composites than the other two is due to the MWCNT being compressed within the PMMA particle boundaries, allowing them to form more connections. The melt mix composites conversely has highly distributed MWCNT that increases the spacing between the MWCNT filler, which increasing the percolation threshold and decreases the conductivity.

Table 9 – Summary of percolation thresholds and conductivity of MWCNT/PMMA composites made using mechanical, melt and solution mixing

Method	Experimental, p_c	Percolation theory, p_c	Highest Conductivity
Mechanical	0.05 phr	0.087 phr	11.85 ± 1.04 $(\Omega\text{-cm})^{-1}$at 0.25 phr
Melt	4 phr	3.55 phr	1.77 ± 0.22 $(\Omega\text{-cm})^{-1}$at 15 phr
Solution	2 phr	2.1 phr	1.09 ± 0.17 $(\Omega\text{-cm})^{-1}$at 5 phr

Overall, this chapter shows that when considering electrical properties, mechanically mixed CNT/PMMA nanocomposites are able to produce resistivity close to that of pure CNT while using only a small amount of MWCNT. This may lead to a reduction in production cost for CNT based technology.

In the next chapter, SiC powders of different sizes are analysed before being incorporated into the composites in Chapters 6 and 7. This is conducted to show how the filler morphology, crystal structure, and contamination may affect the electrical and morphological properties.

5 COMPARISON OF SIC POWDERS TO DETERMINE THE DIFFERENCES IN ELECTRICAL PROPERTIES AND CRYSTAL STRUCTURE

Before creating the composites, the powder differences need to be analysed. In this chapter four types of silicon carbide powders will be compared. Nano-, micron-, and whisker SiC were bought from industry (Table 1), and SiC nanowires were fabricated as described in section 2.5. These four powders were compared using XRD and impedance spectroscopy to determine the base differences between the powders.

5.1 Fabrication of SiC Nanowires

To compare with SiC_w, smaller anistropic SiC (nanowires) were fabricated. Figure 42 shows a TEM image from the first attempt at making SiC nanowires along with an image of the powder fresh out of the furnace. From the TEM image, a strand of MWCNT is visible among the SiC nanowires. The SiC nanowires do not have the visible walls that the CNT does and therefore are easy to distinguish.

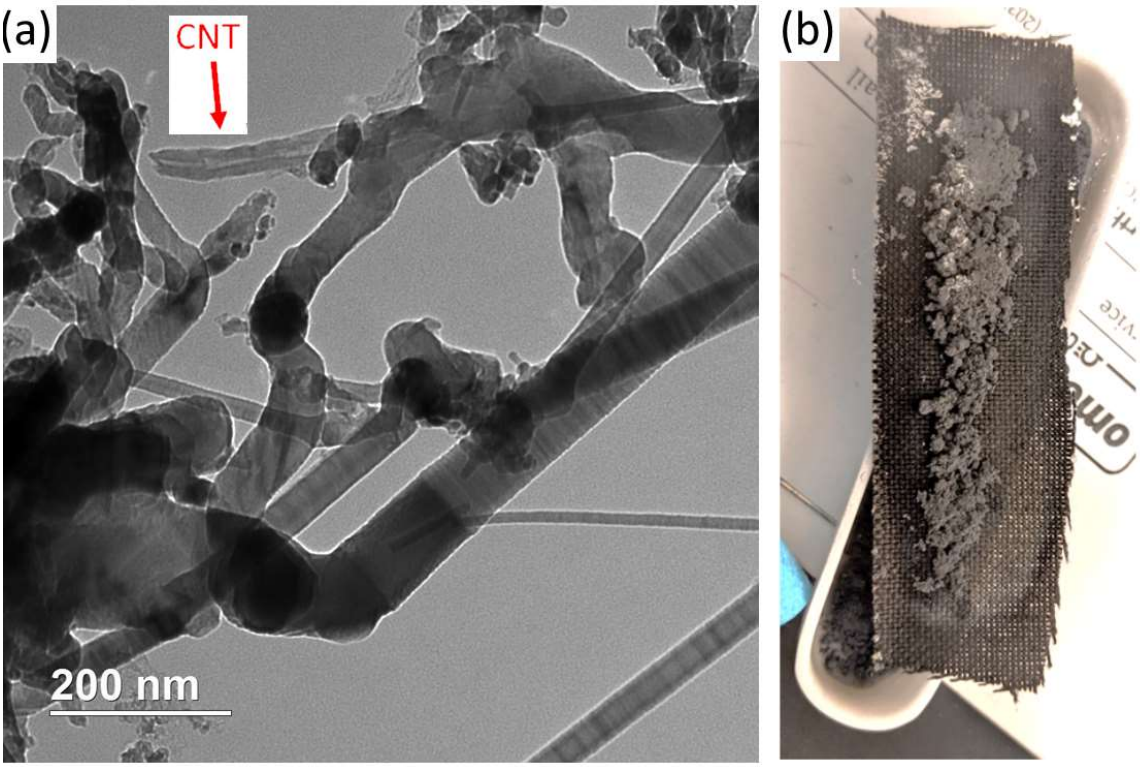

Figure 42 – The first attempt at making SiC nanowires. (a) TEM of SiC nanowires made from CNT and (b) SiC nanowire powder upon removal from furnace

To reduce the amount of untransformed carbon nanotubes, the hold time within the furnace was increased from 6 to 8 hours. There was still some carbon contamination despite the increase in time as can be seen in Figure 43b. Another noticeable difference is that the SiC nanowires have a capped end unlike the MWCNT (Figure 43a).

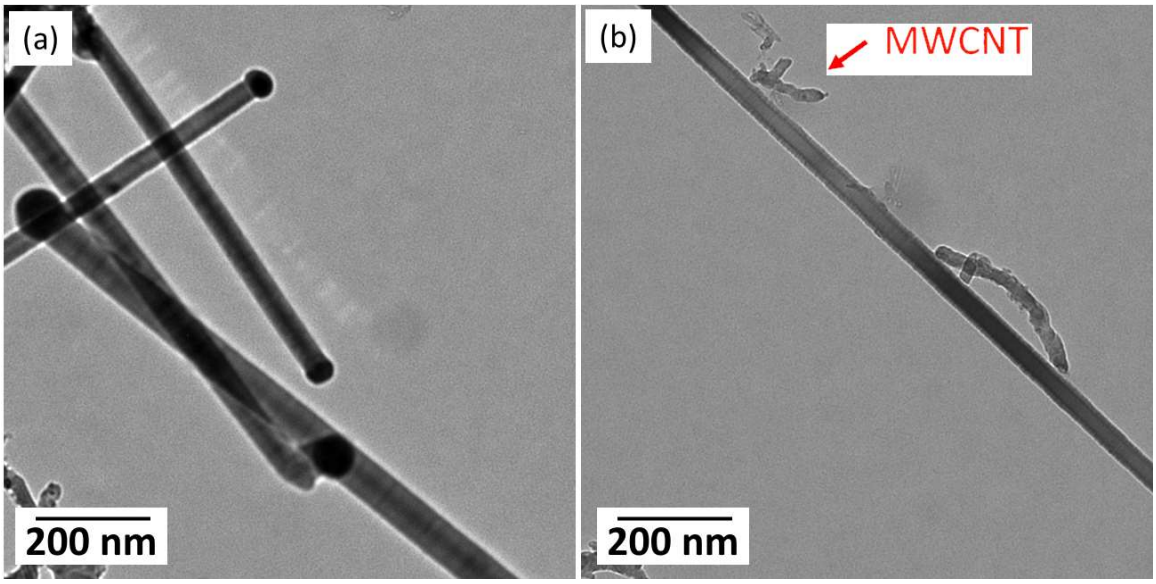

Figure 43 – TEM images of SiC nanowires made from MWCNT

From multiple TEM images, the diameters of the SiC nanowires and MWCNT were determined by measuring 135 and 155 diameters respectively. The average and standard deviations are shown in Table 10. Overall, the SiC nanowires are slightly larger than the MWCNTs that they were made from.

Table 10 – Sizes of MWCNT and SiC nanowires

Powder	Avg. diameter (nm)	Max. diameter (nm)	Min. diameter (nm)
MWCNT	20 ± 8	63	5
SiC nanowires	32 ± 20	122	10

To verify that the composition is correct, FTIR was used to compare spectra of SiC whiskers, nanowires and carbon nanotubes. The results are shown in Figure 44. It is obvious that the silicon carbide nanowires match the SiC whiskers.

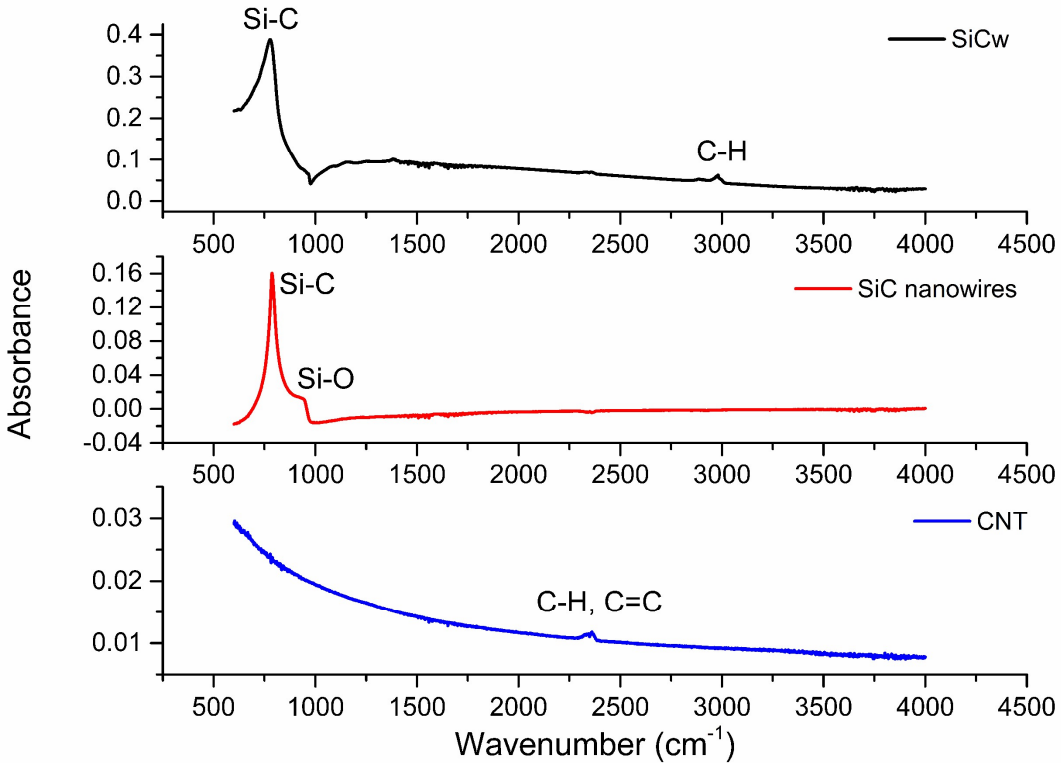

Figure 44 – FTIR of SiC_w from Advanced Composite Materials, SiC nanowires made from MWCNT, and MWCNT

5.2 Silicon Carbide Phase Characterization by X-ray Diffraction

Since silicon carbide may have four different crystal structures, XRD was used to verify that the silicon carbides used were all β-SiC [91, 92]. The XRD results for the SiC powders are shown in Figure 45 with an enlarged view in Figure 46. Overall, all the SiC

powders are β-SiC (111, 200, 220, 311, and 400 peaks); however, there are some impurities. Both micron-SiC and SiC_w have peaks (6H 101, 103, and 109) that correspond with α-SiC (6H). Both the nano-SiC and SiC nanowires have peaks (labelled as SF) that correspond to stacking faults. Lastly, the micron-SiC and SiC nanowires show a peak (labelled as carbon) that represents carbon contamination (Figure 46) which is expected for the nanowires from its method of fabrication.

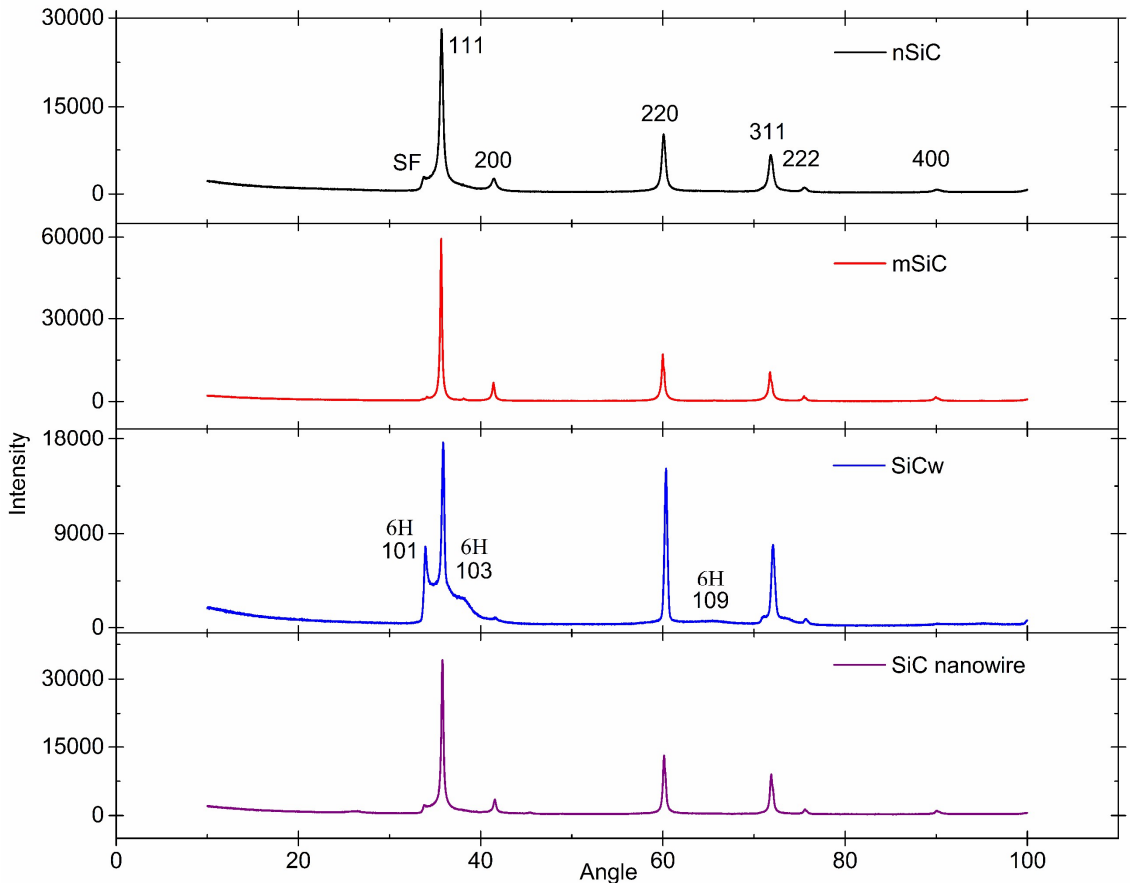

Figure 45 – XRD of nano-, micron-, whisker, and nanowire SiC powders

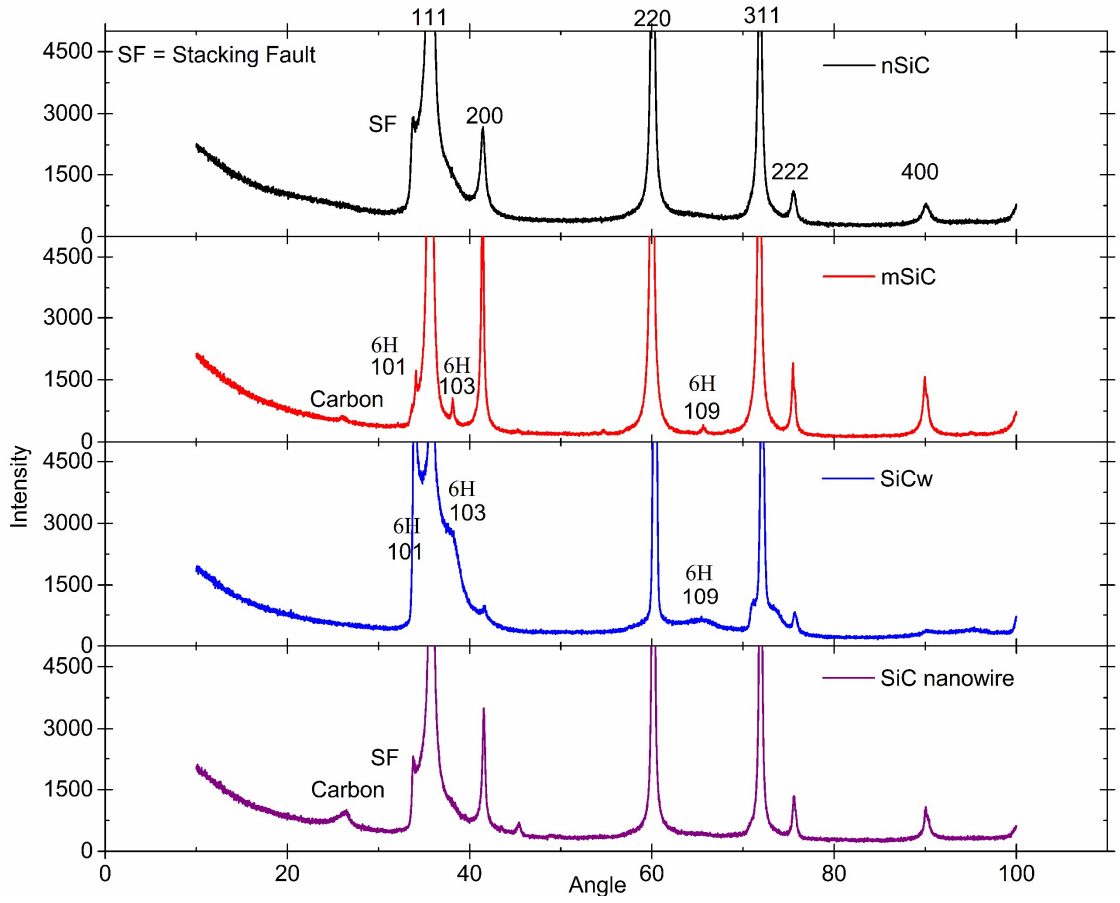

Figure 46 – Enlarged view of XRD of nano-, micron-, whisker, and nanowire SiC powders

Table 11 shows the reported impurities of each of the silicon carbide powders that could cause further differences in properties in addition to the crystal structures.

Table 11 – Reported impurities of the SiC powders

Particle	Impurities	Source
SiC_w	Free C: 0.05-0.3% SiO_2: 0.35-0.75%	Advanced Composite Materials
Micron-SiC	0.2% max metal impurities	Alfa Aesar
Nano-SiC	Free C: 0.76% Free Si: 0.24%	US Research Nanomaterials, Inc
SiC nanowires	Carbon contamination	This work

5.3 Silicon Carbide Particle Impedance Response

As a baseline, the conductivities of each silicon carbide powder that was compressed at 350 MPa using the die shown in Figure 21 were determined from the impedance magnitude at 0.1 Hz. The conductivities of whisker, nano-sized, micron-sized, and nanowire SiC powders were 2.43 x 10^{-3}, 5.89 x 10^{-3}, 4.45 x 10^{-2}, and 0.169 1/Ω-cm, respectively. The impedance magnitudes and phase angles of each SiC powder are shown in Figure 47. The sizes are similar so the data in the graphs are comparable. The same trend is visible with SiC_w as the most resistive and the SiC nanowires as the most conductive.

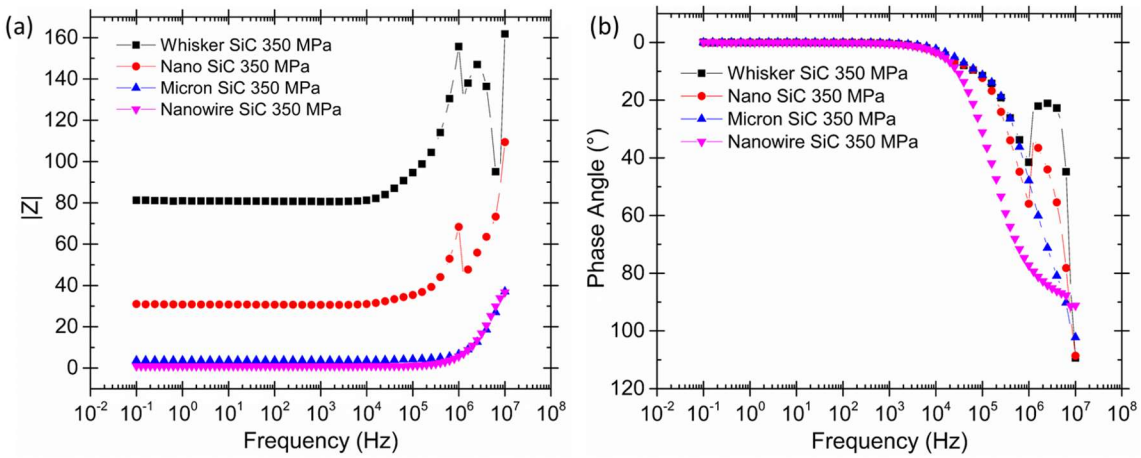

Figure 47 – Impedance magnitude and phase angle of whisker, micron-sized, nano-sized, and nanowire SiC powder compressed at 350 MPa and measure in-situ

Figure 47 made a comparison at 350 MPa. This pressure was selected after testing from 25-350 MPa as it formed the most connections between the MWCNTs. Overall, the patterns of the SiC powders are the same as pressure is increased as can be seen in the complex impedance graphs within Figure 48. The point where the data curves meet the Z' axis indicates the resistance value. The change from semicircles in the first quadrant to a vertical line in the fourth quadrant indicates a change from capacitive to inductive behavior, while the decrease along the Z' axis indicates decreasing resistive behavior [65]. This is a result of the increased pressure causing an increase in contact points. The micron SiC powder is more conductive than the whisker or nano-SiC powders. Figure 49 shows the complex impedance graph for the SiC nanowires which did not show the same change (semicircles to vertical lines) as the other SiC powders and immediately showed a conductive response (vertical line in 4th quadrant).

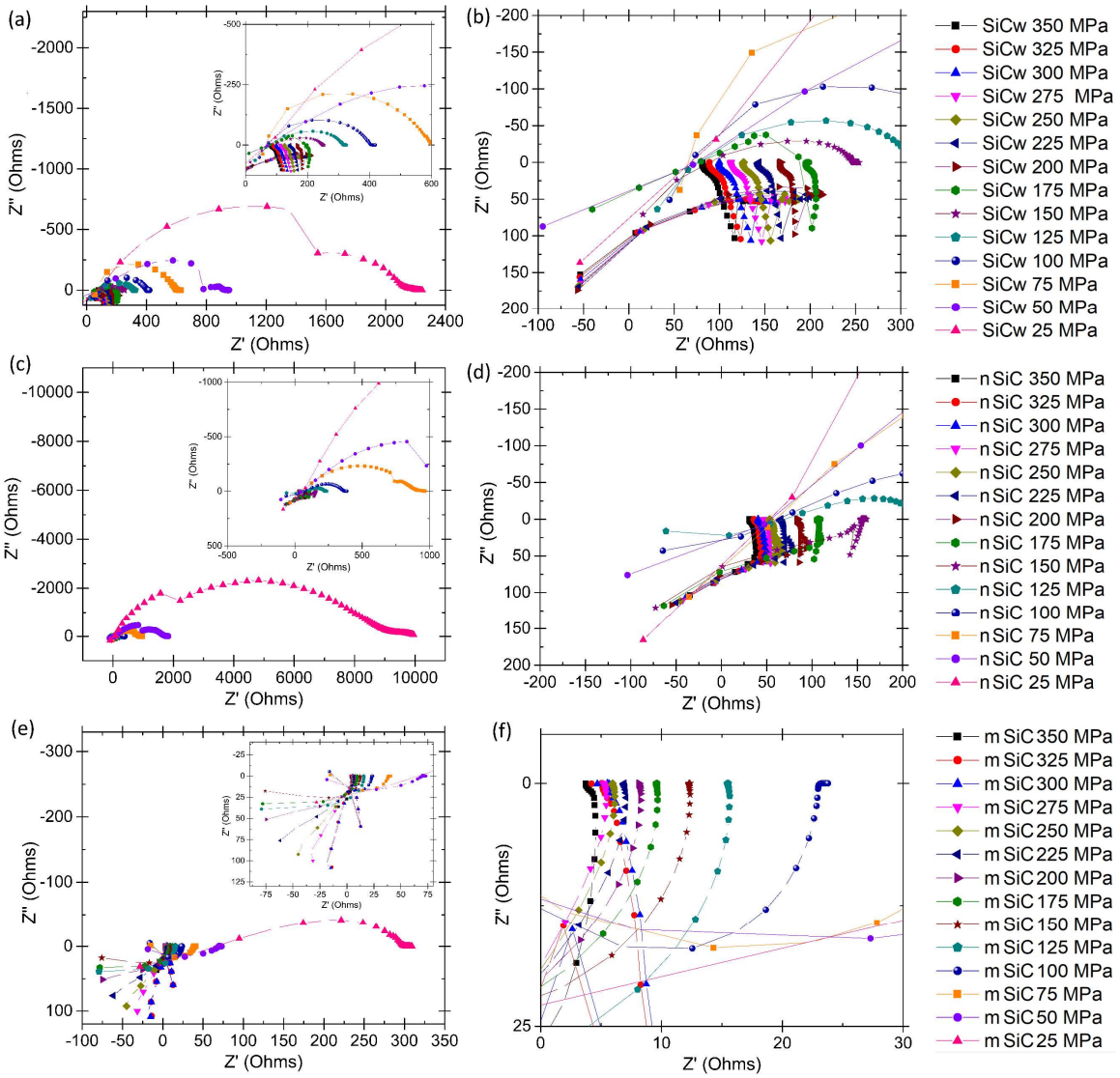

Figure 48 – Complex impedance of (a-b) SiC_w, (c-d) nano-SiC, (e-f) micron-SiC powder compressed and measured in-situ, with insets at intermediate magnification

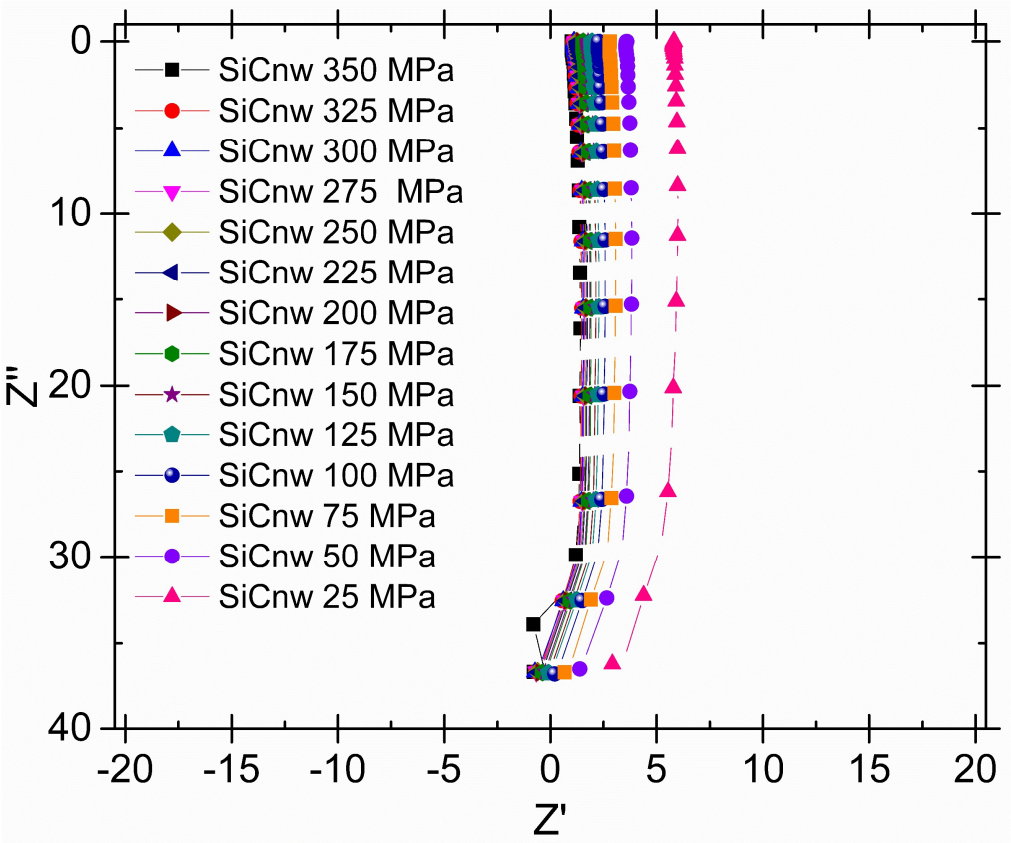

Figure 49 – Complex impedance of silicon carbide nanowire (SiC_{nw}) powders compressed and measured in-situ

5.4 Summary

This chapter compared the XRD and impedance of four silicon carbide powders of different morphologies. First the nanowire SiC was fabricated and compared to SiC whiskers that were bought commercially. FTIR showed little difference between the two anisotropic powders. Next all four SiC powders were compared using XRD and found to overall be considered β-SiC crystal structures. However, micron and whisker SiC had some α-SiC (6-hexagonal) peaks. Finally, the powders were pressed and electrically measured

in-situ using impedance spectroscopy. The nanowire SiC powder showed as the most conductive powder with micron-sized SiC a close second. It should be noted that both of those powders had carbon contamination peaks showing in the XRD data. With the knowledge of the differences between the powders, a more accurate comparison between SiC composites may be made.

In the next chapter, nano-, micron- and whisker SiC / PMMA composites will be examined using impedance spectroscopy and microscopy. This will show the effect of filler size on the electrical measurements and microstructure which will later (Chapter 9) be used to fit equivalent circuits.

6 EFFECT OF PARTICLE SHAPE ON THE ELECTRICAL AND MICROSTRUCTURAL PROPERTIES (SIC/PMMA)

The shape of the filler particles also has a strong effect on the connectivity of the conductive filler network. The ratio between filler and matrix particle size needs to be taken into account. In this section, three types of SiC (nano-sized, micron-sized, and whisker) within PMMA matrices will be studied. Since the same size PMMA will be used in all cases, a direct comparison between the composites is possible.

6.1 Microstructure of SiC/PMMA Composites

Since the SiC/PMMA composites were made using mechanical mixing via a blender, they form segregated network, grain-like microstructures seen in Figure 50 [58]. At low concentrations (0.1 phr), the SiC/PMMA samples are partially transparent. Overall, nano-sized SiC / PMMA composites have the most defined microstructure (Figure 50 a and d) since the small particles were easier to segregate into the boundaries. In contrast, the SiC_w was unable to fully segregate into the boundaries (Figure 50 c and f) due to the length being more similar to the size of PMMA (10-100 μm, Table 1). The micron- SiC / PMMA composites fall between the other two sizes since micron-SiC does segregate but not as clearly as nano-SiC (Figure 50 b and e).

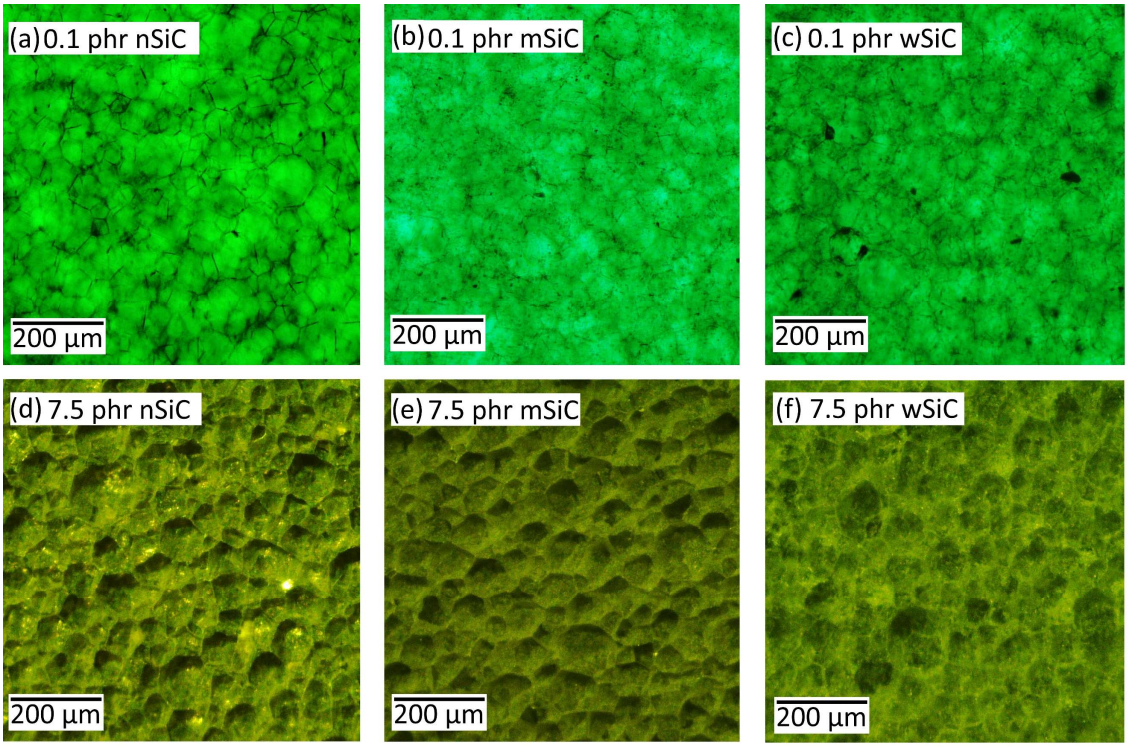

Figure 50 – Microstructures of SiC/PMMA composites before percolation at 0.1 phr and after percolation at 7.5 phr for (a,d) nano-sized, (b,e) micron-size, and (c,f) whisker SiC [58]

6.2 Electrical Characterization of SiC/PMMA Composites

The impedance magnitude and phase angle data of the SiC powders discussed in the previous section are included in Figure 51 along with PMMA data for comparison. From Figure 51, it is observed that the SiC/PMMA composites (lowest $|Z| \sim 10^6\ \Omega$ at 0.1 Hz) do not come close to the conductivity of pure SiC ($|Z| \sim 10^1$ at 0.1 Hz) for all three sets of composites. The percolation is observed by the flattening of the curves in |Z| at low frequencies or the first deviation from -90° in phase angle. The percolation points of nano-

, micron-, and whisker SiC are estimated to be 2 phr, 7.5 phr, and 10 phr, respectively. The overall trend indicated by the phase angles (Figure 51 b, d, and f) is a decrease in capacitive behavior (deviation from -90°) with increasing composition. It does not reach 90° which indicates a lack of inductive behavior.

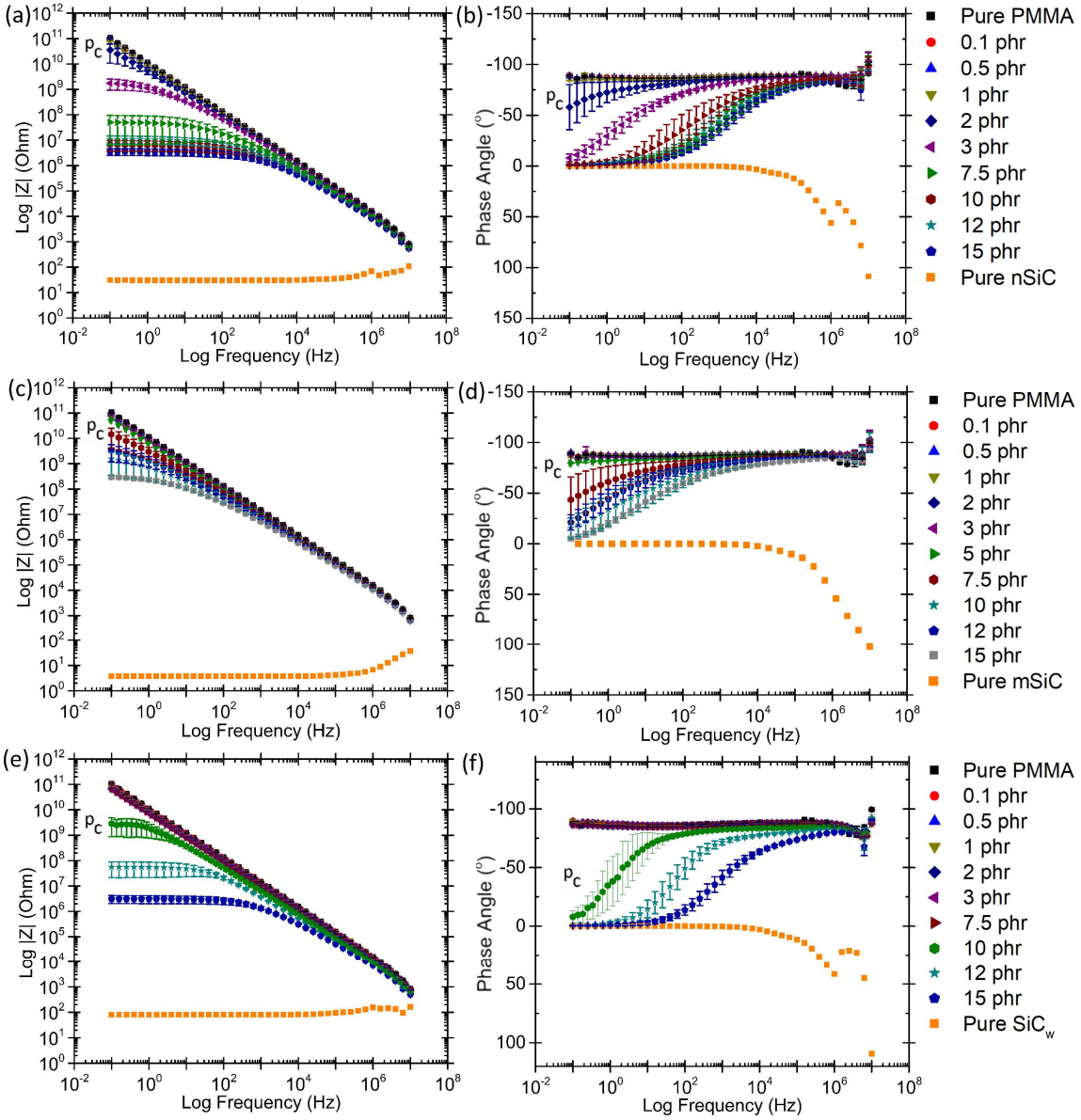

Figure 51 – Impedance magnitude and phase angle vs frequency for (a, b) nano-sized, (c, d) micron-sized, and (e, f) whisker SiC-PMMA composites, where p_c is percolation threshold

Figure 52 shows the average conductivity versus concentration for 3-5 samples the SiC/PMMA composites (with standard deviations). The nano-SiC composite achieved percolation (increase in conductivity) at the concentration of 2 phr while the whisker SiC achieved percolation at the higher concentration of 10 phr. Despite this, both reached the same maximum conductivity (for the concentrations tested). Micron-sized SiC never reached the same conductivity. Two samples were made using a similar mechanical mixing method at 25 phr for the micron-SiC/PMMA, which averaged to about the same conductivity as the 15 phr micron-SiC/PMMA. A mentioned in Chapter 5, the micron-sized powder has a higher conductivity than the nano-sized and whisker SiC. Despite that, the micron-SiC/PMMA composites had the lowest conductivity of all the SiC/PMMA composite sets, presumably because there was an issue with forming the conductive network with micron-SiC. The larger size of the micron-SiC (1-2 μm, Table 1) without anisotropy may have allowed the PMMA to interfere with the connectivity of the SiC since the micron-SiC would have a more difficult time segregating to the boundaries of the PMMA particles.

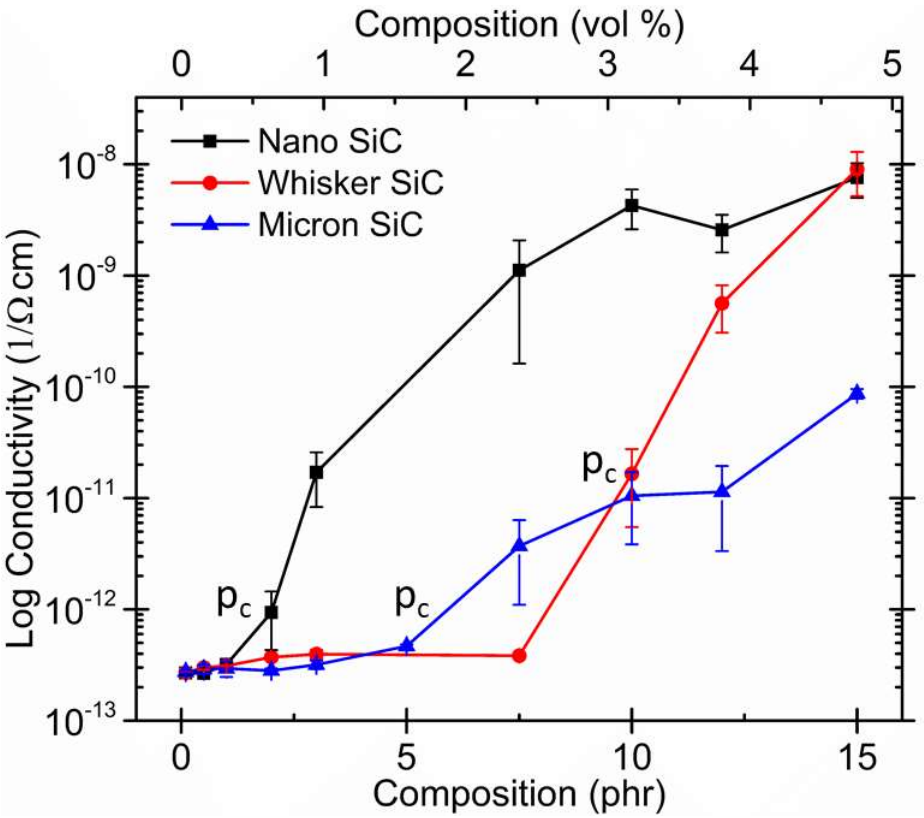

Figure 52 – Conductivity of SiC/PMMA composites as a function of SiC content. p_c is percolation threshold, updated from [58]

Percolation theory (Equation 1) was applied to the data in Figure 52 to determine the percolation threshold. The equations used ($\sigma_M = y = A(p - p_c)^s, x = p - p_c$), R^2 (accuracy of fit), and percolation threshold, p_c, are in the corner of each graph in Figure 53. The percolation thresholds are 2.35 phr for nano-SiC, 2.1 phr for micron-SiC, and 9.8 phr for whisker SiC composites. For the micron-sized SiC composite, this is a large difference from estimating by looking at the graph in Figure 52. This difference may be able to be reduced by creating more samples in the 2-5 phr range. A possible reason for the difference may be the rigidity and larger powder size of the micron-SiC. It should also be noted that

the micron-SiC composite percolation fit has an R^2 of 0.708, indicating that the fit is not very accurate, most likely due to the reasons listed earlier.

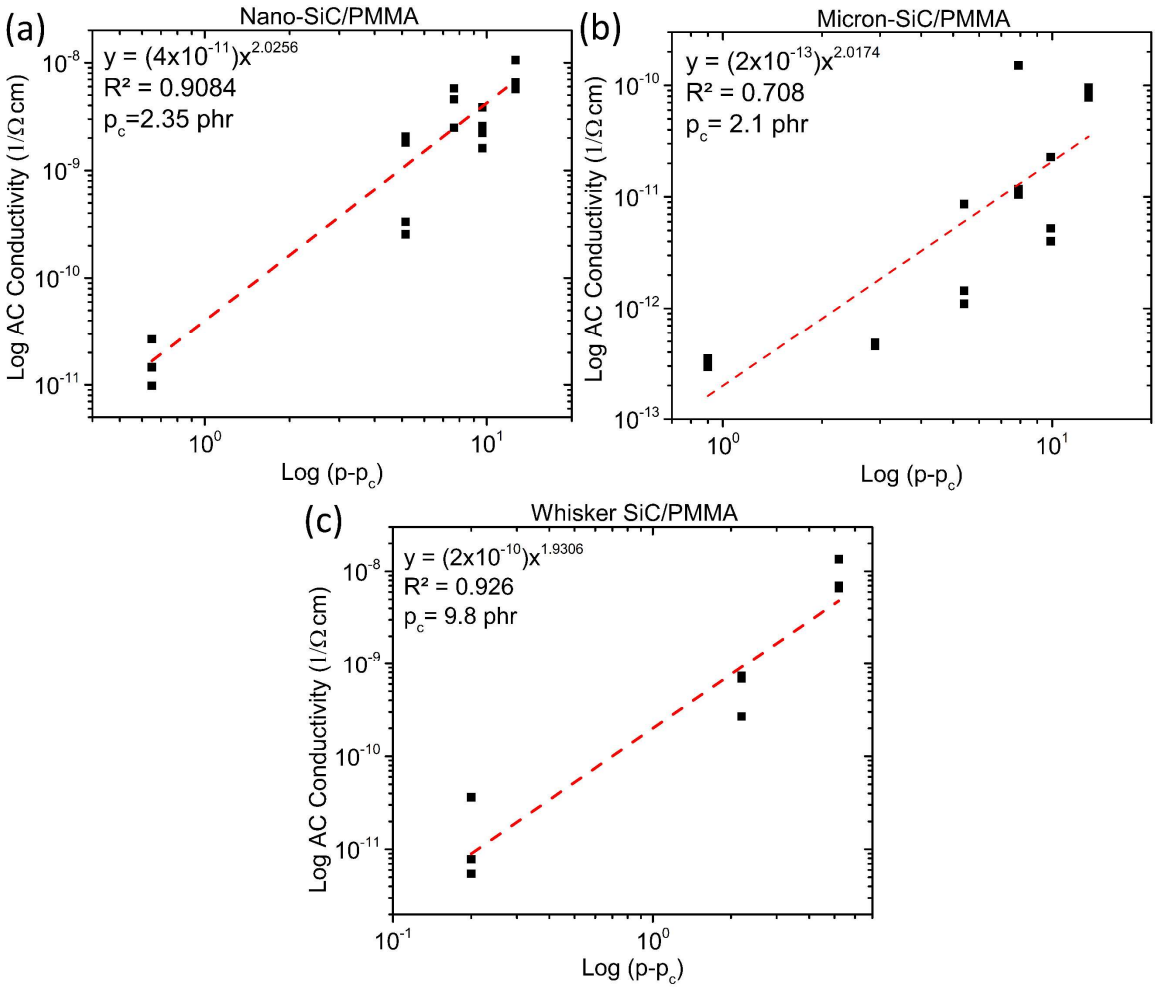

Figure 53 – AC conductivity of SiC/PMMA composites fit using percolation theory equations shown in the corners of each graph.

The crystal structure, size difference, and impurities of the three SiC powders used as fillers in the chapter all have an effect on the resultant properties. The combination of these factors resulted in different electrical properties of the powders (Figure 47) which

then are compounded by the change in filler morphology within the composites. Table 12 summarizes these factors.

Table 12 – Summary of crystal structure, size, and impurities for SiC powders

Particle	Crystal Structure	Size	Impurities
SiC_w	β- Cubic with α (6 Hexagonal, 6H) contamination	L: 10-50 μm, D: 1 μm	Free C: 0.05-0.3% SiO_2: 0.35-0.75%
Micron-SiC	β- Cubic with α (6 Hexagonal, 6H) contamination	1-2 μm	0.2% max metal impurities
Nano-SiC	Cubic with stacking faults	10-70 nm	Free C: 0.76% Free Si: 0.24%

6.3 Summary

Three types of silicon carbide were used to make PMMA composites in order to determine the effect of particle morphology on the electrical and morphological properties. All the composites formed segregated network microstructures since they were made using mechanical mixing. The nano-SiC formed the most defined network, while the SiC whiskers broke out of the PMMA network boundaries due to their length. Using impedance spectroscopy and percolation theory, the percolation thresholds were determined to be 2.35 phr for nano-SiC, 2.1 phr for micron-SiC, and 9.8 phr for whisker SiC composites. There is a large difference for the micron-SiC between the percolation threshold determined by estimation from the conductivity graph (5 phr) and percolation theory (2.1 phr). Overall, the nano-SiC composites were the most reliable, had the lowest percolation, and highest conductivity.

Table 13 – Summary of percolation thresholds and conductivity of nano-, micron-, and whisker SiC/PMMA composites

Particle Size	**Experimental, p_c**	**Percolation theory, p_c**	**Highest Conductivity**
Nano	2 phr	2.35 phr	$7.62 \times 10^{-9} \pm 2.61 \times 10^{-9}$ $(\Omega\text{-cm})^{-1}$ at 15 phr
Micron	5 phr	2.1 phr	$8.70 \times 10^{-11} \pm 8.57 \times 10^{-12}$ $(\Omega\text{-cm})^{-1}$ at 15 phr
Whisker	10 phr	9.8 phr	$9.04 \times 10^{-9} \pm 3.88 \times 10^{-9}$ $(\Omega\text{-cm})^{-1}$ at 15 phr

This chapter showed that SiC_w /PMMA composites had the highest percolation; however, the MWCNT/PMMA composites from Chapter 4 had low percolation and were also anisotropic in shape. Therefore, Chapter 7 will compare SiC nanowires (32 nm in diameter) and whiskers (1 μm in diameter) to determine the effect of anisotropic filler size on the overall electrical and microstructural properties.

7 EFFECT OF PARTICLE SIZE ON ELECTRICAL AND MICROSTRUCTURAL PROPERTIES (SIC/GLASS)

Past work suggested that high aspect ratio particles would achieve lower percolation concentrations [62, 63, 93]. The ratio of the size of the filler and matrix particles is important. Chapter 6 showed that while the SiC whiskers have a high aspect ratio, their length (10-50 μm) was too similar to the size of the PMMA particles (50 μm) to easily segregate to the boundaries of the PMMA particles. This chapter will use two sizes of anisotropic SiC whiskers in a glass matrix to study the effect of anisotropic filler size on electrical and microstructural properties. The size of the glass (45-53 μm) is about the average of the range of the PMMA particles (10-100 μm), as listed in Table 1. A SiC nanowires (32 nm), which are closer in size to the MWCNT (20 nm), will be used to prove that smaller anisotropic SiC will reduce the percolation threshold within segregated network composites.

7.1 Microstructure of SiC Whisker and Nanowire/Glass Composites

Figure 54 shows microstructures of SiC_w-glass composites at 0.1, 1, 5, and 12.5 phr. Since the SiC_w is larger than the CNT used in this work, the microstructure is not as defined as for the ones made with CNT. The microstructures are grain-like since the glass was created at specific temperature (610°C) and pressure conditions (23.4 MPa) that made the glass matrix deform due to lower viscosity but not decrease the viscosity enough so that the filler enters the glass [82]. SiC_w agglomerates, as seen in Figure 54b, were seen to

form starting at 1 phr. As the concentration increased SiC_w becomes even more visible in the microstructure.

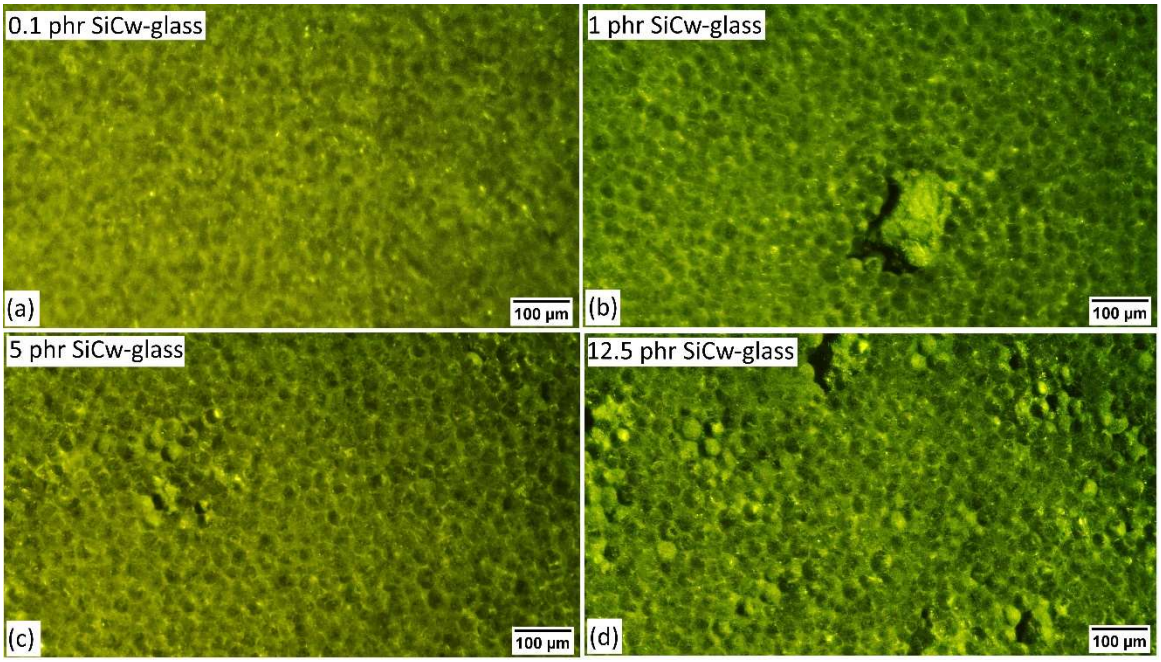

Figure 54 – Optical microscope pictures of SiC_w-glass composites at (a) 0.1, (b) 1, (c) 5, and (d) 12.5 phr

A few samples were selected based on their electrical properties (section 7.3) for SEM imaging to get a clearer idea of the placement of the SiC_w within the glass matrix. Figure 55 a and e show the microstructure of a 0.25 phr SiC_w/glass composite which does not appear to have any visible SiC_w. Conversely, the 7.5 phr composite shown in Figure 55 b and f shows that the SiC_w are along the edges of the grains, which is easiest seen when looking at where a glass bead appeared to have pulled out during polishing. Figure 55 c-d and g-h are the same composition of 10 phr. However, Figure 55 c and g are a cross-section

of a sample that was cut with a diamond blade. The SiC_w is visible but harder to spot since the act of cutting the sample appears to have fractured the glass. Figure 55 d and h show a sample made using newly bought borosilicate glass mixed with SiC_w using a speedmixer and without ball-milling as previously done. The micrographs show again that the SiC_w is relegated to the grain-like boundaries. From the exposed locations where the SiC_w are more visible, the SiC_w appears to be directionally oriented along the grains but pointed randomly in that plane.

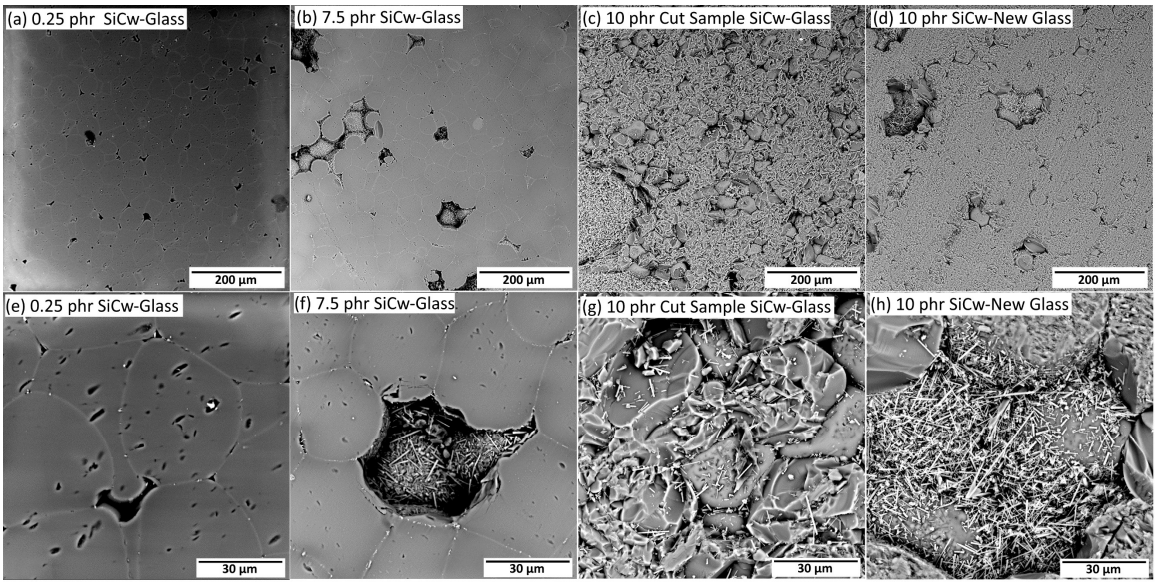

Figure 55 – SEM images of (a,e) 0.25 phr, (b,f) 7.5 phr, and (c,g) 10 phr cut sample SiC_w/glass composites and (d,h) 10 phr SiC_w /glass composites made with recently bought glass and no ball-milling.

Figure 56 shows the optical photographs of the microstructures of (a,b) below, (c,d) at and (e,f) above percolation samples of SiC nanowires/glass composites. Below

percolation (0.325 phr), the microstructure appears sintered. At percolation (1 phr), the glass particles appear more rounded and less sintered than before percolation. Despite being made at the same temperature and pressure as the SiC_w/glass composites, the SiC nanowire/glass composites appear less sintered and are more fragile at higher concentrations (at and after percolation) than the SiC_w/glass composites. At 4 phr, the samples were easily broken by hand, so no higher concentrations were made. After percolation, agglomerates are clearly seen in the microstructure.

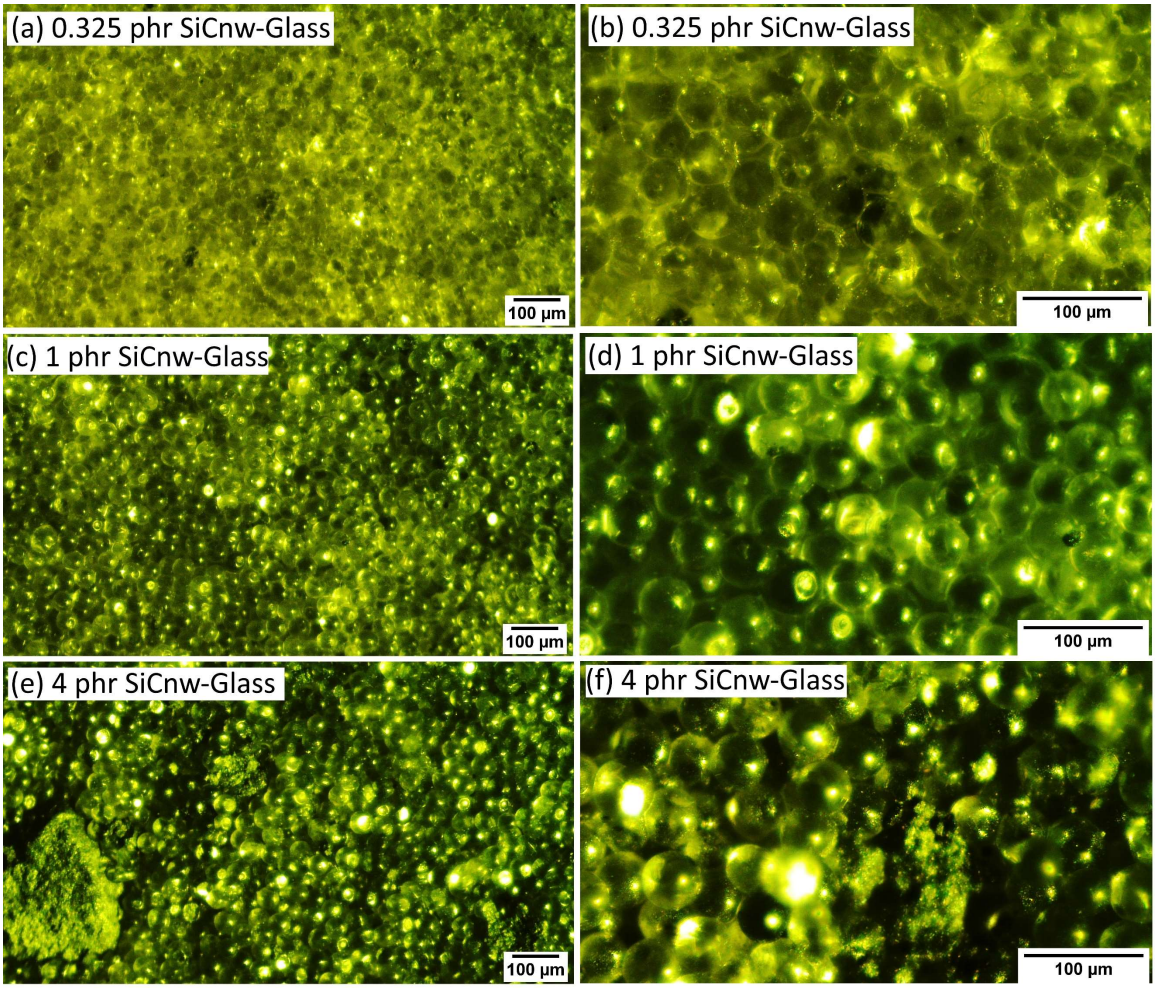

Figure 56 – Pentaview optical images of (a-b) 0.325 phr, (c-d) 1 phr, (e-f) 4 phr SiC nanowires/ glass composites

Figure 57 shows the SEM images of the same samples as in Figure 56. In Figure 57a, a large agglomerate of SiC nanowires is visible within a composite containing 0.325 phr composition. At 1 phr, the SiC nanowires are not easily spotted, and at 4 phr the nanowires have formed small agglomerates. The higher concentration of SiC_{nw} at 4 phr

may have lead to visible agglomerates. Additionally, the 4 phr appears partially sintered which is evidenced by the glass particles that are not perfectly spherical.

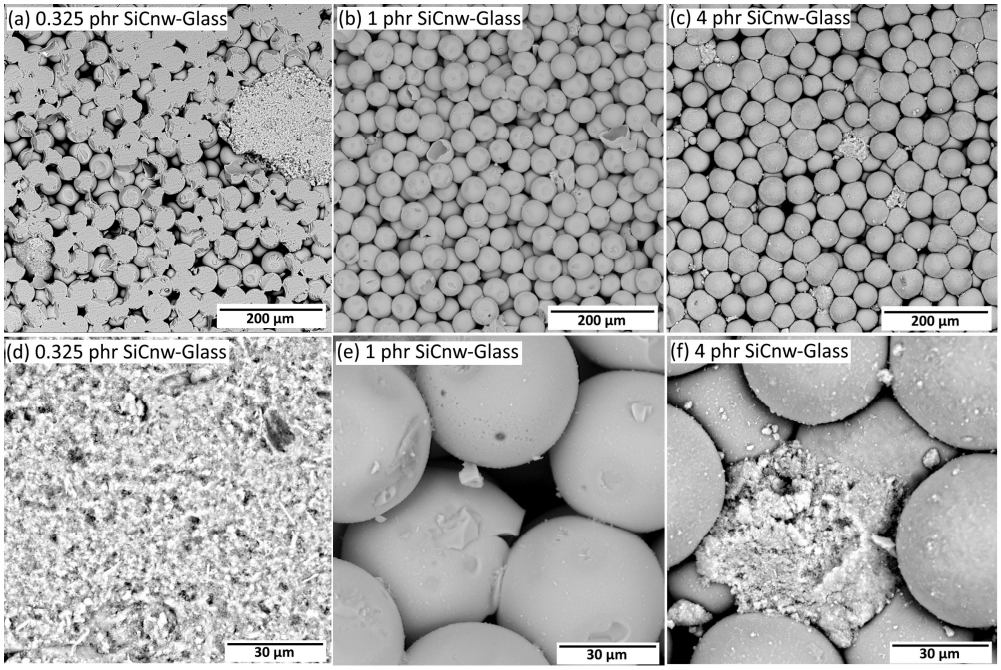

Figure 57 – SEM images of (a,d) 0.325 phr, (b,e) 1 phr, and (c,f) 4 phr SiC nanowire/glass composites

EDX of the samples was performed to verify the location of the SiC within the matrix. Figure 58 shows the EDX results and the location at which it was measured on the SEM images. This was performed for all the samples for which SEM analysis was conducted, but only 10 phr of the SiC_w and 4 phr of the SiC_{nw} are shown here. Red plus signs show the locations of the measurements. Figure 58 a and c were measured on the glass portion, while b and d were placed on SiC. The presence of carbon within the SiC showed in the EDX allows for identification of the location of the SiC within the glass

matrix. When measuring the nanowires, the glass also was observed using EDX. The glass signature shows some elements (Br, Na, and Sn) that may be contaminates. The bromine may actually be aluminium as that is a known ambiguity in EDX.

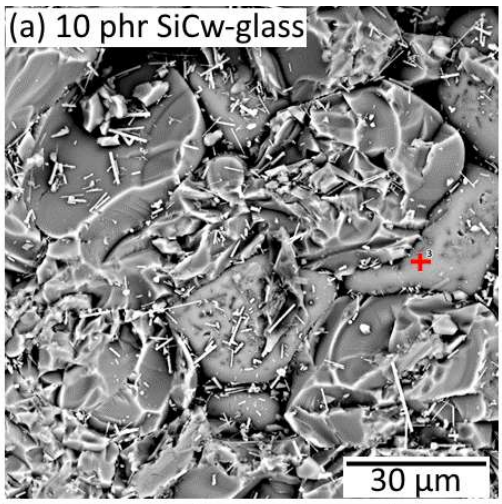

Element Symbol	Atomic Conc.	Weight Conc.	Oxide Symbol	Stoich. wt Conc.
O	77.81	65.12		
Si	20.02	29.42	Si	84.33
Br	0.76	3.17	Br	9.08
Na	1.28	1.54	Na	4.42
Sn	0.12	0.76	Sn	2.17

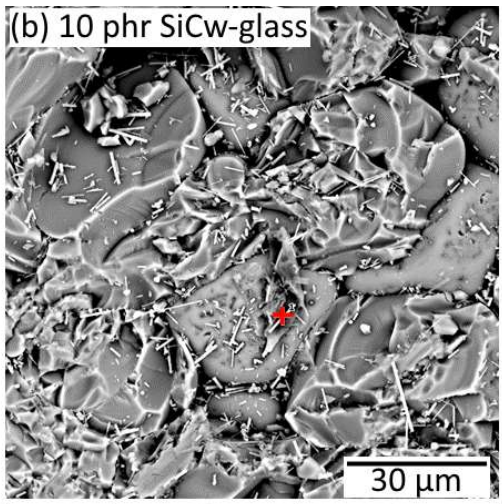

Element Symbol	Atomic Conc.	Weight Conc.	Oxide Symbol	Stoich. wt Conc.
Si	20.61	32.73	Si	45.03
O	30.18	27.30		
C	36.75	24.96	C	34.33

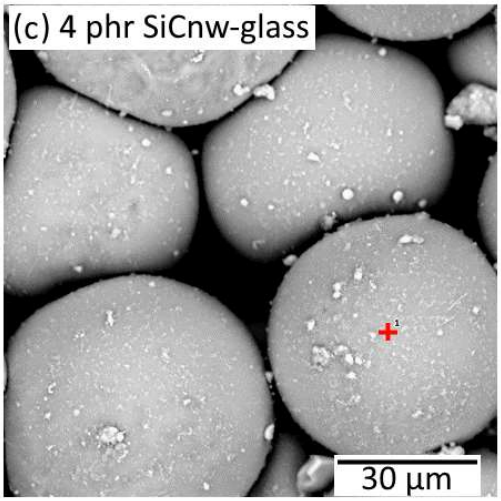

Element Symbol	Atomic Conc.	Weight Conc.	Oxide Symbol	Stoich. wt Conc.
O	72.36	57.91		
Si	24.97	35.08	Si	83.33
Br	1.10	4.39	Br	10.43
Na	1.40	1.61	Na	3.82
Sn	0.17	1.02	Sn	2.41

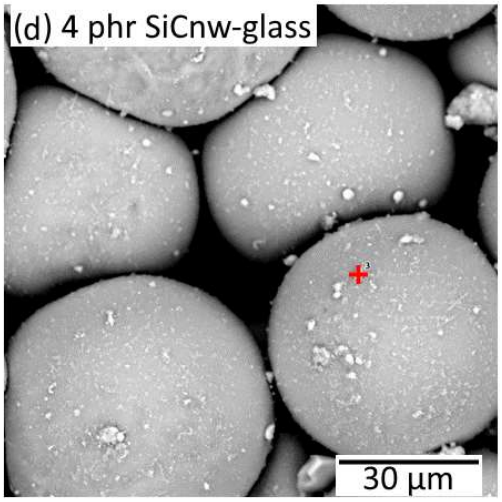

Element Symbol	Atomic Conc.	Weight Conc.	Oxide Symbol	Stoich. wt Conc.
O	68.07	63.08		
Si	13.03	21.19	Si	57.39
C	14.20	9.88	C	26.75
N	3.19	2.58	N	7.00
Br	0.38	1.75	Br	4.74
Na	1.14	1.52	Na	4.12

Figure 58 – EDX of SiC_w and SiC_{nw} composites. Red + signs mark the location measured

7.2 SPS In-situ Collection of Data

Figure 59 and Figure 60 show the data collected during the fabrication of the SiC whisker/glass and SiC nanowire/glass composites using spark plasma sintering (section 2.3.2), respectively. There was only one sample (7.5 phr S1) that had an abnormal voltage and current fluctuation during the SiC_w/glass fabrication. 0.05 phr S2 also had abnormal fluctuation during the SiC nanowire/glass fabrication. This may have been due to the thermocouple shifting during the temperature increase or non-perfect PID settings. Overall, the runs were very consistent with current, voltage, and temperature.

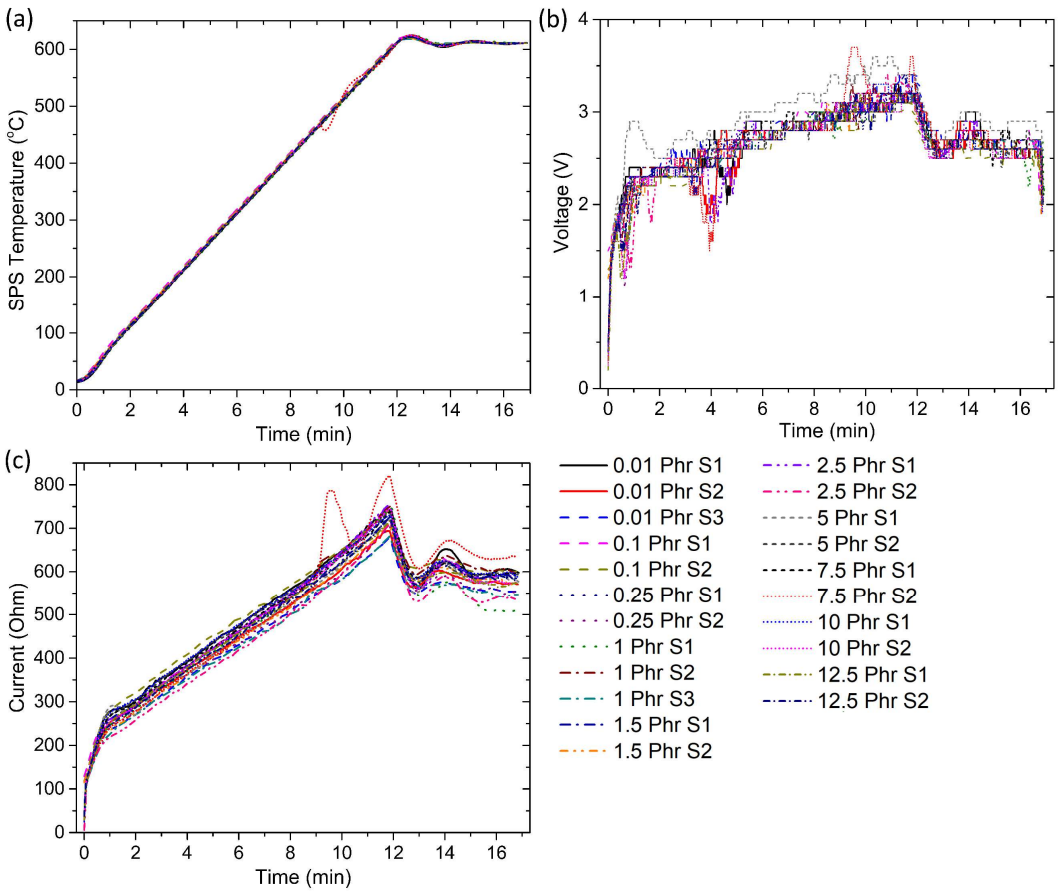

Figure 59 – SPS run data for SiC_w-glass composites with (a) temperature, (b) voltage, and (c) current versus time

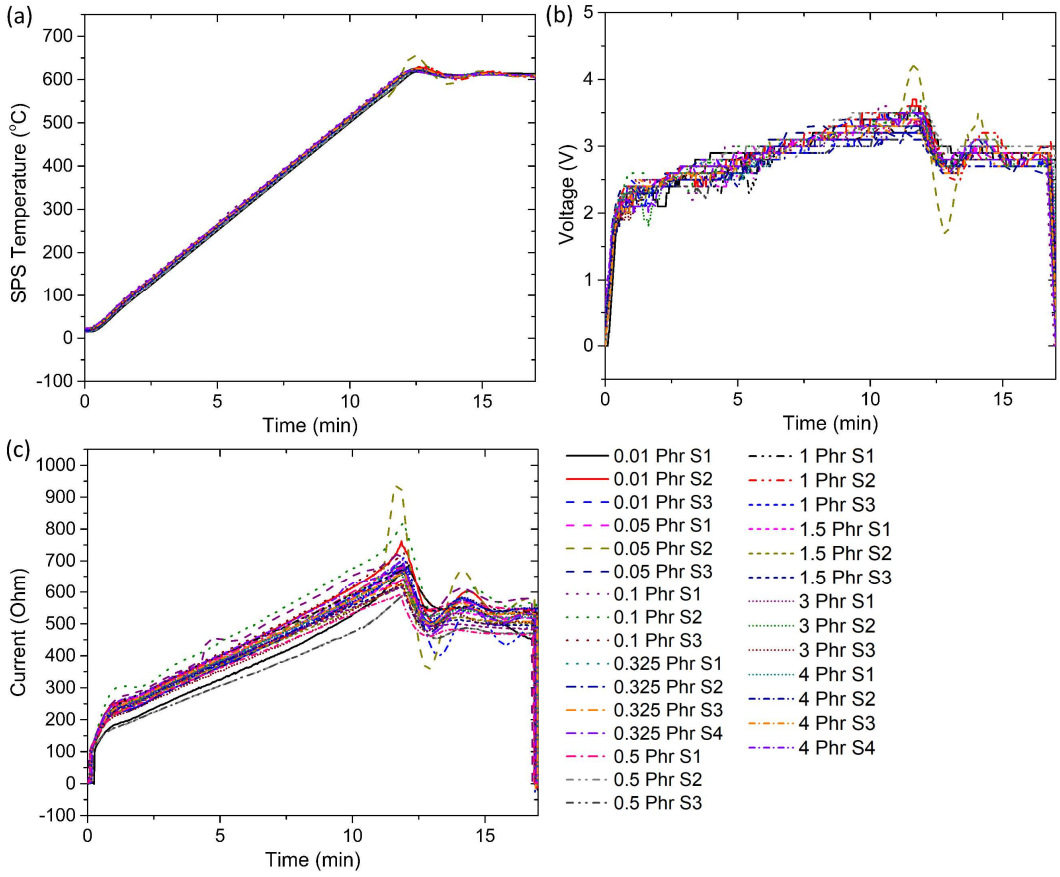

Figure 60 – SPS run data for SiC nanowire-glass composites with (a) temperature, (b) voltage, and (c) current versus time

7.3 Electrical Properties of SiC/Glass Composites at 10% Humidity

Figure 61 shows the impedance magnitude (|Z|) and phase angle (Θ) versus frequency for the SiC_w-glass composites. The orange squares in Figure 61 represent the impedance data of SiC_w pressed at 350 MPa, which were measured in situ. Percolation is seen at a concentration of 5 phr where there is the first deviation from -90° in the phase angle and where the impedance graph first decreases. At and after percolation, there is a

large variability that shows in the standard deviations in both |Z| and phase angle. The variability indicates that sometimes the network formed (lower |Z|) and other times it did not (higher |Z|).

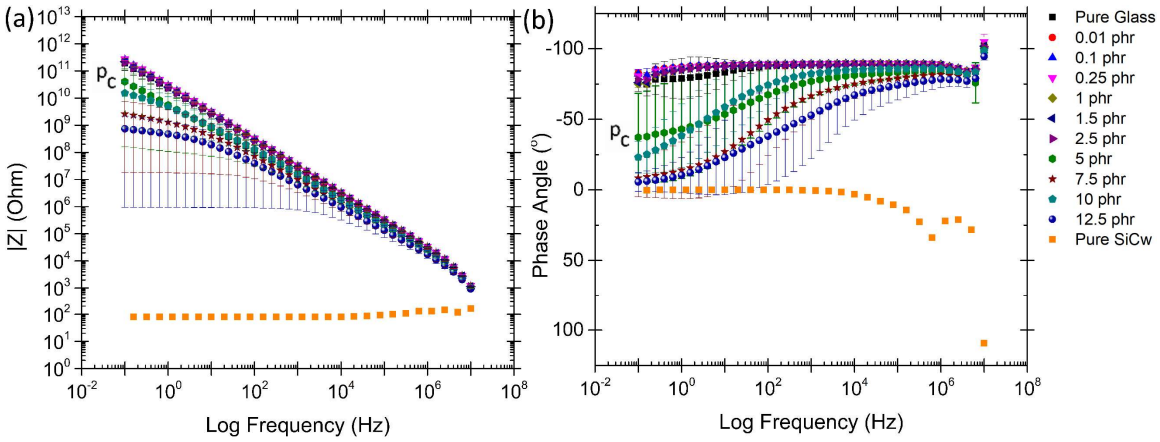

Figure 61 – (a) Impedance magnitude and (b) phase angle vs frequency for SiC_w/glass composites measured at 10% humidity, where p_c is percolation threshold

Figure 62 shows the impedance magnitude (|Z|) and phase angle (Θ) versus frequency for the SiC nanowire/glass composites at 10% relative humidity. The blue spheres represent the SiC nanowire powder measured at 350 MPa in-situ. There is less deviation with the SiC nanowire composites compared to the SiC_w composites indicating that the electrical measurements were more reproducible. The phase angle graph appears to have more wave in it than seen in the SiC_w/glass phase angle graph in Figure 61. For example, the 1 phr SiC_w/glass composites have a very visible variation in the error. From the impedance magnitude graphs in Figure 62a, percolation appears to start at 1 phr, where a slight decrease in impedance magnitude is observed.

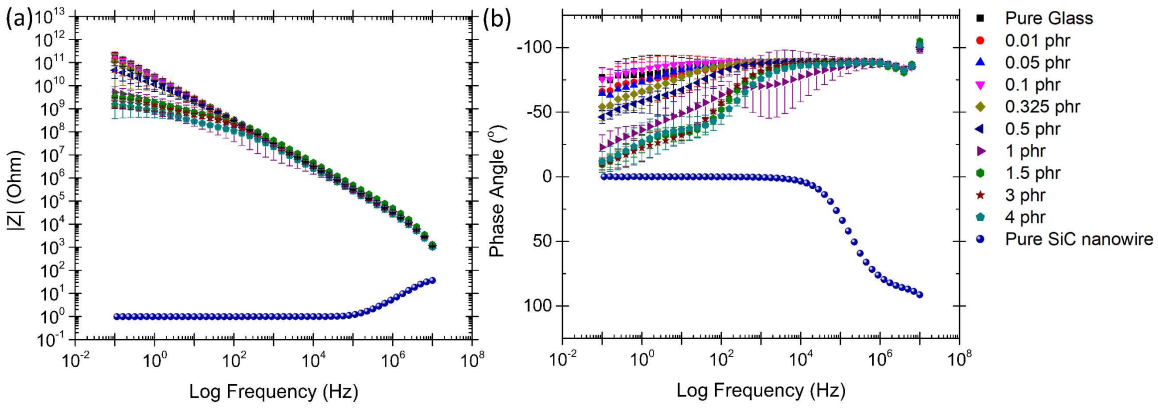

Figure 62 – (a) Impedance magnitude and (b) phase angle vs frequency for SiC nanowire/glass composites measured at 10% humidity

Figure 63 depicts the percolation graph of data collected from anisotropic SiC / glass composites and glass SPS samples. Additionally, SiC_w/glass composites that were hot pressed by Dr. T. Pruyn are included in Figure 63 to compare with the SPS SiC_w/glass samples [82]. The humidity that the hot-pressed samples were tested at is unknown. The hot-pressed samples were tested both in parallel and perpendicular to the hot-pressed direction. The SPS samples percolated at a lower concentration (5 phr) than the hot-pressed samples. An interesting trend is that both hot-pressed and SPS samples fabricated from the same ball-milled mixed powders experienced a dip at 10 phr. In order to explore this further, a 10 phr sample was cross-sectioned which will be shown in section 7.4.

In Figure 63, there are a couple of points representing the properties of the pure glass. The “past glass SPS” (black square) was tested at 10% humidity by Dr. T. Rudzik as a reference [94], while the “SPS glass-new” (red circle) is newly bought glass that was also tested at 10% humidity. There is a more than a magnitude of difference between the new

and old glass. This is important to do because the abnormal dip observed for the electrical properties of both hot-pressed and SPS sintered 10 phr SiC_w/glass composites. Due to this discrepancy, three samples of 10 phr SiC_w/glass were made using the new glass and speedmixing the powders (without ball milling). It had a dramatic effect of increasing two orders of magnitude in conductivity suggesting the original mix was different (contamination or a mislabeled composition possibly) from the new mix or it may have been incorrectly labeled. It may be coincidence, but the electrical conductivity of the new SPS sintered 10 phr SiC_w/glass composites (pink downward triangle) aligns with the rest of the compositions of the SPS sintered SiC_w/glass where the 10 phr would be expected rather than the dip that happened.

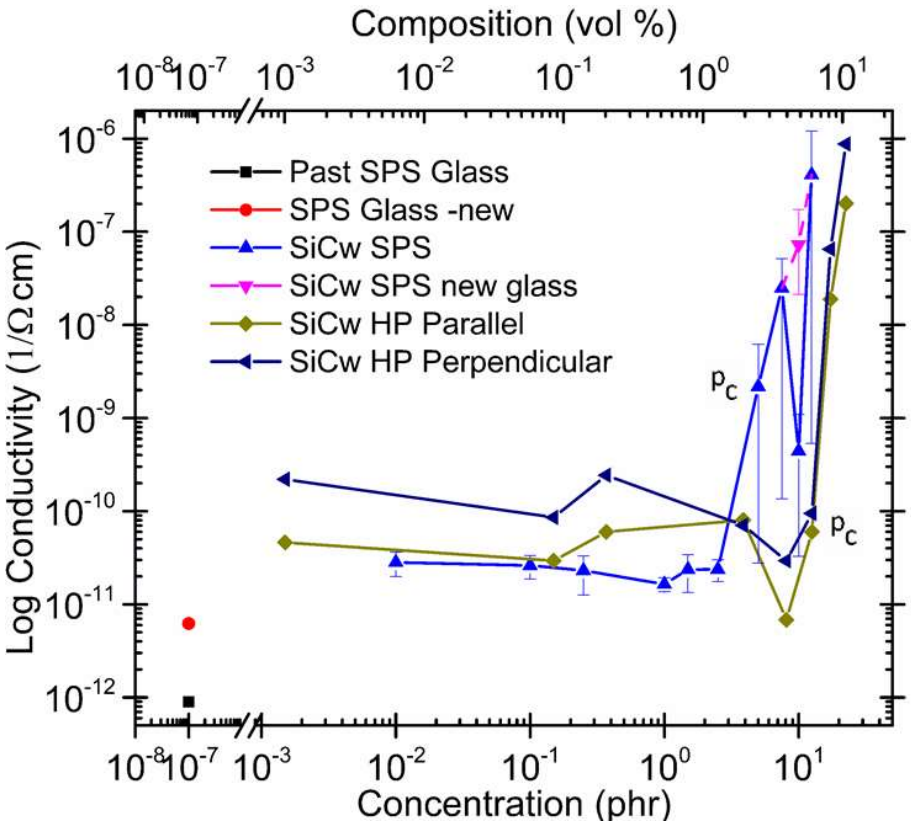

Figure 63 – Conductivity of SiC/glass composites as a function of SiC content comparing SPS and hot-pressed composites from Dr. Pruyn's work [82], where p_c is percolation threshold

Next, the conductivities of SiC nanowire and whisker composites are compared in Figure 64. The SiC nanowire glass composites did have a lower percolation (1 phr) than the SiC_w / glass composites (hot-pressed and SPS); however, the highest conductivity achieved for the SiC_{nw} composites is much lower than for the SiC_w composites, and the samples became too fragile to continue increasing the concentration since they broke on removal from the SPS.

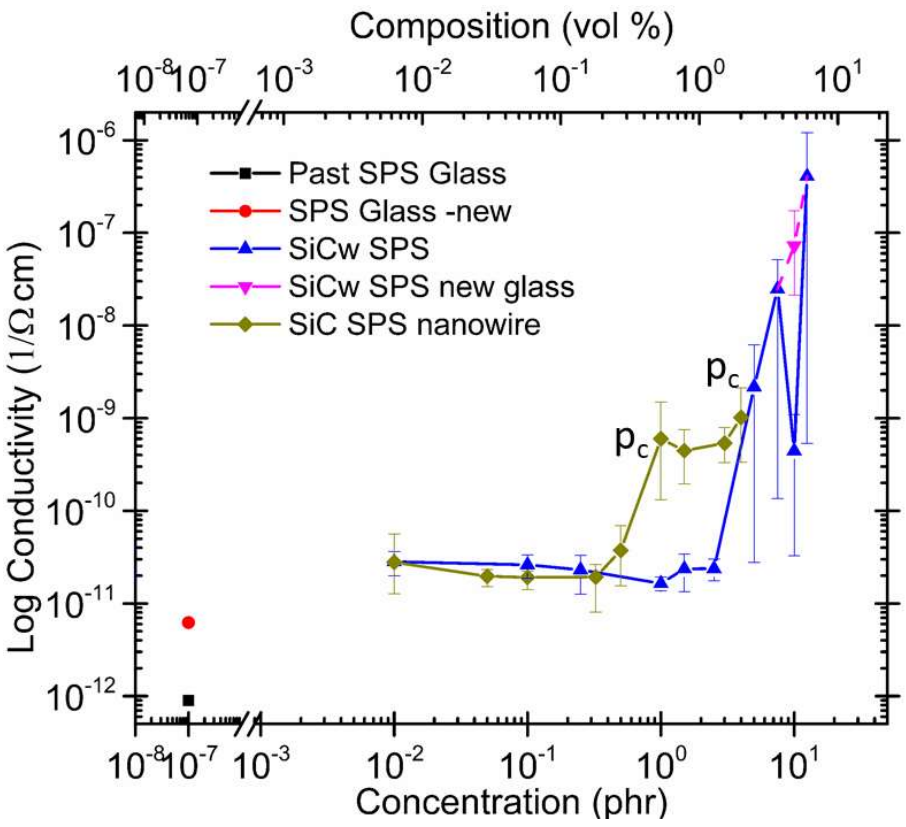

Figure 64 – Conductivity of SiC/Glass composites as a function of SiC content comparing SiC_w and SiC_{nw} as fillers, where p_c is percolation threshold

7.4 Electrical Properties – Heterogeneities at 10 phr SiC_w/Glass (Original Mix)

As mentioned, to explore the unexpected dip in conductivity a 1arger 10 phr sample was made using the original ball-milled mix [82] then cut using a diamond blade to study the change in microstructure and electrical properties across the sample. Figure 65 shows how the sample was cut, images of the slices, and the dimensions of the cut samples.

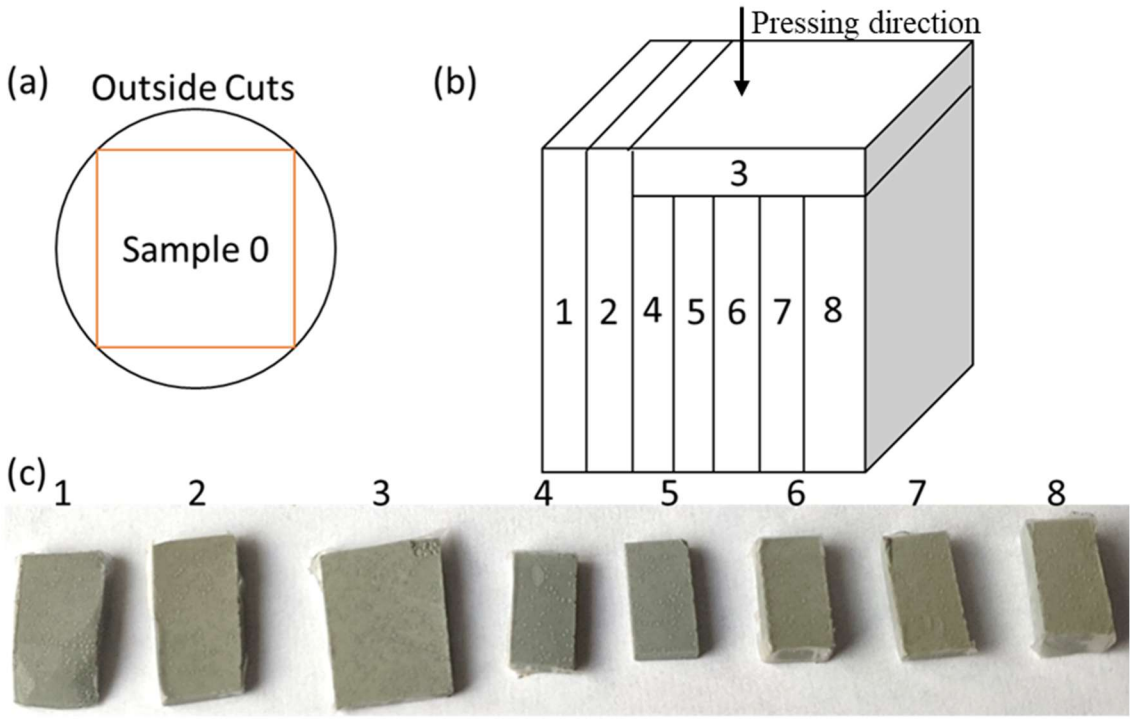

(d)

Sample	Height (mm)	Length (mm)	Width (mm)
Sample 0	8.11	16.25	14.45
Sample 1	7.67	2.38	13.89
Sample 2	7.4	2.14	14.49
Sample 3	2.14	10.78	14.2
Sample 4	5.54	10.36	2
Sample 5	5.48	10.34	2.08
Sample 6	5.5	10.51	2.65
Sample 7	5.47	10.61	2.13
Sample 8	5.49	10.8	3.66

Figure 65 – (a-b) Schematics of cuts made into a 10 phr SiC_w/borosilicate glass composite, (c) cut samples, and (d) size of samples

The microstructures of the samples were studied using a Pentaview optical microscope and are shown in Figure 66. It is observed that the individual cut samples are

inhomogeneous. Samples 6 and 7 showed much larger SiC_w agglomerates than all other sample slices.

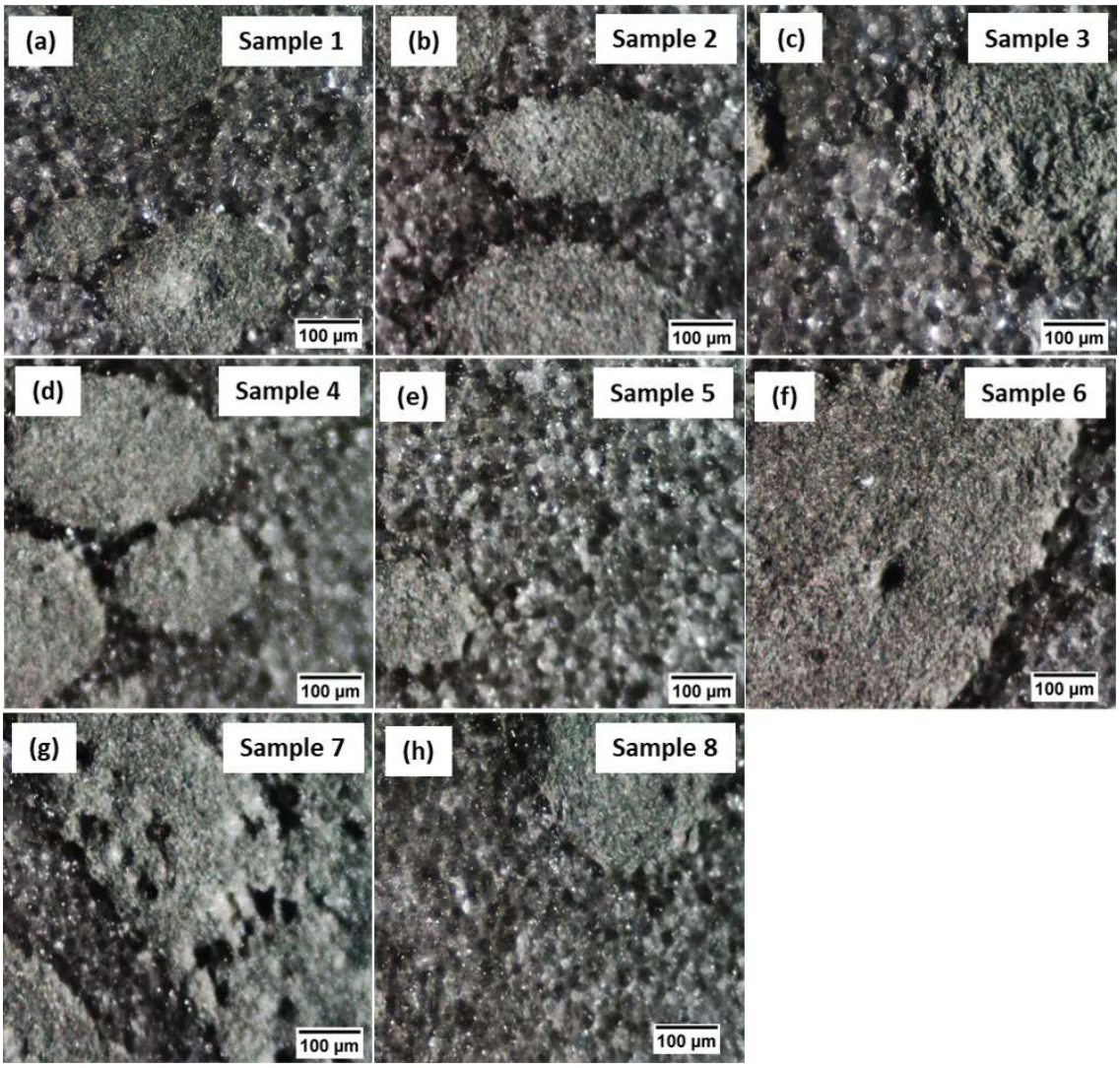

Figure 66 – Optical microstructures of the 10 phr SiC_w/glass composites slices cut using the method depicted in Figure 65

Figure 67 displays the impedance magnitude and phase angle versus frequency of the sample slices except for sample slice 5, which was left out for SEM analysis (shown in

Figure 55c and g). There is a large difference in electrical response across the sample. The impedance magnitude ranged from about 10^{11} to 10^{7} Ω, indicating that the original sample was inhomogeneous. It should be noted that the graphs in Figure 67 are not normalized by sample dimensions which may shift the values, but not the overall observed trends.

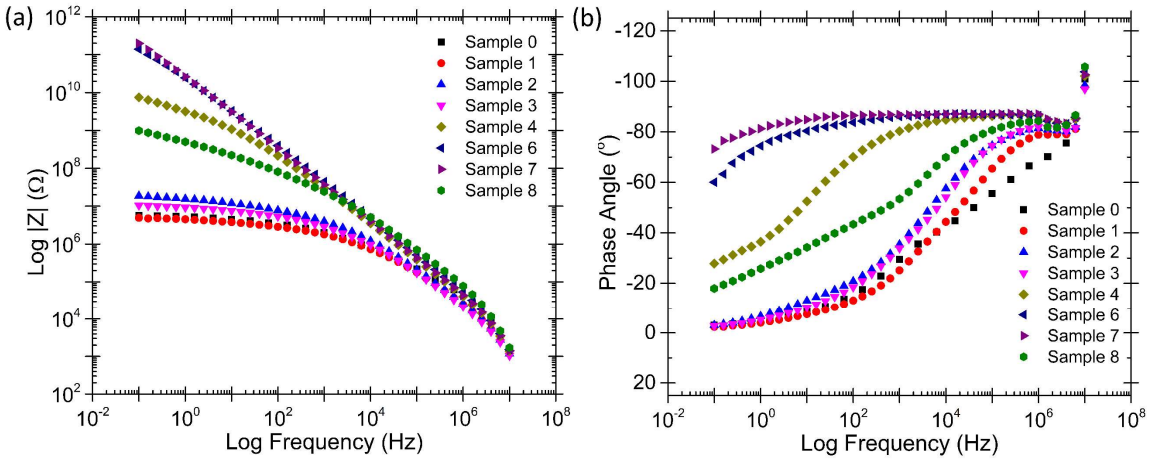

Figure 67 – (a) Impedance magnitude and (b) phase angle versus frequency for 10 phr sample cut into 8 sections. Not normalized by sample dimensions. Measurements were done on the largest face of each sample.

The conductivity values reported in Figure 68 take into account the size of the 10 phr sliced SiC_w/glass samples. It is observed again that the sample is not homogeneous. Overall, the sample labeled 0 (red square), which is before slicing, had the highest conductivity. Sample 3 was measured in the pressing direction and is represented by the blue square. The samples measured perpendicular to the press direction show that samples 6 and 7 have the lowest conductivity which coincides with the agglomerates that were seen in their microstructures (Figure 66 f and g). Since this was a thicker sample than made

before, that may cause some difference in its properties from the thinner samples mentioned previously in this chapter. However, it still should help with understanding the dip in the conductivity of the 10 phr SiC_w/glass (Figure 63). The dip is likely due to the presence of enough SiC_w within the matrix to form larger agglomerates but not enough to form a network of agglomerates (Figure 66).

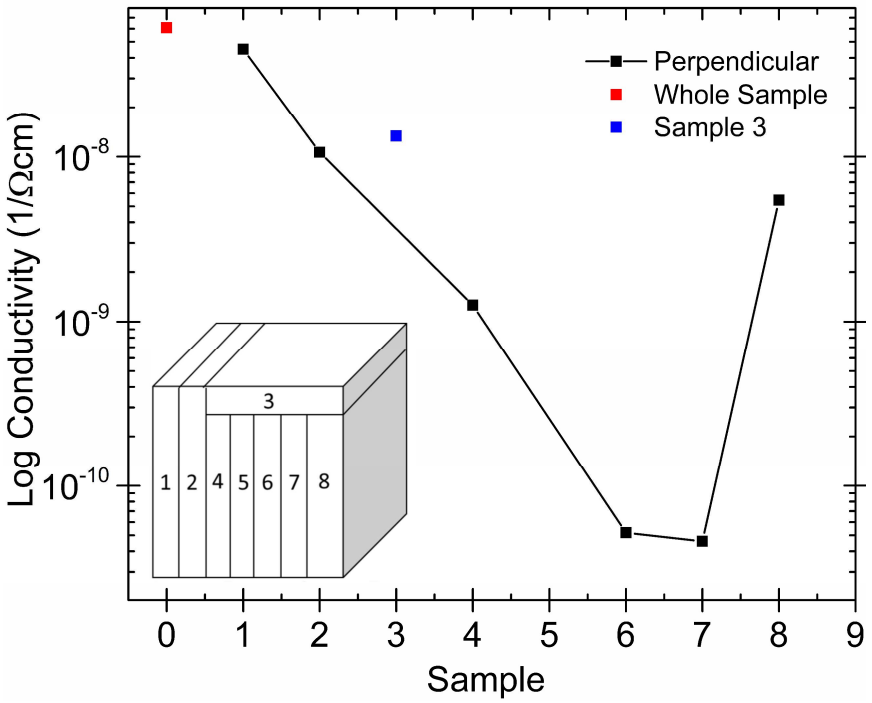

Figure 68 – Conductivity of each section of the 10 phr cut sample compared to whole sample. Inset shows location of each slice within the whole sample.

7.5 Summary

Two different sizes of anisotropic SiC (whisker and nanowire) were used to study the effect of filler size on the electrical percolation and microstructure of SiC/glass composites made using SPS. It was theorized that the smaller size of the SiC nanowires would allow it to segregate into the grain boundaries easier and create a lower percolation threshold. The basis for this theory is from works that did calculations and FEA simulations of 2D idealized segregated network microstructures with truncated octahedral and truncated tetrahedral shapes [59, 60]. Those works show that smaller filler particles of octahedral and tetrahedral shapes percolate at lower concentrations. This chapter focused on how the electrical properties (including percolation) and microstructure changed with anisotropic filler size rather than isotropic fillers. While it was true that the percolation threshold did decrease as predicted, the maximum conductivity value reached was not as high as for the SiC_w/glass composites value (Table 14). The SiC nanowire composites also became too fragile to handle with increasing the concentration after 4 phr. It may be that despite being the same materials, the SiC nanowire composites needed to be processed at a different temperature at higher concentration.

Table 14 – Summary of percolation thresholds and conductivities of whisker and nanowire SiC/glass composites

SiC Particle	Percolation, p_c	Conductivity
Whisker	5 phr	$4.09 \times 10^{-7} \pm 4.08 \times 10^{-7}$ $(\Omega\text{-cm})^{-1}$ at 12.5 phr
Nanowire	1 phr	$1.02 \times 10^{-9} \pm 1.11 \times 10^{-9}$ $(\Omega\text{-cm})^{-1}$ at 4 phr

The SPS made SiC_w/glass composites were also compared to hot-pressed composites made by a past student using the same powder mixes (Figure 63) [82]. In that case, the percolation threshold was lower while still reaching the same conductivity. Both hot-pressed and SPS composites had a dip at 10 phr. This may be due to either incorrect measurement of powders or agglomerates reaching a critical point of pulling SiC_w into agglomerates then raising conductivity again after having more SiC_w to reform the network. A sample at 10 phr was cut to study this phenomenon and did reveal an inhomogeneous microstructure with large agglomerates.

All the samples made in this chapter were tested at 10 % relative humidity because it was observed that the electrical measurement varied with increasing humidity. Chapter 8 will discuss the electrical properties trends and conduction mechanisms observed with increasing humidity for SiC_w/glass and PMMA composites.

8 EFFECT OF CHANGING HUMIDITY ON THE ELECTRICAL PROPERTIES

In this chapter, the effect of humidity during impedance testing will be reported for MWCNT/PMMA, SiC/PMMA and SiC/glass composites. The humidity range tested is from 10 – 80 % relative humidity using a humidity chamber to control the humidity during measurement. The impedance data will be converted to other dielectric functions (section 1.4.2) in order to explore the mechanism of conduction within the composites with changing humidity.

8.1 Impedance Spectroscopy of PMMA Composites Under Different Humidity

For PMMA composites, there appears to be little effect of humidity on the impedance response of the composites. This is seen for both MWCNT/PMMA (Figure 69) and SiC_w/PMMA (Figure 70) composites, where the symbols represent the samples measured at 60% humidity and the lines represent the samples measured at 10% humidity. The high humidity (60% and 50%) and low humidity (10%) overlap for both sets of PMMA composites, indicating no change with humidity.

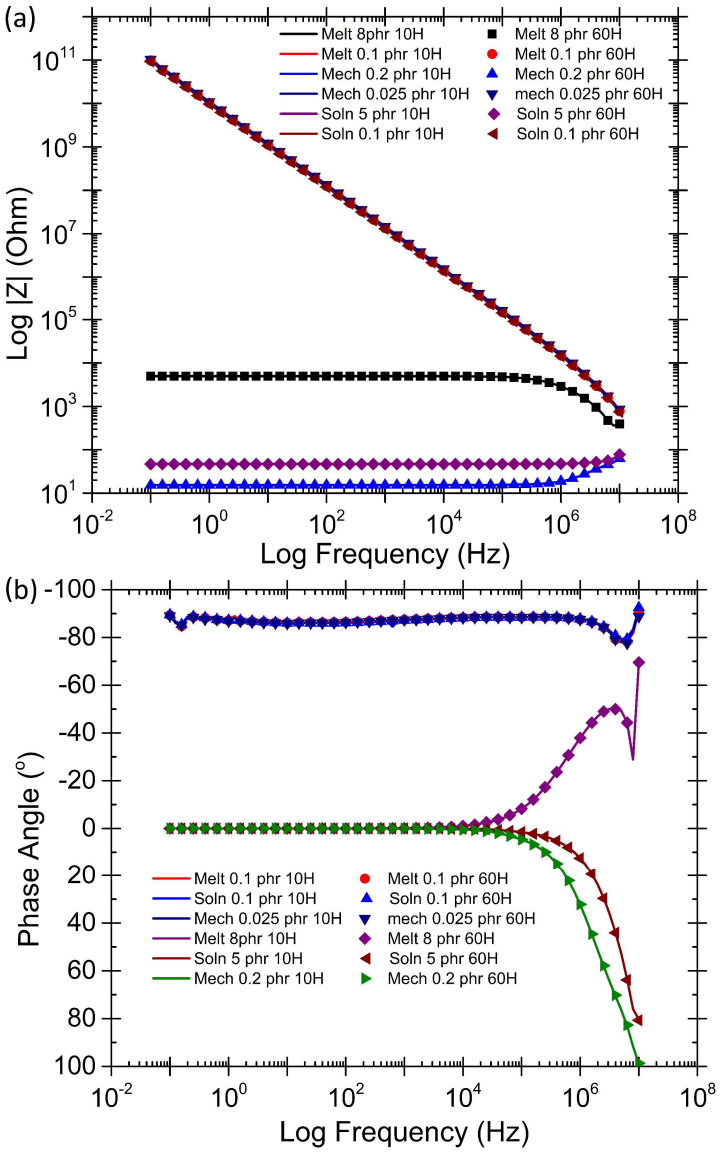

Figure 69 – (a) Impedance magnitude and (b) phase angle versus frequency for MWCNT/PMMA composites measured at 60% relative humidity (60H, symbols) and 10% relative humidity (10H, lines) where the 60% and 10% relative humidity data overlap at all concentrations

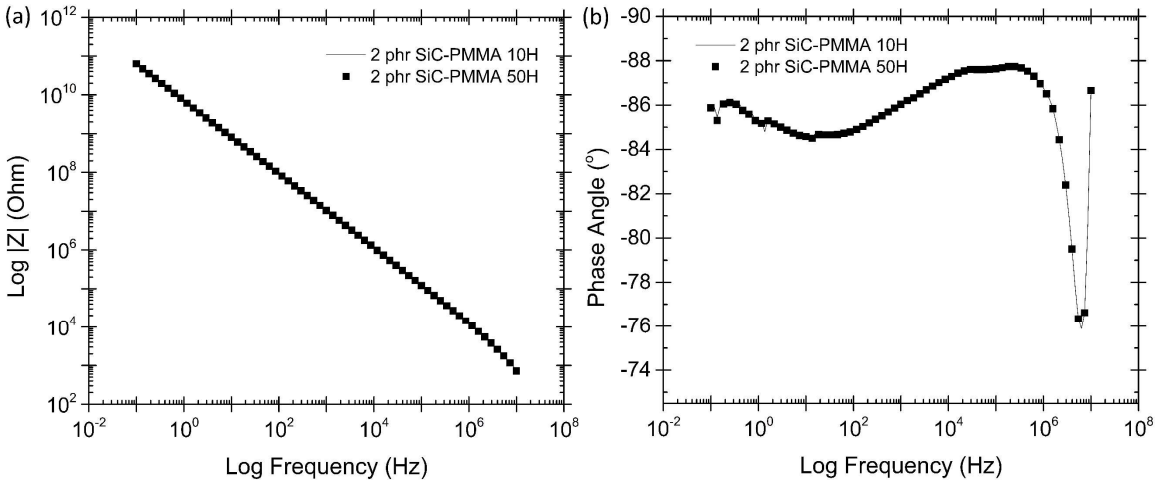

Figure 70 – (a) Impedance magnitude and (b) phase angle versus frequency for a 2 phr SiC_w/PMMA composite measured at 50% relative humidity (50H, symbol) and 10% relative humidity (10H, line) where the 50% and 10% relative humidity overlap

8.2 Impedance Spectroscopy of SiC_w/Glass Composites with Varying Humidity

The SiC_w/glass composites are a very different case than the PMMA composites. Borosilicate glass composites have been shown to be humidity sensitive using ITO/glass composites [80]. Figure 71 shows the change in impedance magnitude (|Z|) and phase angle (Θ) for (a-b) 0.25, (c-d) 2.5, and (e-f) 12.5 phr SiC_w/glass composites with humidity from 10-60% relative humidity. Each composite set shows at least a three magnitude decrease in impedance magnitude and an increase in inductive (decrease in capacitive) behavior with increasing humidity.

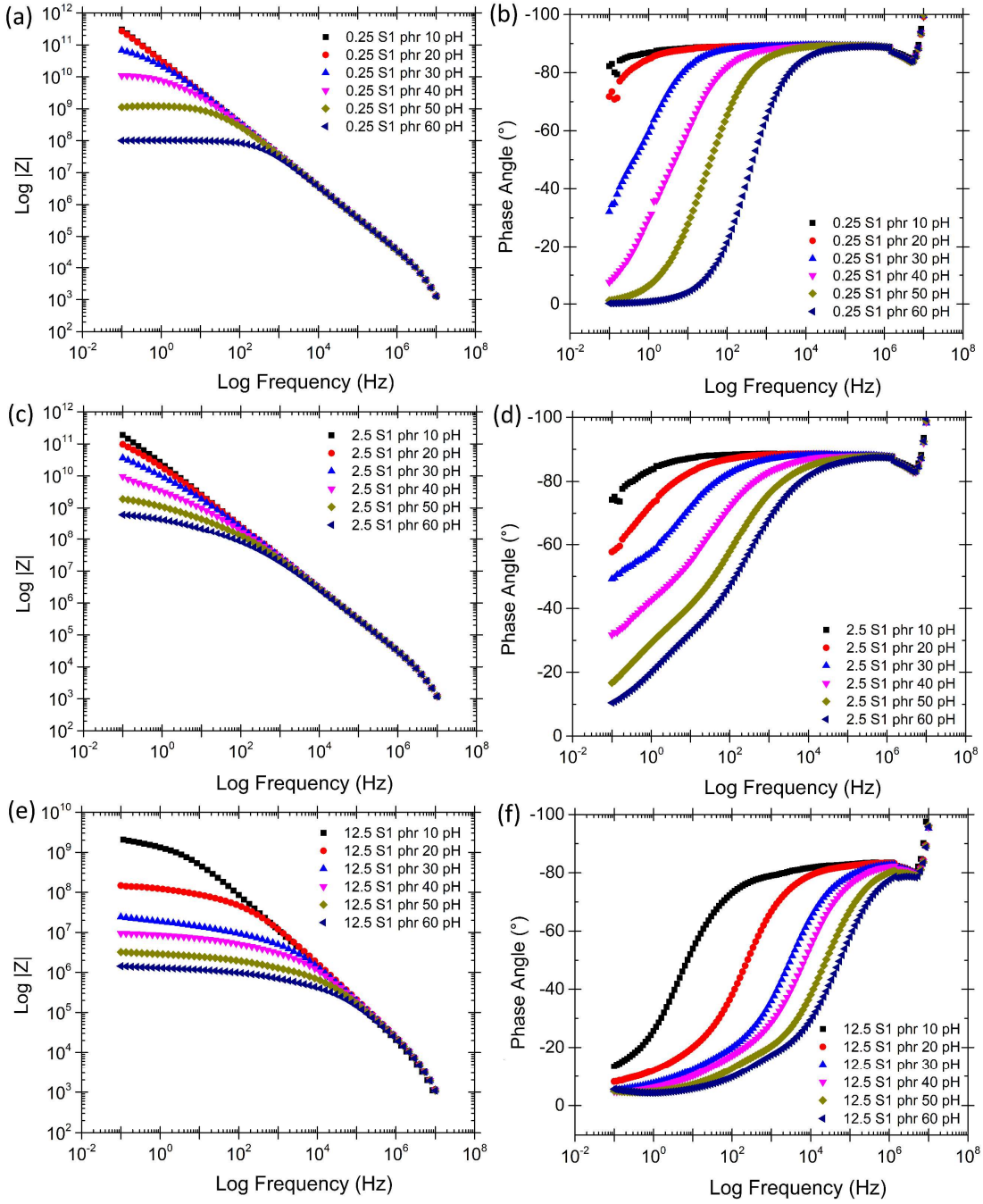

Figure 71 – Impedance magnitude and phase angle versus frequency for SiC_w/glass composite samples containing (a-b) 0.25, (c-d) 2.5, and (e-f) 12.5 phr measured from 10-60% humidity

Converting real impedance to conductivity, the graph in Figure 72 was created using bootstrapping (of 10000 random selections) to average at least 3 samples with the deviations shown using the error bars. The exceptions are the measurements at 88 % relative humidity, which could not be reached again once summer ended. From 0-2.5 phr, the conductivity decreases with increasing humidity until 40 or 50% humidity then increases. At 20% humidity, the 0.01 phr SiC_w/glass shows a spike in conductivity. For 7.5 and 12.5 phr, there is an initial sharp increase then a gradual decrease in conductivity with increasing humidity. This suggests that once the SiC_w have formed conductive paths, the continued addition of absorbed water disrupts these conductive pathways, whereas it increases conductivity for the lower concentrations.

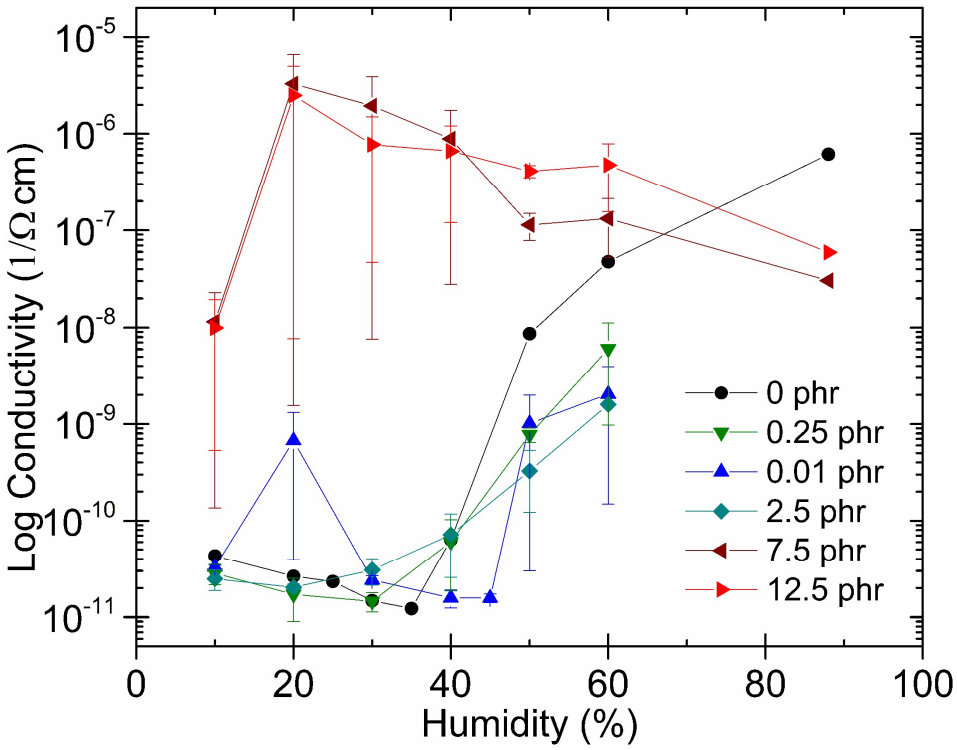

Figure 72 – Conductivity versus humidity of the SiC_w / glass composites

8.3 Conductivity Mechanism as a Function of Humidity Using Normalized M", Z", and Tanδ

To understand the mechanisms of conductance which takes place within the glass composites, imaginary impedance (Z"), imaginary modulus (M"), and tan delta (tand or tanδ) were normalized by dividing by their max amplitude. For this section, even though at least three samples were measured, only data for one sample of each composition (around the average conductivity of the samples displayed in Figure 72) are shown to ease understanding and represent the general trends. The presence or absence of a M" or Z" peaks indicates long range conductivity or localized conductivity [66]. When Z" and M"

peaks overlap at the same frequencies, this indicates long range conductivity [66]. In Figure 73a, the 0.01 phr composite has a full overlap of Z" and M" peaks from 40 to 80% humidity indicating long range conductivity through water molecules (green text). For the 0.01 phr composite, the conductivity is mainly due to the water absorbed into the composite. As the concentration increases, the conductivity is a mix of SiC and water creating the conductive paths. In Figure 73b, the 0.25 phr composite shows close but not fully overlapping Z" and M" peaks. The trend continues in Figure 73c where the Z" and M" peaks for the 2.5 phr composite have separated further. When the Z" and M" peaks are separate but present, this indicates a mix of long-range conductivity and localized relaxation [66]. At the highest concentrations shown of 7.5 and 10 phr (Figure 73 d and e), Z" peaks are present for all percent humidity and shift to higher frequencies with increasing humidity indicating that long range conductivity from the SiC was already present and then absorbed water from the atmosphere became a factor as humidity increased. Comparing the peaks of tanδ and M" (Figure 74) also reveals the mechanisms of conductivity. Tanδ peaks in the low frequencies indicate an onset of DC conductivity [66]. For the tanδ peaks shown in Figure 74e (12.5 phr high humidity), it is not clear exactly what is contributing to them other than being caused by the humidity.

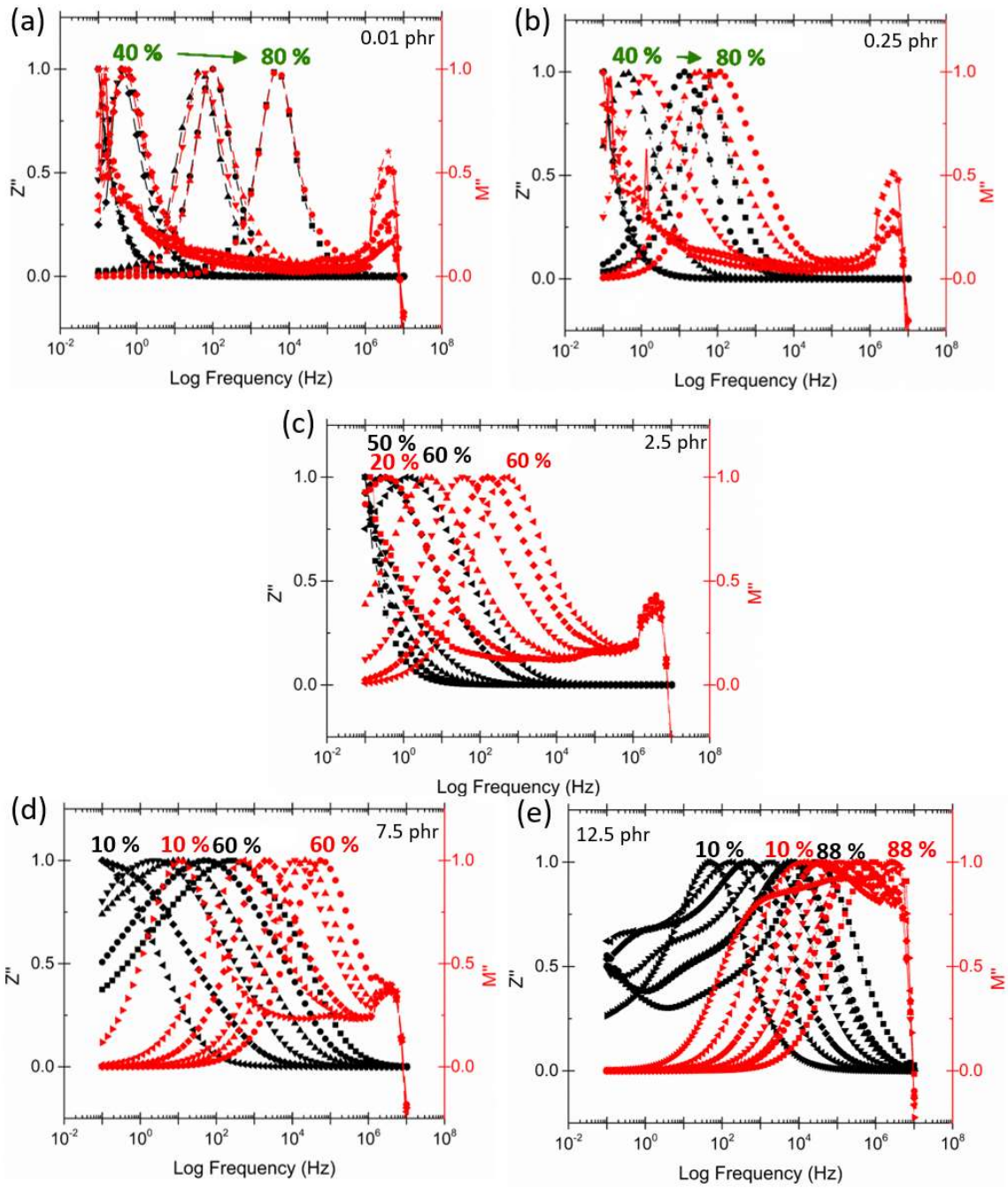

Figure 73 – Normalized Z" and M" versus frequency graphs of the SiC_w/Glass composites at (a) 0.01, (b) 0.25, (c) 2.5, (d) 7.5, and (e) 12.5 phr measured for 10-88% relative humidity (green text used where peaks overlap.)

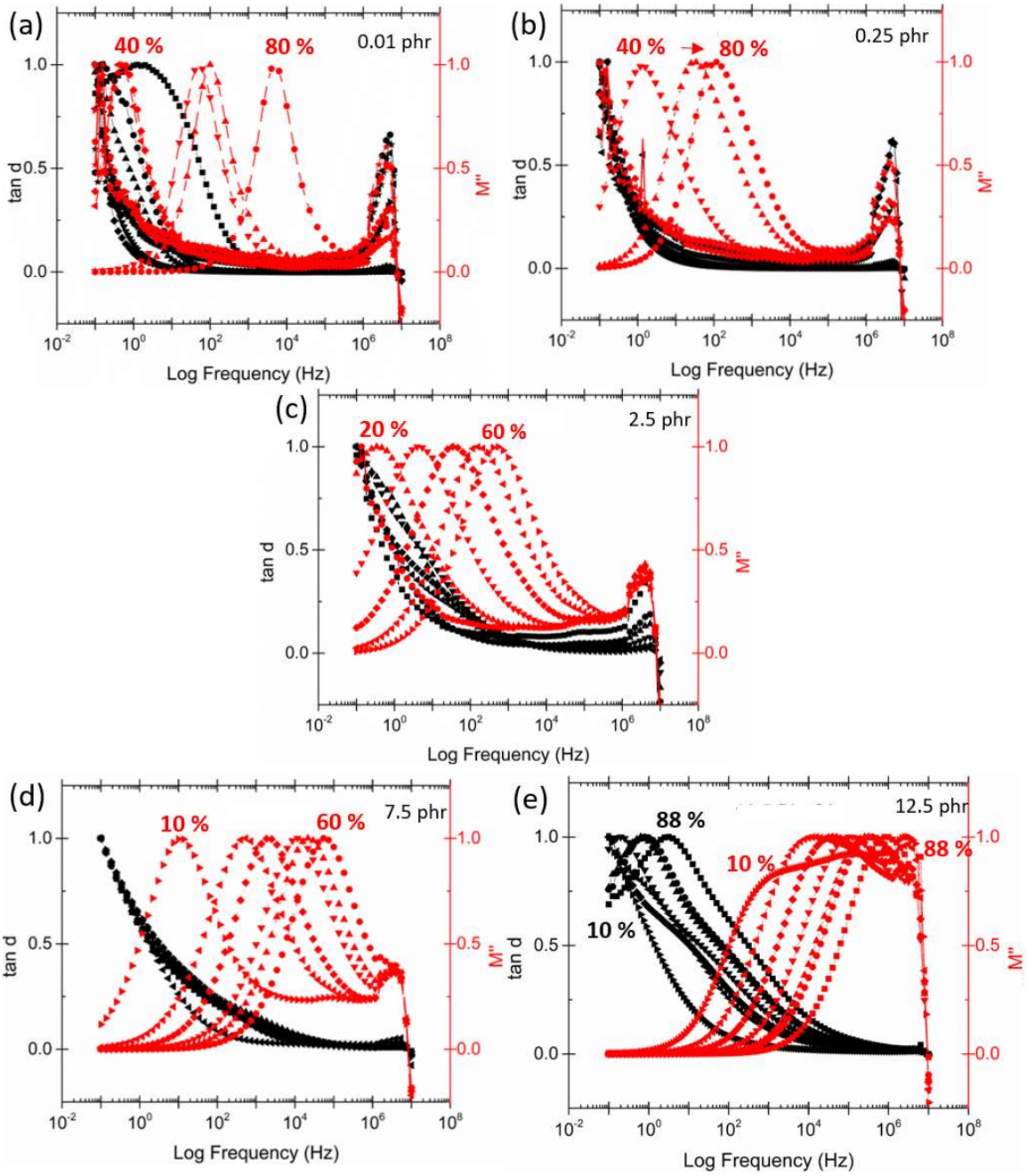

Figure 74 – Normalized tanδ and M" versus frequency graphs of the SiC_w/Glass composites at (a) 0.01, (b) 0.25, (c) 2.5, (d) 7.5, and (e) 12.5 phr measured for 10-88% relative humidity

The patterns of the peak locations (Figure 76) and peak height (Figure 77) are also important to study with the change in humidity. Figure 75, which displays representative spectra from different compositions and humidity, are labeled with Z" peak, M" peak 1, M" peak 2, tand peak 1, and tand peak 2 to help explain the naming convention shown in Figure 76 and Figure 77. From Figure 76, the change in the frequency location of the peaks is shown. At all concentrations, only the M" peak 1 (highest peak) and Z" peak show a significant shift in the frequency of the peak location with increasing humidity. The M" peak 1 and Z" peak also both increase in frequency with increasing composition. At the concentration of 12.5 phr, the tanδ peak 1 also showed a shift in the frequency as was seen in the appearance of tanδ peaks in Figure 74e. At lower concentrations, the tanδ peaks do not show much change in frequency.

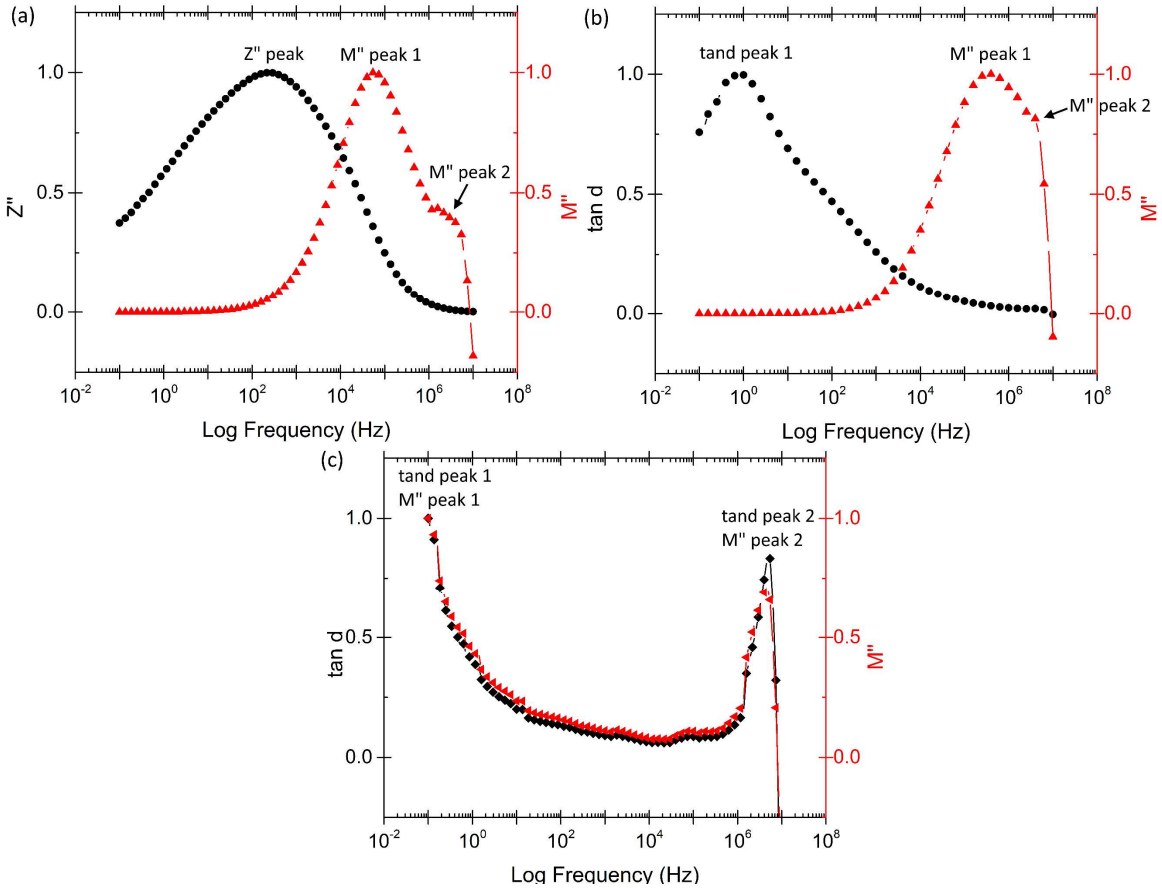

Figure 75 – (a) Representative imaginary impedance and modulus versus frequency and (b-c) imaginary tan d and modulus versus frequency to understand peak naming

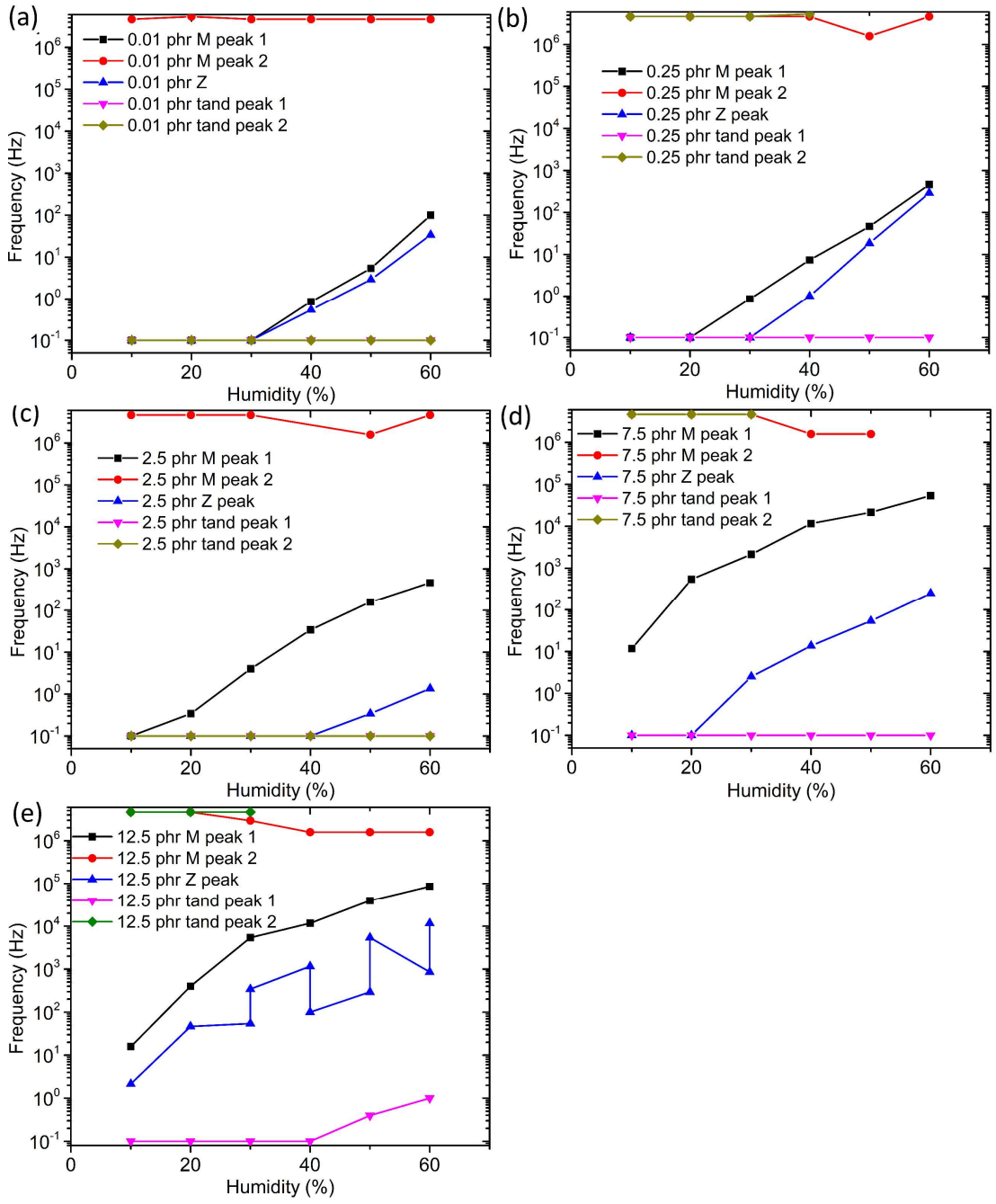

Figure 76 – Peak location frequency versus percent humidity for select SiC_w/Glass composites at (a) 0.01 phr, (b) 0.25 phr, (c) 2.5 phr, (d) 7.5 phr, and (e) 12.5 phr

Peak heights were obtained from M", Z", and tanδ graphs for each composition at increasing percent humidity. These results are summarized in Figure 77. For the highest peak of M" (peak 1), in all compositions there is a slight increase in peak height with increasing humidity (Figure 77a). A smaller peak in M" (peak 2) shows a slight increase peak height for 7.5 and 12.5 phr (Figure 77b). Conversely as shown in Figure 77c, 0, 0.01, and 0.25 phr composites increase in peak height for the highest tanδ peak (peak 1). Lastly (Figure 77e), the Z" peak decreases for 0-2.5 phr compositions with the increase in humidity.

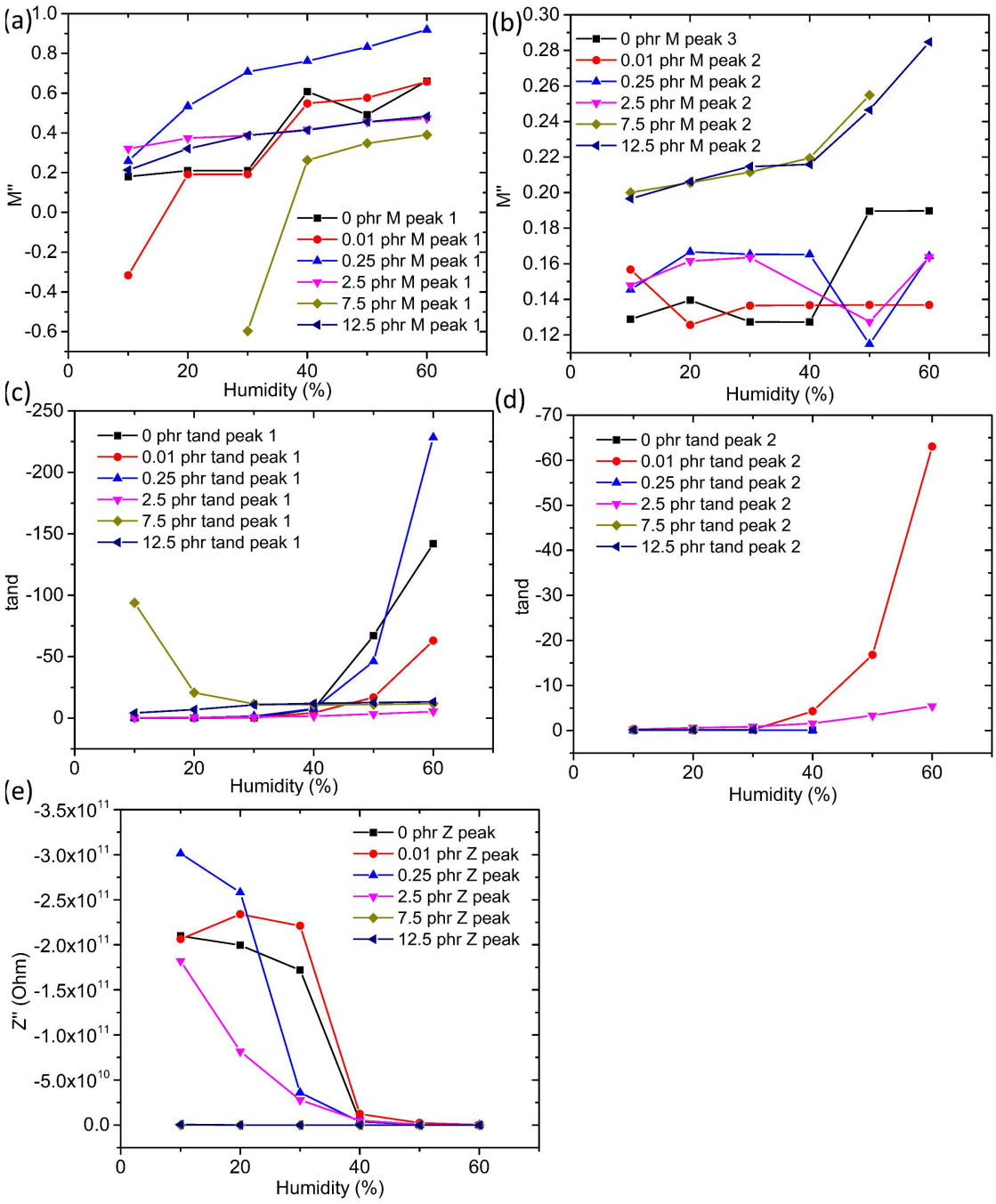

Figure 77 – Peak height versus percent humidity for select SiC_w/Glass composites at 0 phr, 0.01 phr, 0.25 phr, 2.5 phr, 7.5 phr, and 12.5 phr. (a) M" peak 1, (b) M" peak 2, (c) tanδ peak 1, (d) tanδ peak 2, and (e) Z" peak

8.4 Summary

MWCNT/PMMA, SiC_w/PMMA, and SiC_w/glass were all impedance tested at a range of humidities. Both composites with a PMMA matrix were not affected by increasing the humidity. Conversely, the glass composites were strongly affected by humidity. There was also a difference in how the composites react to humidity with different content of SiC. From 0-2.5 phr, the conductivity increases with increasing humidity. For 7.5 and 12.5 phr, there is an initial sharp increase then a gradual decrease in conductivity with increasing humidity. The mechanism of conductivity was analyzed by normalizing the imaginary impedance, imaginary modulus, and tanδ and plotting them together for comparison. As humidity increases the peaks shift towards higher frequencies. For most compositions, M" and Z" are separate which indicates that both localized relaxation and long-range conductivity are present.

Chapter 9 will apply equivalent circuit models to the impedance data collected in this chapter and Chapters 4-7 to fulfill the hypothesis of this thesis. The equivalent circuit models should show, through individual circuit element values, the effect of individual materials, processing, and humidity on the overall electrical properties.

9 UNDERSTANDING THE ELECTRICAL RESPONSE OF CONDUCTIVE FILLER / INSULATING MATRIX COMPOSITES BY MODELING IMPEDANCE DATA

In order to properly analyze impedance data for a sample, fitting the data to an equivalent circuit is essential. Seeing the change in circuit values with concentration, humidity, or any other condition allows for a better understanding of the contribution of each feature present within the material to the overall properties. This chapter will take the impedance data from Chapters 4-8 and fit them to equivalent circuits.

9.1 Initial Models for Compressed Filler Powders and Sintered PMMA and Glass

First, the impedance data for individual materials are fit to equivalent circuit models for later comparison to composite circuits. Each of the models may contain resistors (R), constant phase elements (CPE), and inductors (L). As mentioned in Section 1.4.3, CPEs are used instead of capacitors since they account for the imperfects of real capacitance.

9.1.1 MWCNT Powder Equivalent Circuit Fitting

The base materials need to be fit before fitting the composite materials. For the compressed MWCNT powder presented in Figure 37 showed that increasing the loading decreased the impedance. The data obtained for 300 MPa compression produced the most stable measurement, so it was chosen for equivalent circuit fitting. The circuit developed for MWCNT powder is shown in Figure 78 along with the values.

The MWCNT equivalent circuit fitting is very close to one of the equivalent circuits developed by Dr. Rachel Muhlbauer in past work with in plane impedance measurements of MWCNT deposited on paper [95]. The circuit in this dissertation has one more inductor than Muhlbauer's, most likely due to the absence of the paper substrate. This indicates that measuring the MWCNT as a pellet rather than on a paper substrate forms more interconnects between the MWCNT.

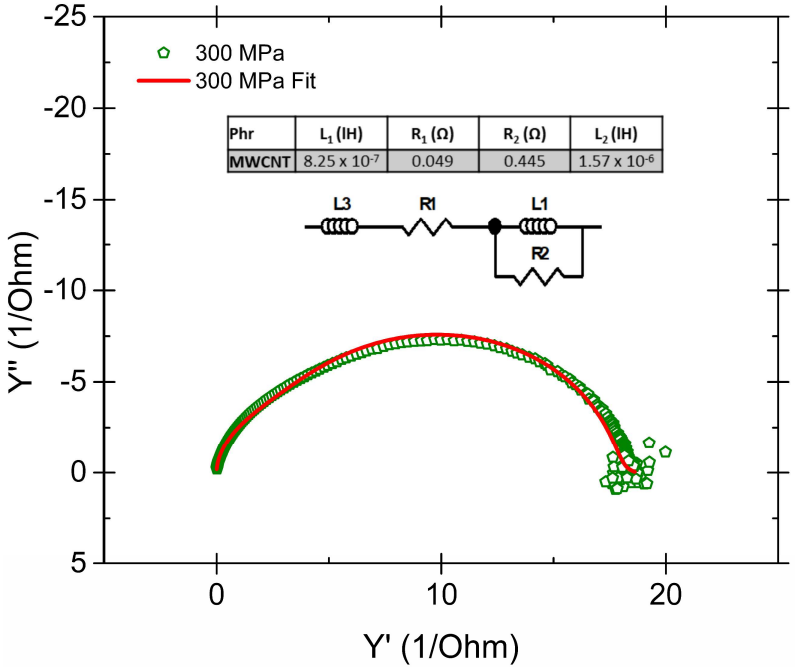

Figure 78 – Experimental data and fits complex admittance of MWCNT compressed at 300 MPa and measured in-situ

9.1.2 SiC Powder Equivalent Circuit Fittings

Most of the SiC powders were able to fit to the same circuit, as seen in Figure 79 with complex admittance data. The powders were all measured in-situ under 350 MPa

(Figure 48 and Figure 49). The micron-SiC R circuit values were lower and the CPE circuit values higher than the corresponding values for nano-SiC and whisker SiC. Conversely, the SiC_w R circuit values were higher and CPE circuit values were lower than the nano-SiC and micon-SiC corresponding values. The SiC nanowires were more conductive than the other three powders and had one less CPE in its circuit. A possible reason for this is the difference in the purity of the powders. The circuit for the SiC nanowire is the same circuit used to fit the MWCNT data. The SiC nanowire fit has higher resistance values, one larger inductance value, and one inductance value about the same as the MWCNT values. Overall, they are both very conductive which leads to the same circuit being used.

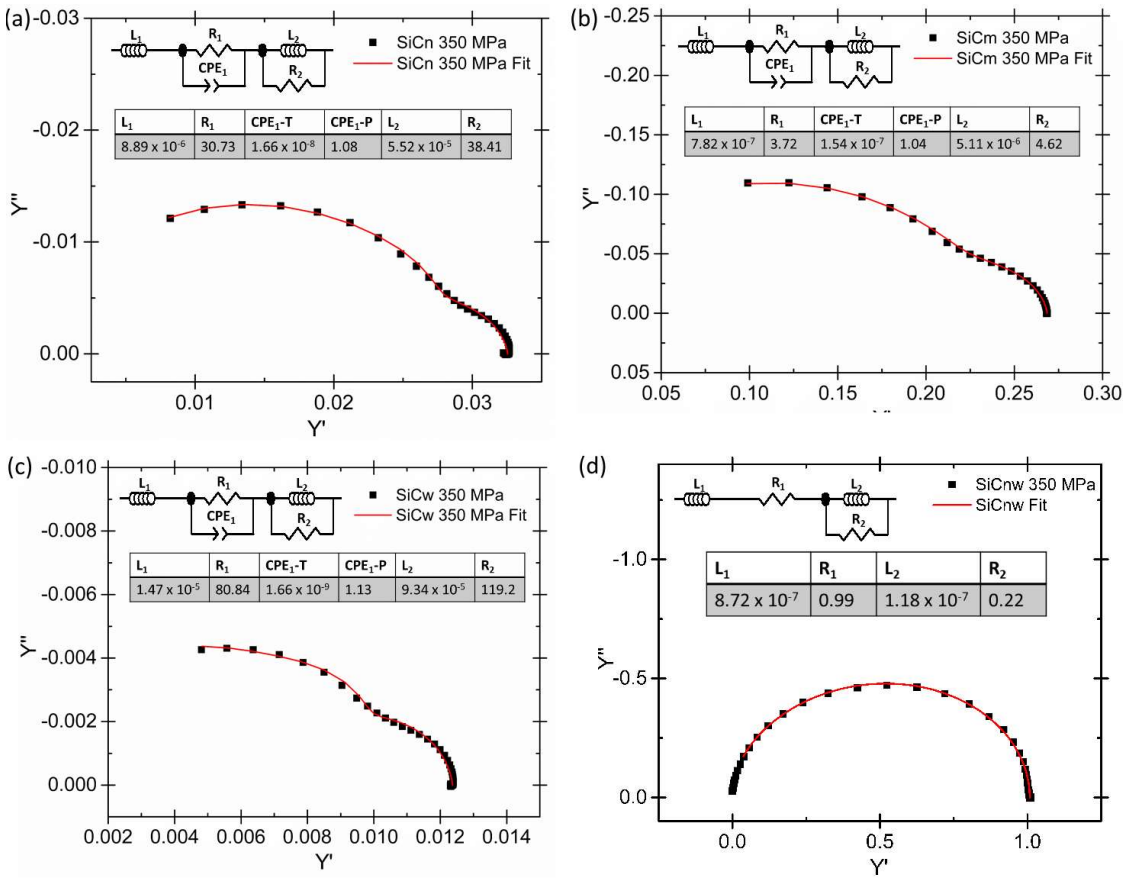

Figure 79 – Complex admittance and fits for (a) nano-sized, (b) micron-sized, (c) whisker, and (d) nanowire SiC powders compressed at 350 MPa and measured in-situ

9.1.3 PMMA Pellet Equivalent Circuit Fittings

PMMA was compression molded the same way that the polymer composites were at 170 °C and 20 kN. Figure 80 is a complex modulus graph with a single sample's data (from data in Figure 38 and Figure 39), fit, and equivalent circuit. The PMMA circuit has no inductors, three resistors, and 3 CPEs. Overall, the circuit has very high resistance and low capacitance.

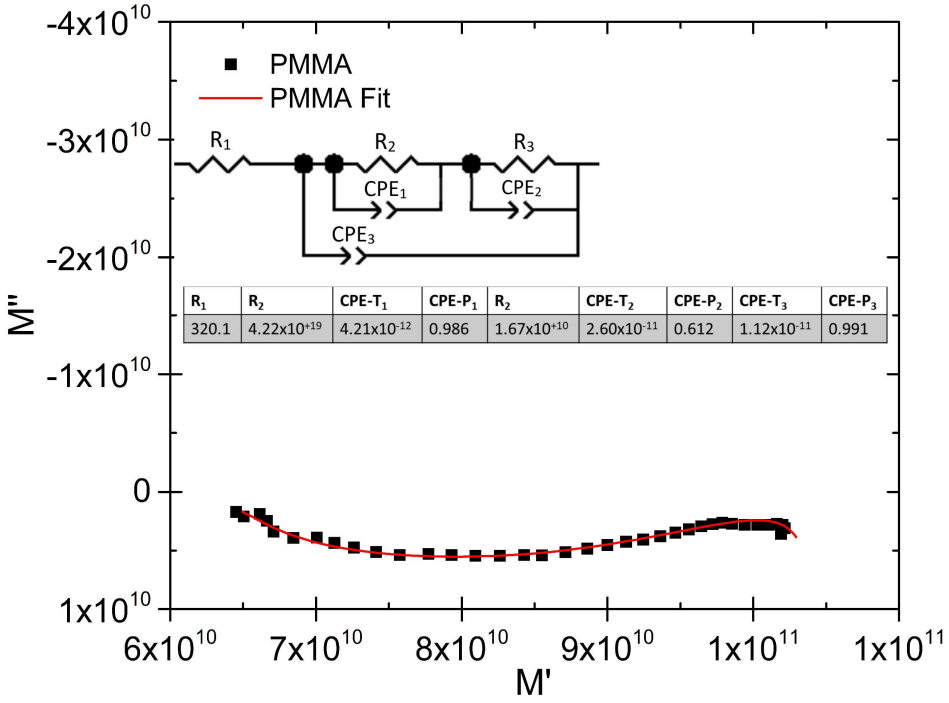

R_1	R_2	CPE-T_1	CPE-P_1	R_2	CPE-T_2	CPE-P_2	CPE-T_3	CPE-P_3
320.1	$4.22\times10^{+19}$	4.21×10^{-12}	0.986	$1.67\times10^{+10}$	2.60×10^{-11}	0.612	1.12×10^{-11}	0.991

Figure 80 – Complex modulus and fit of PMMA hot-pressed sample with fit data

9.1.4 Borosilicate Glass Equivalent Circuit Fittings

The borosilicate glass samples were fabricated using an SPS at 610°C heated at a rate of 50°C per minute, the same as the composite SPS samples. The equivalent circuit fit of one glass sample (10% humidity) is shown in Figure 81. This circuit is similar the PMMA equivalent circuit, which has one more resistor in series. The glass fit has smaller CPE values and higher resistance values than PMMA fit values indicating that overall, PMMA is more conductive than the glass which correlates with the conductivities measured previously (Figure 39 and Figure 63).

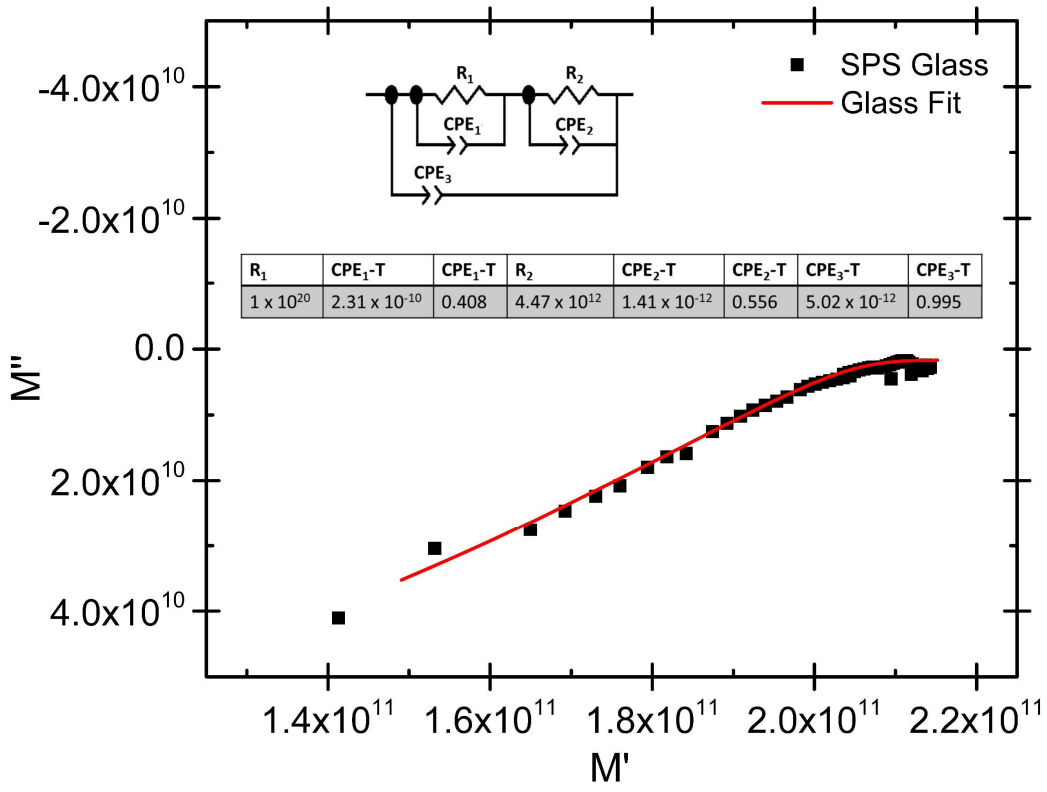

Figure 81 – Complex modulus and fits of SPS sintered glass

9.2 Change in Equivalent Circuit Models with Increasing Concentration of CNT within Composites made using Three Mixing Methods

The equivalent circuits used for fitting the electrical data vary with the formation of CNT paths through the differently made composites. Figure 82 shows the typical formation of paths for the composites made using the three different mixing methods. In the mechanical case (Figure 82a), the conducting particles (black lines) are segregated to the edges of the insulating particles (blue background). This creates a grain-like structure that reduces the space the conducting particles may be located in and therefore requires

fewer particles to form a conducting path. The solution mixed composites have the largest variety of microstructures but in this case the MWCNTs are agglomerated. Figure 82b shows that first the agglomerates form then the conducting path forms through the touching of agglomerates. Last, the melt mixed composites (Figure 82c) distributes the conducting particles more evenly through the insulating matrix. Since the particles are evenly distributed over the whole volume of the composite, it takes many more conducting particles to form the paths. For the insulating samples, the intrinsic CNT contribution is simplified to an inductor and resistor in series. The edge of the network and PMMA matrix is represented by R_{PMMA} and CPE_{PMMA}, while R_1/CPE_1 and R_2/CPE_2 parallel RC circuits in series represent the main conducting path. In Figure 82c, the conducting paths are colored red with dead ends marked in lime green. The flow of current through the composites is reliant on the connections of the paths. If there is only one connection that the current may pass through with others serving as dead ends, that point will limit the conduction of the composite overall [96]. This causes the circuits for conducting samples to vary more than for insulating samples.

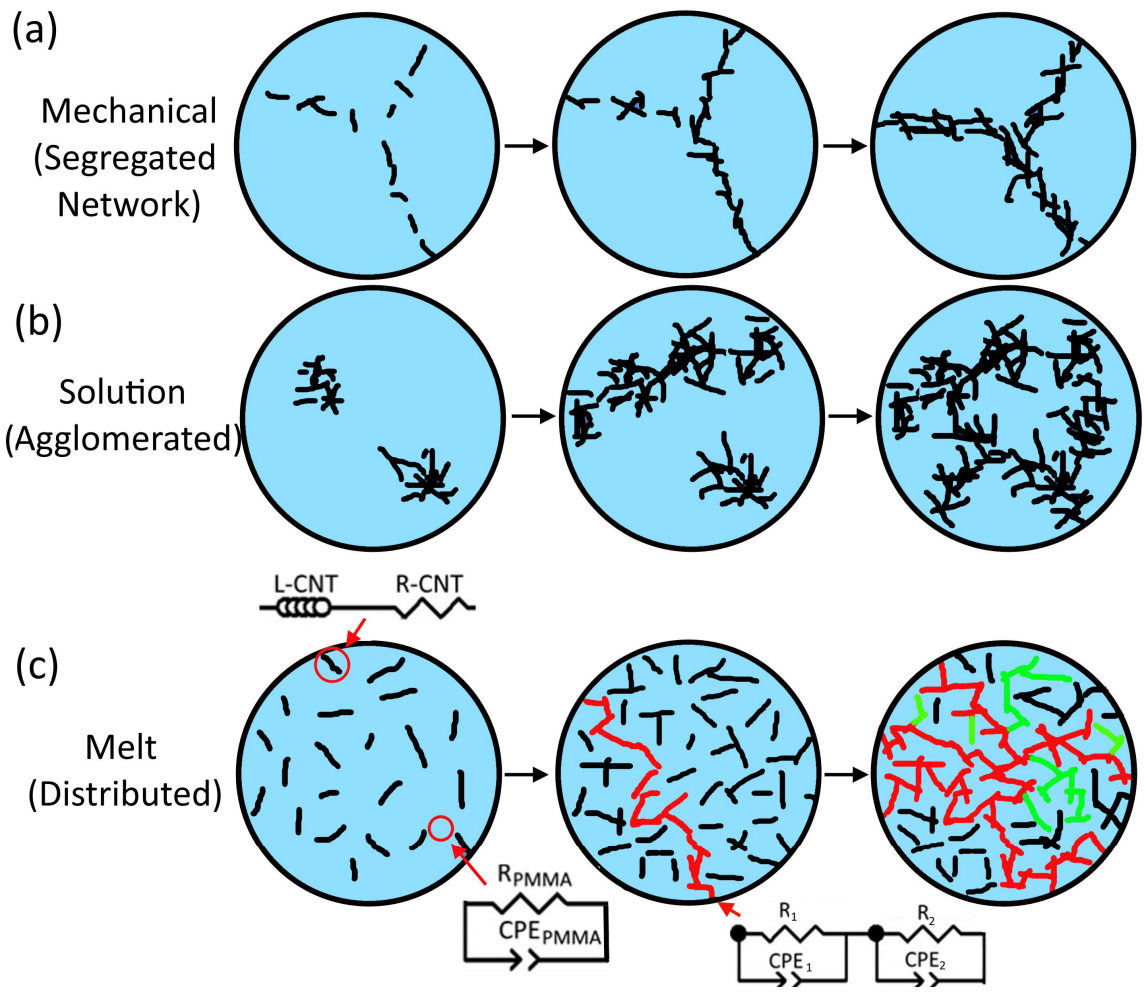

Figure 82 – Formation of paths in CNT/PMMA composites made by three different mixing methods

Table 15 contains the average circuit fitting data for all the MWCNT/PMMA samples before full conductivity is reached. The composites from the lowest concentration of CNT until it almost reaches full conductivity are represented by the circuit (labeled MWCNT/PMMA Composites) under Table 15. As the concentration of CNT increases, more contact points form to start developing paths through the composites. This causes a

decrease in resistivity (R_1 and R_2) which represent the main conducting path resistance. The circuit elements that represent intrinsic CNT properties and PMMA that separates CNT particles remain about the same with increasing CNT concentration. All the equivalent circuit fits of this thesis simultaneously fit all the dielectric functions which results in small standard deviations which are shown in each circuit fit table below the averages.

Table 15 – Equivalent circuit fits for MWCNT/PMMA composites before reaching full conductivity (averages of at least 3 samples with ± standard deviation)

Phr	L_{CNT} (lH)	R_{CNT} (Ω)	R_1 (Ω)	CPE_1-T (F)	CPE_1-P (F)	R_2 (Ω)	CPE_2-T (F)	CPE_2-P (F)	R_{PMMA} (Ω)	CPE_{PMMA}-T (F)	CPE_{PMMA}-P
Mechanically Mixed											
0.005	4.45×10^{-5} ±2.22×10^{-6}	209.3 ±30.42	$1.00 \times 10^{+20}$ ±0	3.60×10^{-12} ±6.05×10^{-14}	0.995 ±8.99×10^{-4}	$3.60 \times 10^{+10}$ ±$1.90 \times 10^{+10}$	2.58×10^{-11} ±6.78×10^{-12}	0.576 ±4.88×10^{-2}	$1.03 \times 10^{+20}$ ±$4.40 \times 10^{+18}$	1.17×10^{-11} ±4.20×10^{-13}	0.988 ±1.21×10^{-3}
0.025	4.35×10^{-5} ±1.54×10^{-6}	229.03 ±1.16	$1.00 \times 10^{+20}$ ±0	3.73×10^{-12} ±6.87×10^{-14}	0.998 ±4.86×10^{-3}	$2.64 \times 10^{+10}$ ±$4.45 \times 10^{+9}$	2.26×10^{-11} ±6.33×10^{-13}	0.602 ±3.25×10^{-3}	$1.00 \times 10^{+20}$ ±0	1.15×10^{-11} ±7.51×10^{-14}	0.988 ±9.02×10^{-5}
0.0375	4.16×10^{-5} ±5.94×10^{-7}	202.07 ±4.91	$3.62 \times 10^{+20}$ ±$4.59 \times 10^{+20}$	4.49×10^{-12} ±6.45×10^{-14}	0.987 ±8.71×10^{-4}	$1.89 \times 10^{+10}$ ±$1.96 \times 10^{+8}$	2.84×10^{-11} ±1.97×10^{-13}	0.598 ±1.83×10^{-3}	$9.20 \times 10^{+19}$ ±$1.25 \times 10^{+19}$	1.24×10^{-11} ±9.22×10^{-14}	0.985 ±3.33×10^{-4}
0.05	4.19×10^{-5} ±1.70×10^{-6}	45.18 ±17.58	$1.26 \times 10^{+9}$ ±$6.96 \times 10^{+8}$	2.79×10^{-10} ±2.32×10^{-10}	0.777 ±1.60×10^{-1}	$5.68 \times 10^{+8}$ ±$3.19 \times 10^{+8}$	3.74×10^{-10} ±2.62×10^{-10}	0.709 ±2.23×10^{-1}	$9.32 \times 10^{+19}$ ±$1.25 \times 10^{+20}$	8.78×10^{-11} ±1.13×10^{-10}	0.844 ±1.95×10^{-1}
0.0875	2.67×10^{-5} ±4.10×10^{-6}	105.89 ±29.82	$1.46 \times 10^{+7}$ ±$1.43 \times 10^{+7}$	1.69×10^{-9} ±6.94×10^{-10}	0.623 ±6.19×10^{-2}	$1.47 \times 10^{+7}$ ±$1.46 \times 10^{+7}$	1.93×10^{-9} ±8.96×10^{-10}	0.669 ±8.16×10^{-2}	$8.05 \times 10^{+19}$ ±$1.96 \times 10^{+19}$	2.67×10^{-11} ±1.72×10^{-12}	0.951 ±2.52×10^{-3}
0.15	4.60×10^{-5} ±7.75×10^{-7}	155.87 ±11.00	$1.31 \times 10^{+20}$ ±$5.12 \times 10^{+19}$	8.66×10^{-12} ±4.82×10^{-13}	0.925 ±1.17×10^{-2}	$6.59 \times 10^{+9}$ ±$1.57 \times 10^{+9}$	6.26×10^{-11} ±6.02×10^{-13}	0.579 ±3.60×10^{-3}	$1.25 \times 10^{+20}$ ±$6.6 \times 10^{+19}$	1.40×10^{-11} ±1.50×10^{-13}	0.979 ±2.47×10^{-4}
Solution Mixed											
0.01	3.09×10^{-5} ±1.27×10^{-6}	232.93 ±22.59	$9.74 \times 10^{+19}$ ±$8.97 \times 10^{+19}$	5.45×10^{-12} ±4.68×10^{-14}	0.999 ±1.59×10^{-3}	$8.36 \times 10^{+9}$ ±$3.08 \times 10^{+8}$	5.45×10^{-11} ±7.91×10^{-13}	0.592 ±6.81×10^{-4}	$7.93 \times 10^{+19}$ ±$3.59 \times 10^{+19}$	1.32×10^{-11} ±2.30×10^{-13}	0.991 ±7.51×10^{-5}
0.1	3.10×10^{-5} ±2.27×10^{-6}	221.23 ±18.69	$9.50 \times 10^{+19}$ ±$4.72 \times 10^{+18}$	5.41×10^{-12} ±1.83×10^{-13}	0.993 ±4.32×10^{-3}	$7.01 \times 10^{+9}$ ±$4.58 \times 10^{+8}$	5.75×10^{-11} ±9.22×10^{-13}	0.587 ±4.80×10^{-3}	$1.05 \times 10^{+20}$ ±$4.6 \times 10^{+18}$	1.30×10^{-11} ±3.50×10^{-13}	0.991 ±5.12×10^{-4}
1	2.99×10^{-5} ±4.94×10^{-7}	181.05 ±4.74	$1.07 \times 10^{+20}$ ±$9.83 \times 10^{+18}$	5.16×10^{-12} ±2.00×10^{-13}	0.998 ±3.80×10^{-3}	$1.30 \times 10^{+10}$ ±$1.25 \times 10^{+9}$	3.87×10^{-11} ±2.42×10^{-12}	0.603 ±1.73×10^{-3}	$9.54 \times 10^{+19}$ ±$6.50 \times 10^{+18}$	1.33×10^{-11} ±2.62×10^{-13}	0.992 ±3.54×10^{-5}
1.5	3.57×10^{-5} ±6.5×10^{-6}	124.66 ±47.86	$1.23 \times 10^{+20}$ ±$3.99 \times 10^{+19}$	4.96×10^{-12} ±6.35×10^{-13}	1.01 ±6.36×10^{-3}	$1.55 \times 10^{+10}$ ±$1.75 \times 10^{+9}$	6.09×10^{-11} ±1.68×10^{-11}	0.540 ±6.67×10^{-2}	$9.81 \times 10^{+19}$ ±$1.71 \times 10^{+19}$	1.47×10^{-11} ±6.72×10^{-13}	0.988 ±2.55×10^{-3}
Melt Mixed											
0.01	3.37×10^{-5} ±4.67×10^{-7}	260.57 ±10.66	$7.31 \times 10^{+19}$ ±$2.89 \times 10^{+19}$	4.44×10^{-12} ±2.24×10^{-14}	1.00 ±4.16×10^{-3}	$1.94 \times 10^{+10}$ ±$1.99 \times 10^{+9}$	2.97×10^{-11} ±1.09×10^{-12}	0.605 ±2.69×10^{-3}	$5.77 \times 10^{+19}$ ±$5.23 \times 10^{+19}$	1.24×10^{-11} ±1.10×10^{-13}	0.990 ±1.25×10^{-4}
0.1	3.45×10^{-5} ±2.37×10^{-6}	251.23 ±22.93	$9.90 \times 10^{+19}$ ±$1.93 \times 10^{+19}$	4.32×10^{-12} ±1.93×10^{-13}	1.00 ±1.53×10^{-3}	$2.10 \times 10^{+10}$ ±$4.30 \times 10^{+9}$	2.89×10^{-11} ±1.21×10^{-12}	0.605 ±1.81×10^{-3}	$9.98 \times 10^{+19}$ ±$4.36 \times 10^{+18}$	1.24×10^{-11} ±4.50×10^{-13}	0.990 ±1.23×10^{-4}
0.5	2.90×10^{-5} ±2.86×10^{-6}	266.70 ±19.19	$1.00 \times 10^{+20}$ ±0	4.52×10^{-12} ±3.13×10^{-13}	0.991 ±1.37×10^{-2}	$1.43 \times 10^{+10}$ ±$6.19 \times 10^{+9}$	3.07×10^{-11} ±3.83×10^{-12}	0.614 ±8.51×10^{-3}	$1.00 \times 10^{+20}$ ±0	1.24×10^{-11} ±2.80×10^{-13}	0.991 ±1.48×10^{-3}
1	3.22×10^{-5} ±6.90×10^{-7}	224.33 ±4.62	$1.09 \times 10^{+20}$ ±$1.99 \times 10^{+19}$	4.43×10^{-12} ±3.24×10^{-14}	1.00 ±5.77×10^{-4}	$1.89 \times 10^{+10}$ ±$2.86 \times 10^{+8}$	2.88×10^{-11} ±2.03×10^{-13}	0.606 ±3.56×10^{-4}	$1.16 \times 10^{+20}$ ±$3.47 \times 10^{+19}$	1.31×10^{-11} ±1.61×10^{-13}	0.990 ±4.62×10^{-5}
2	5.32×10^{-5} ±7.36×10^{-6}	125.2 ±0	$2.79 \times 10^{+11}$ ±0	2.27×10^{-12} ±1.64×10^{-10}	0.617 ±1.86×10^{-1}	$3.44 \times 10^{+10}$ ±$2.70 \times 10^{+10}$	8.92×10^{-11} ±5.94×10^{-11}	0.684 ±1.01×10^{-1}	$6.85 \times 10^{+19}$ ±$5.46 \times 10^{+19}$	1.71×10^{-11} ±1.15×10^{-12}	0.974 ±3.75×10^{-3}
3	3.13×10^{-5} ±1.15×10^{-6}	139.67 ±14.86	$9.63 \times 10^{+19}$ ±$6.34 \times 10^{+18}$	8.54×10^{-12} ±1.09×10^{-12}	0.963 ±1.30×10^{-2}	$1.18 \times 10^{+10}$ ±$4.62 \times 10^{+9}$	6.04×10^{-11} ±8.86×10^{-12}	0.593 ±5.43×10^{-3}	$1.00 \times 10^{+20}$ ±$1.91 \times 10^{+20}$	1.71×10^{-11} ±4.18×10^{-13}	0.983 ±1.41×10^{-3}

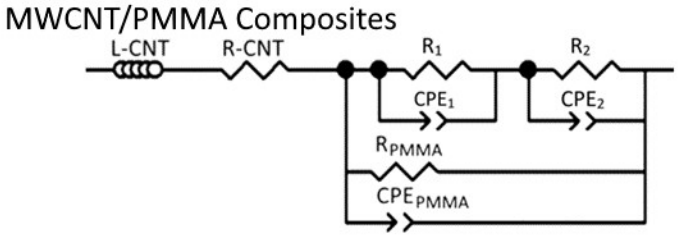

Table 16 contains the circuit fitting data for all of the MWCNT/PMMA samples after percolation is reached. In contrast to samples before percolation, the circuits (a-g) show that the composites after percolation vary more depending on the connectivity of the path. As the concentration increases, the resistivity decreases and inductance increases. Some samples do deviate back to a more insulating representative circuits which indicates that fewer paths formed for those samples. With the mechanically mixed samples, the samples changed from the previous insulating to conductive equivalent circuits without intermediate circuits that form with the other two mixing methods. The circuits developed do not match the equivalent circuit of CNT alone (Figure 78) because even at high concentrations the insulating matrix does interact with the network and is represented by the capacitive and some resistive behavior. The equivalent circuit for CNT alone is solely made of an inductor (L), a resistor (R) and a parallel RL in series. Therefore, the increased presence of inductance within the developed circuits is the inter- and intra- particle interaction of the CNTs.

Table 16 – Circuits used for MWCNT/PMMA samples and table of circuit values after percolation (averages of at least 3 samples with ± standard deviation)

Phr	Circuit	L_1 (IH)	CPE_1-T (F)	CPE_1-P (F)	R_1 (Ω)	R_2 (Ω)	L_2 (IH)	CPE_2-T (F)	CPE_2-P (F)	R_3 (Ω)	L_3 (IH)	CPE_3-T (F)	CPE_3-P (F)
Mechanically Mixed													
0.1	a	3.46×10^{-6} $\pm 2.96 \times 10^{-7}$	2.41×10^{-10} $\pm 5.37 \times 10^{-12}$	0.971 $\pm 8.10 \times 10^{-3}$	118.95 ±19.87	0.313 $\pm 1.04 \times 10^{-2}$	7.30×10^{-7} $\pm 6.04 \times 10^{-8}$	1.97×10^{-5} $\pm 1.21 \times 10^{-5}$	1.01 $\pm 5.74 \times 10^{-2}$				
0.1	b	6.31×10^{-6}	3.38×10^{-10}	0.973	212.4	0.540	1.23×10^{-6}	2.04×10^{-5}	0.954		4.39×10^{-6}		
0.2	a	9.12×10^{-7} $\pm 5.20 \times 10^{-7}$	-5.02×10^{-5} $\pm 8.70 \times 10^{-5}$	0.433 $\pm 1.84 \times 10^{-1}$	12.3 ±0.332	2.11 ±0.639	1.22×10^{-6} $\pm 2.16 \times 10^{-7}$	7.34×10^{-4} $\pm 1.36 \times 10^{-3}$	0.558 $\pm 1.39 \times 10^{-1}$				
0.25	a	8.07×10^{-7} $\pm 1.07 \times 10^{-7}$	-5.66×10^{-5} $\pm 5.24 \times 10^{-5}$	0.459 $\pm 4.43 \times 10^{-2}$	8.34 ±2.60	2.13 ±0.243	1.27×10^{-6} $\pm 6.53 \times 10^{-8}$	1.92×10^{-4} $\pm 9.51 \times 10^{-5}$	0.590 $\pm 2.59 \times 10^{-2}$				
Solution Mixed													
2	c	1.96×10^{-5} $\pm 2.14 \times 10^{-6}$	2.88×10^{-11} $\pm 4.44 \times 10^{-12}$	0.967 $\pm 3.80 \times 10^{-3}$	$9.08 \times 10^{+3}$ $\pm 2.77 \times 10^{3}$								
2.25	d	2.68×10^{-5} $\pm 6.85 \times 10^{-6}$	2.61×10^{-9} $\pm 2.94 \times 10^{-9}$	1.08 ±0.147	97.2 ±109	11.58 ±8.78		1.81×10^{-7} $\pm 1.99 \times 10^{-7}$	1.20 ±0.199	2.44×10^{3} $\pm 8.15 \times 10^{2}$		2.55×10^{-11} $\pm 1.41 \times 10^{-11}$	0.997 $\pm 3.11 \times 10^{-2}$
3	a	2.95×10^{-6}	2.31×10^{-10}	0.997	81.48	0.269	7.03×10^{-7}	4.94×10^{-5}	0.934				
3	b	4.60×10^{-6}	4.14×10^{-10}	0.985	131	0.326	6.57×10^{-7}	1.42×10^{-5}	1.03		4.14×10^{-10}		
4	a	2.99×10^{-6} $\pm 1.67 \times 10^{-7}$	2.08×10^{-10} $\pm 1.15 \times 10^{-11}$	1.00 $\pm 7.69 \times 10^{-3}$	82 ±12.2	0.271 $\pm 4.15 \times 10^{-3}$	7.23×10^{-7} $\pm 6.99 \times 10^{-8}$	6.71×10^{-5} $\pm 4.41 \times 10^{-5}$	0.915 $\pm 6.42 \times 10^{-2}$				
5	a	2.88×10^{-6} $\pm 3.75 \times 10^{-7}$	2.32×10^{-10} $\pm 3.47 \times 10^{-11}$	1.00 $\pm 1.39 \times 10^{-2}$	75.8 ±24.3	1.49 ±0.667	1.00×10^{-6} $\pm 5.11 \times 10^{-7}$	2.43×10^{-4} $\pm 3.13 \times 10^{-4}$	0.849 ±0.219				
Melt Mixed													
4	e		2.29×10^{-10} $\pm 5.33 \times 10^{-11}$	0.862 $\pm 8.10 \times 10^{-3}$	$3.88 \times 10^{+5}$ $\pm 3.50 \times 10^{+5}$	$4.72 \times 10^{+4}$ $\pm 1.77 \times 10^{+4}$		7.34×10^{-10} $\pm 1.55 \times 10^{-11}$	0.930 $\pm 1.28 \times 10^{-2}$				
6	e		3.48×10^{-10} $\pm 4.86 \times 10^{-11}$	0.922 $\pm 1.57 \times 10^{-2}$	$6.23 \times 10^{+3}$ ±246	$8.00 \times 10^{+3}$ $\pm 3.93 \times 10^{+3}$		5.53×10^{-10} $\pm 6.23 \times 10^{-11}$	0.821 $\pm 3.71 \times 10^{-3}$				
8	e		4.99×10^{-10} $\pm 1.60 \times 10^{-10}$	0.849 $\pm 2.89 \times 10^{-2}$	$3.57 \times 10^{+3}$ $\pm 1.85 \times 10^{+3}$	$3.96 \times 10^{+3}$ $\pm 2.89 \times 10^{+3}$		2.86×10^{-10} $\pm 2.02 \times 10^{-11}$	0.886 $\pm 3.94 \times 10^{-2}$				
10	f	5.18×10^{-6} $\pm 6.29 \times 10^{-7}$	3.38×10^{-11} $\pm 2.5 \times 10^{-12}$	1.09 $\pm 9.90 \times 10^{-3}$	$1.85 \times 10^{+2}$ $\pm 4.31 \times 10^{+1}$	3.97 ±1.24	2.90×10^{-6} $\pm 4.86 \times 10^{-7}$	9.95×10^{-6} $\pm 1.05 \times 10^{-5}$	0.987 $\pm 2.96 \times 10^{-3}$	0.663 ±0.131		4.62×10^{-8} $\pm 3.78 \times 10^{-9}$	1.04 $\pm 2.97 \times 10^{-2}$
12	f	5.12×10^{-6} $\pm 3.57 \times 10^{-7}$	5.78×10^{-11} $\pm 3.37 \times 10^{-12}$	1.05 $\pm 1.02 \times 10^{-2}$	$2.12 \times 10^{+2}$ ±34.2	4.23 ±0.868	3.97×10^{-6} $\pm 7.65 \times 10^{-7}$	2.33×10^{-5} $\pm 6.55 \times 10^{-7}$	0.957 $\pm 9.56 \times 10^{-2}$	0.832 ±0.114		5.75×10^{-8} $\pm 3.25 \times 10^{-9}$	1.02 $\pm 1.99 \times 10^{-2}$
15	f	3.81×10^{-6} $\pm 1.31 \times 10^{-6}$	3.41×10^{-11} $\pm 2.11 \times 10^{-12}$	1.13 $\pm 4.74 \times 10^{-2}$	$1.06 \times 10^{+2}$ ±68.6	3.61 ±0.738	1.56×10^{-6} $\pm 1.41 \times 10^{-6}$	3.31×10^{-5} $\pm 1.24 \times 10^{-5}$	0.973 $\pm 1.78 \times 10^{-2}$	0.406 ±0.232		1.49×10^{-7} $\pm 1.49 \times 10^{-7}$	0.971 ±0.121
15	g	2.61×10^{-6}	9.12×10^{-10}	0.885	1.13 × 10^{+2}	0.349	5.38×10^{-6}	3.45×10^{-5}	0.937		9.43×10^{-7}		

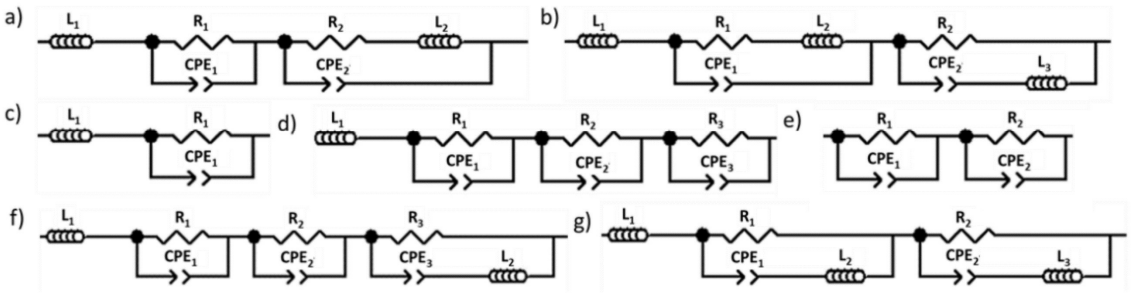

To summarize the previous two tables, Figure 83 demonstrates the progression of the circuit elements with increasing composition using the complex admittance data and fitting for representative samples. The trend from capacitive behavior to more inductive

behavior is seen in all three composite types. The melt mixed composites have a different final circuit that is likely due to the more even distribution of CNT. The PMMA has a stronger presence in a distributed matrix resulting in more capacitance. When reading the complex admittance graphs, insulating composites data show in the 4^{th} quadrant (Figure 83 a and b), and conductive composites data show in the 1^{st} quadrant (Figure 83 c-e). The mechanically mixed composites showed the highest conductivity (see Table 9 in Chapter 4), and it shows in the complex admittance plot as a partial semicircle.

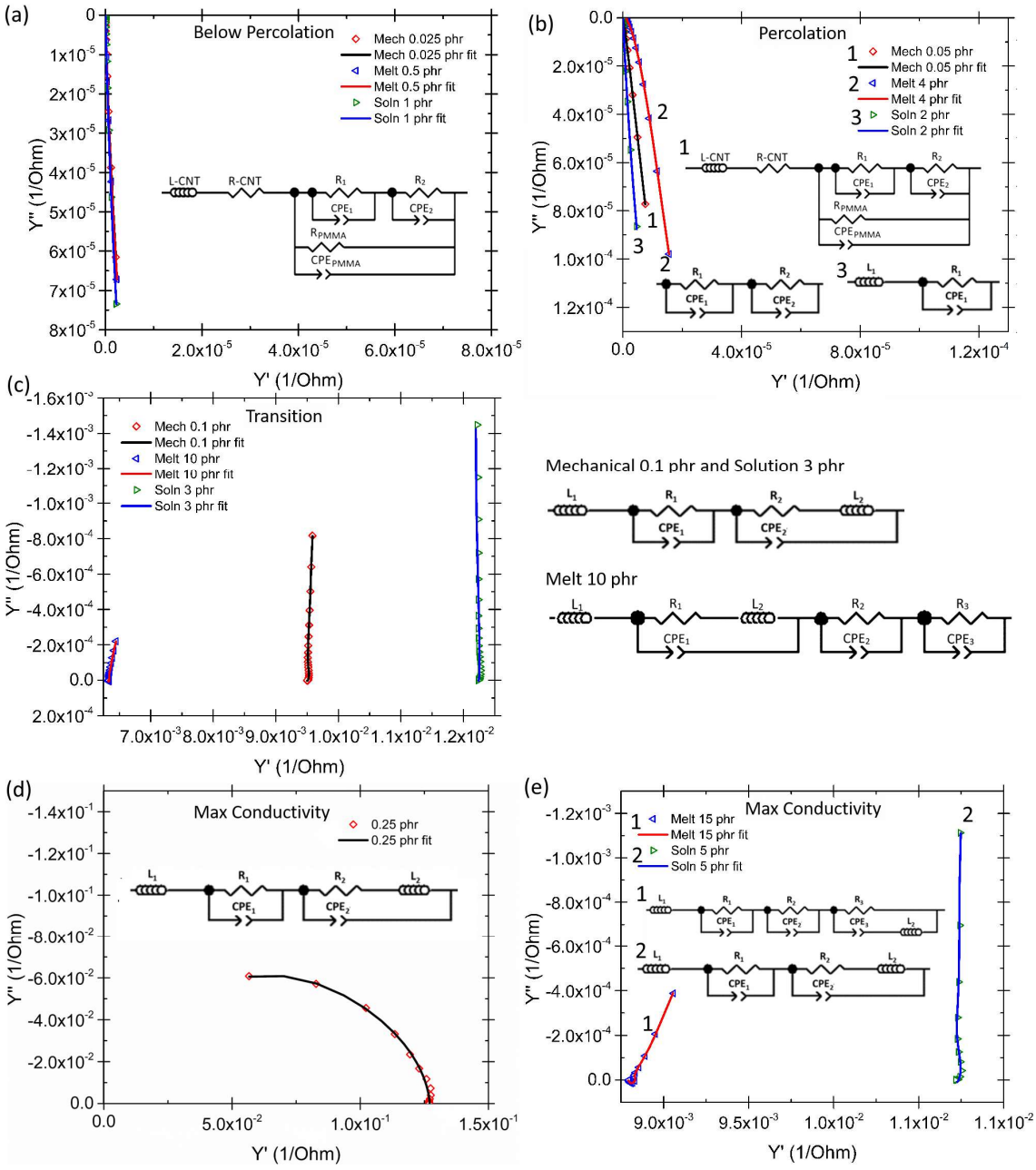

Figure 83 – Complex admittance of select MWCNT/PMMA composite samples with fitted data and representative equivalent circuits

9.3 Equivalent Circuit Modeling of the Effect of Particle Shape on Electrical Properties (SiC/PMMA)

In all three SiC/PMMA composites with different SiC particle shapes, the same two equivalent circuits are used to fit to the impedance data. The two circuits are shown at the bottom of each table of circuit values (Table 17, Table 18, and Table 19). The nano-sized SiC/PMMA composite equivalent circuit values are shown in Table 17. As concentration increases, resistance decreases (R_1 and R_2), CPE_1-T and -P increases (capacitance), CPE_2-T and -P remains about the same, and CPE_3 -T and -P shows a small increase. This indicates that as the concentration increases, the CPE_2-T and -P is not strongly affected by the formation of percolated paths with the nano-SiC and likely results from the PMMA interfering with the conductive paths. This theory is supported by the fact that the value of CPE_2-T is in the range of 10^{-11} F, which is the same as seen in the equivalent circuit for neat PMMA (Figure 80). With the other values, the increase in nano-SiC within the matrix causes more connections to form and cause the observed reductions in R and increases in CPE. With the PMMA interfering, the SiC in the composites cannot reach values comparable to the nano-SiC powder fitting (Figure 79).

Table 17 – Equivalent circuit fit values for nano-sized SiC / PMMA composites

(averages of at least 3 samples with ± standard deviation)

phr	Circuit	L_1 (IH)	R_1 (Ω)	CPE_1-T (F)	CPE_1-P (F)	R_2 (Ω)	CPE_2-P (F)	CPE_2-T (F)	CPE_3-T (F)	CPE_3-P (F)
0.1	a	4.64×10^{-5} ±5.28×10^{-6}	3.04×10^{12} ±8.23×10^{11}	1.84×10^{-11} ±1.93×10^{-12}	1.03 ±0.033	2.84×10^{10} ±1.25×10^{10}	3.05×10^{-11} ±1.25×10^{-11}	0.968 ±0.005	1.41×10^{-10} ±1.01×10^{-10}	0.616 ±0.046
0.5	a	4.62×10^{-5} ±1.24×10^{-6}	5.00×10^{19} ±7.07×10^{19}	1.72×10^{-11} ±4.31×10^{-13}	1.00 ±0.016	9.18×10^{10} ±9.87×10^{10}	4.72×10^{-11} ±1.28×10^{-11}	0.970 ±0.011	3.02×10^{-10} ±1.79×10^{-10}	0.572 ±0.029
0.5	b		4.39×10^{12}	1.72×10^{-11}	0.997	2.94×10^{9}	4.18×10^{-11}	0.986	2.73×10^{-10}	0.634
1	a	4.95×10^{-5} ±6.89×10^{-6}	5.00×10^{19} ±7.07×10^{19}	1.98×10^{-11} ±1.80×10^{-12}	0.972 ±0.004	5.00×10^{19} ±7.07×10^{19}	3.28×10^{-11} ±3.93×10^{-12}	1.05 ±0.006	3.29×10^{-10} ±7.11×10^{-11}	0.665 ±0.011
1	b		1.00×10^{20}	6.06×10^{-11}	1.51	1.58×10^{11}	1.01×10^{-11}	1.00	1.26×10^{-11}	0.817
2	b		4.23×10^{11} ±7.15×10^{11}	7.41×10^{-11} ±3.96×10^{-11}	0.963 ±0.023	9.60×10^{19} ±6.95×10^{18}	2.00×10^{-11} ±3.87×10^{-12}	0.991 ±0.003	9.92×10^{-11} ±2.21×10^{-11}	0.613 ±0.071
3	b		4.70×10^{8} ±3.00×10^{8}	5.29×10^{-10} ±2.17×10^{-10}	0.881 ±0.038	1.48×10^{9} ±7.15×10^{8}	1.34×10^{-11} ±1.1×10^{-12}	1.00 ±0.007	1.70×10^{-10} ±1.44×10^{-11}	0.602 ±0.013
7.5	b		1.37×10^{7} ±1.46×10^{7}	6.70×10^{-10} ±3.04×10^{-10}	0.837 ±0.027	3.72×10^{7} ±3.01×10^{7}	8.85×10^{-12} ±3.85×10^{-12}	1.06 ±0.044	7.47×10^{-10} ±3.31×10^{-10}	0.633 ±0.070
10	b		3.05×10^{5} ±3.51×10^{5}	5.19×10^{-7} ±8.76×10^{-7}	0.697 ±0.226	6.48×10^{6} ±3.42×10^{6}	$2.35 \times 10_{-11}$ ±1.09×10^{-11}	0.986 ±0.025	2.69×10^{-9} ±9.30×10^{-10}	0.518 ±0.056
12	b		3.65×10^{4} ±1.34×10^{4}	1.74×10^{-9} ±1.60×10^{-9}	0.855 ±0.083	1.10×10^{7} ±3.91×10^{6}	2.81×10^{-11} ±1.54×10^{-11}	0.989 ±0.061	2.55×10^{-9} ±1.37×10^{-9}	0.500 ±0.078
15	b		2.77×10^{4} ±8.69×10^{2}	1.58×10^{-9} ±4.56×10^{-10}	0.855 ±0.036	3.56×10^{6} ±1.06×10^{6}	3.72×10^{-11} ±5.93×10^{-12}	0.962 ±0.007	4.34×10^{-9} ±1.94×10^{-9}	0.487 ±0.022

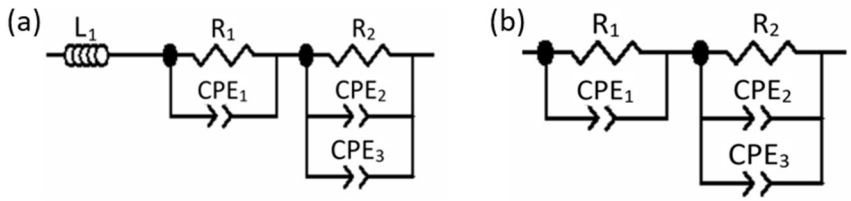

The micron-sized SiC/PMMA composite equivalent circuit values are shown in Table 18. As concentration increases, resistance decreases with spikes to higher values (R_1 and R_2), CPE_1-T and -P increases slightly, and CPE_2-T and -P and CPE_3 -T and -P remain about the same. As with the nano-SiC/PMMA composites, the CPE_2 values match that of PMMA CPE values, further supporting that CPE_2 represent the PMMA contribution. The values for the micron-SiC /PMMA composites are much more unstable (equivalent circuits change more) than for the nano-SiC /PMMA. The sample fits often switch between the two

circuits used (Table 18 circuits column) until it stabilizes after 5 phr. Despite percolation theory suggesting a low percolation around 2 phr, the equivalent circuit fitting suggests that percolation is completed after 5 phr.

Table 18 – Equivalent circuit fit values for micron-sized SiC / PMMA composites (averages of at least 3 samples with ± standard deviation)

phr	Circuit	L_1 (lH)	R_1 (Ω)	CPE_1-T (F)	CPE_1-P (F)	R_2 (Ω)	CPE_2-P (F)	CPE_2-T (F)	CPE_3-T (F)	CPE_3-P (F)
0.1	a	5.03×10^{-5} $\pm 2.23 \times 10^{-6}$	1.00×10^{20} ±0	1.74×10^{-11} $\pm 4.25 \times 10^{-13}$	0.984 ±0.013	5.47×10^{9} $\pm 6.12 \times 10^{9}$	4.82×10^{-11} $\pm 6.66 \times 10^{-12}$	1.02 ±0.052	6.96×10^{-10} $\pm 3.66 \times 10^{-10}$	0.594 ±0.046
0.5	a	5.50×10^{-5} $\pm 1.11 \times 10^{-7}$	5.05×10^{19} $\pm 2.79 \times 10^{19}$	1.76×10^{-11} $\pm 1.05 \times 10^{-13}$	0.983 ±0	6.89×10^{19} $\pm 4.40 \times 10^{19}$	6.58×10^{-11} $\pm 9.83 \times 10^{-14}$	0.986 ±0.003	7.27×10^{-10} $\pm 3.85 \times 10^{-11}$	0.524 ±0.001
0.5	b		6.03×10^{11}	1.98×10^{-11}	1.05	2.58×10^{10}	5.31×10^{-11}	0.929	2.23×10^{-10}	0.407
1	a	5.00×10^{-5} $\pm 7.81 \times 10^{-7}$	5.00×10^{19} $\pm 7.07 \times 10^{19}$	1.72×10^{-11} $\pm 4.84 \times 10^{-13}$	0.986 ±0	1.00×10^{20} ±0	5.9×10^{-11} $\pm 1.85 \times 10^{-12}$	0.984 ±0.002	4.97×10^{-10} $\pm 1.99 \times 10^{-11}$	0.551 ±0.009
1	b		1.64×10^{19}	2.00×10^{-11}	0.987	2.66×10^{8}	1.16×10^{-11}	1.00	3.97×10^{-10}	0.835
2	a	5.08×10^{-5} $\pm 4.58 \times 10^{-6}$	1.41×10^{13} $\pm 1.22 \times 10^{12}$	1.92×10^{-11} $\pm 1.71 \times 10^{-12}$	0.978 ±0.014	1.00×10^{20} ±0	4.39×10^{-11} $\pm 1.90 \times 10^{-11}$	1.028 ±0.072	4.33×10^{-10} $\pm 3.84 \times 10^{-11}$	0.617 ±0.085
2	b		6.70×10^{20}	2.27×10^{-11}	1.017	3.07×10^{20}	2.24×10^{-11}	0.989	6.86×10^{-11}	0.735
3	a	4.45×10^{-5} $\pm 3.80 \times 10^{-6}$	9.11×10^{12} $\pm 5.29 \times 10^{12}$	2.57×10^{-11} $\pm 9.56 \times 10^{-12}$	0.964 ±0.017	5.00×10^{19} $\pm 7.07 \times 10^{19}$	2.85×10^{-11} $\pm 2.19 \times 10^{-11}$	1.06 ±0.046	2.72×10^{-10} $\pm 2.13 \times 10^{-10}$	0.700 ±0.121
3	b		3.42×10^{12}	2.5×10^{-11}	1.02	2.7×10^{17}	2.99×10^{-11}	0.978	1.1×10^{-10}	0.669
5	a	4.14×10^{-5} $\pm 5.66 \times 10^{-7}$	5.00×10^{19} $\pm 7.07 \times 10^{19}$	3.91×10^{-11} $\pm 6.69 \times 10^{-12}$	1.01 ±0.090	4.25×10^{10} $\pm 1.16 \times 10^{10}$	1.6×10^{-11} $\pm 3.97 \times 10^{-12}$	1.03 ±0.073	7.69×10^{-11} $\pm 4.17 \times 10^{-11}$	0.739 ±0.069
5	b		6.58×10^{8}	1.42×10^{-9}	0.949	2.95×10^{9}	2.19×10^{-11}	0.977	1.46×10^{-10}	0.626
7.5	b		3.88×10^{10} $\pm 3.44 \times 10^{10}$	4.92×10^{-10} $\pm 6.39 \times 10^{-10}$	0.921 ±0.025	1.19×10^{10} $\pm 9.34 \times 10^{9}$	2.12×10^{-11} $\pm 3.04 \times 10^{-12}$	0.984 ±0.017	1.41×10^{-10} $\pm 1.04 \times 10^{-10}$	0.653 ±0.055
10	b		1.33×10^{9} $\pm 1.95 \times 10^{9}$	2.81×10^{-9} $\pm 2.37 \times 10^{-9}$	0.901 ±0.039	3.02×10^{9} $\pm 3.07 \times 10^{9}$	2.32×10^{-11} $\pm 3.00 \times 10^{-12}$	0.970 ±0.006	3.40×10^{-10} $\pm 3.38 \times 10^{-10}$	0.607 ±0.042
12	b		7.78×10^{8} $\pm 6.10 \times 10^{8}$	1.96×10^{-9} $\pm 1.00 \times 10^{-9}$	0.915 ±0.019	2.70×10^{9} $\pm 1.84 \times 10^{9}$	2.35×10^{-11} $\pm 2.62 \times 10^{-12}$	0.970 ±0.003	2.08×10^{-10} $\pm 7.49 \times 10^{-11}$	0.609 ±0.027
15	b		2.19×10^{5} $\pm 2.82 \times 10^{5}$	4.76×10^{-9} $\pm 4.33 \times 10^{-9}$	±0.818 ±0.044	3.25×10^{8} $\pm 3.32 \times 10^{7}$	2.26×10^{-11} $\pm 3.08 \times 10^{-12}$	0.978 ±0.015	5.89×10^{-10} $\pm 2.42 \times 10^{-10}$	0.582 ±0.037

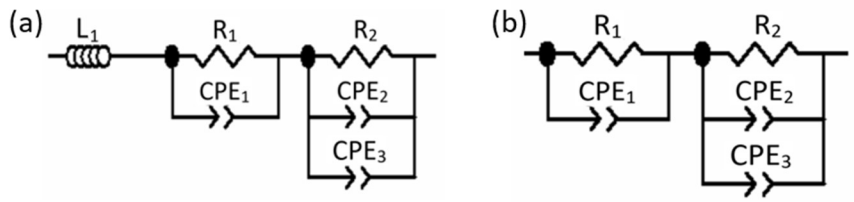

The whisker SiC/PMMA composite equivalent circuit values are shown in Table 19. As concentration increases, R_1 decreases, R_2 increases, CPE_1-T and -P and CPE_2-T and -P increase slightly, and CPE_3 -T and -P increases. The resistance behavior within the circuits is different than the behavior observed in the previous two cases. The anisotropy and length of the SiC_w is likely the cause of the difference in trends between the whiskers and the other two shapes. Its length probably caused it to interact more with the PMMA than the nano- and micron- SiC. Since its length is closer in size to the PMMA than the others, it is more difficult for it to fit in the grain-like boundaries. Since the CPE_2 increases slightly, this supports the idea that the PMMA is not containing the SiC_w like it did with the other two.

Table 19 – Equivalent circuit fit values for whisker SiC / PMMA composites (averages of at least 3 samples with ± standard deviation)

phr	Circuit	L_1 (IH)	R_1 (Ω)	CPE_1-T (F)	CPE_1-P (F)	R_2 (Ω)	CPE_2-P (F)	CPE_2-T (F)	CPE_3-T (F)	CPE_3-P (F)
0.1	a	7.62×10^{-5} $\pm 2.13 \times 10^{-6}$	7.57×10^{19} $\pm 4.21 \times 10^{19}$	1.77×10^{-11} $\pm 1.38 \times 10^{-12}$	1.02 ±0.057	1.48×10^{10} $\pm 1.92 \times 10^{10}$	4.59×10^{-11} $\pm 2.60 \times 10^{-11}$	0.974 ±0.013	5.13×10^{-10} $\pm 4.75 \times 10^{-10}$	0.580 ±0.082
0.5	a	7.40×10^{-5} $\pm 6.26 \times 10^{-7}$	1.00×10^{20} ±0	1.83×10^{-11} $\pm 4.60 \times 10^{-13}$	0.989 ±0.010	3.40×10^{9} $\pm 3.98 \times 10^{9}$	6.16×10^{-11} $\pm 1.11 \times 10^{-11}$	0.971 ±0.016	6.94×10^{-10} $\pm 3.76 \times 10^{-10}$	0.540 ±0.012
0.5	b		1.00×10^{20}	2.14×10^{-11}	1.05	2.18×10^{10}	2.40×10^{-11}	0.970	9.91×10^{-11}	0.656
1	b		6.54×10^{19} $\pm 4.96 \times 10^{19}$	2.07×10^{-11} $\pm 1.20 \times 10^{-12}$	1.02 ±0.022	3.33×10^{19} $\pm 5.77 \times 10^{19}$	3.67×10^{-11} $\pm 1.48 \times 10^{-11}$	0.968 ±0.002	2.51×10^{-10} $\pm 2.19 \times 10^{-10}$	0.612 ±0.050
2	b		6.21×10^{12} $\pm 3.72 \times 10^{12}$	2.40×10^{-11} $\pm 7.25 \times 10^{-13}$	0.994 ±0.053	1.34×10^{10} $\pm 2.22 \times 10^{10}$	1.97×10^{-11} $\pm 5.91 \times 10^{-12}$	1.08 ±0.098	4.61×10^{-10} $\pm 3.60 \times 10^{-10}$	0.691 ±0.030
3	b		5.00×10^{19} $\pm 7.07 \times 10^{19}$	3.25×10^{-10} $\pm 4.22 \times 10^{-10}$	0.876 ±0.117	5.00×10^{19} $\pm 7.07 \times 10^{19}$	7.31×10^{-12} $\pm 1.01 \times 10^{-11}$	1.23 ±0.066	4.95×10^{-10} $\pm 6.68 \times 10^{-10}$	0.855 ±0.140
3	a	6.78×10^{-5}	1.00×10^{20}	2.27×10^{-11}	0.962	2.06×10^{8}	2.24×10^{-11}	1.12	9.43×10^{-10}	0.680
7.5	b		5.11×10^{19} $\pm 5.00 \times 10^{19}$	2.48×10^{-11} $\pm 1.42 \times 10^{-13}$	0.986 ±0.021	8.00×10^{19} $\pm 3.47 \times 10^{19}$	5.53×10^{-11} $\pm 1.60 \times 10^{-11}$	0.979 ±0.029	5.21×10^{-10} $\pm 2.79 \times 10^{-10}$	0.581 ±0.020
10	b		4.97×10^{8} $\pm 1.33 \times 10^{8}$	5.46×10^{-11} $\pm 7.37 \times 10^{-12}$	0.932 ±0.007	1.00×10^{20} ±0	3.10×10^{-10} $\pm 4.20 \times 10^{-11}$	0.960 ±0.006	4.97×10^{-8} $\pm 1.72 \times 10^{-8}$	0.244 ±0.053
12	b		4.94×10^{7} $\pm 2.93 \times 10^{7}$	1.38×10^{-10} $\pm 2.22 \times 10^{-11}$	0.890 ±0.006	9.11×10^{19} $\pm 1.54 \times 10^{19}$	2.55×10^{-10} $\pm 5.89 \times 10^{-12}$	0.919 ±0.013	2.32×10^{-7} $\pm 1.47 \times 10^{-7}$	0.126 ±0.025
15	b		2.50×10^{6} $\pm 8.24 \times 10^{5}$	5.1×10^{-10} $\pm 1.26 \times 10^{-10}$	0.837 ±0.008	1.00×10^{20} $\pm 1.15 \times 10^{16}$	3.21×10^{-10} $\pm 3.65 \times 10^{-11}$	0.882 ±0.006	2.13×10^{-6} $\pm 1.27 \times 10^{-6}$	0.057 ±0.023

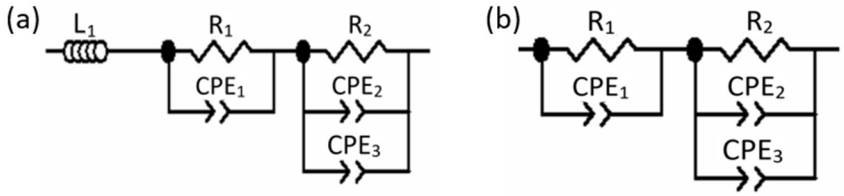

Figure 84 shows the complex impedance graphs (Z" vs Z') and fit data for select SiC / PMMA composites. As the concentration increases, the resistance decreased in all cases. With complex impedance graphs, where semicircles meet the real impedance (Z') axis indicates the resistance. In Figure 84a, the vertical data are a portion of a very large semicircle due to the resistance being too large to be measured in the range of frequencies used. The semicircles form at and after percolation in the complex impedance for the

SiC/PMMA composites with increasing concentration (Figure 84 b-d). The size of the semicircles decreases with increasing concentration which causes a decrease in resistance.

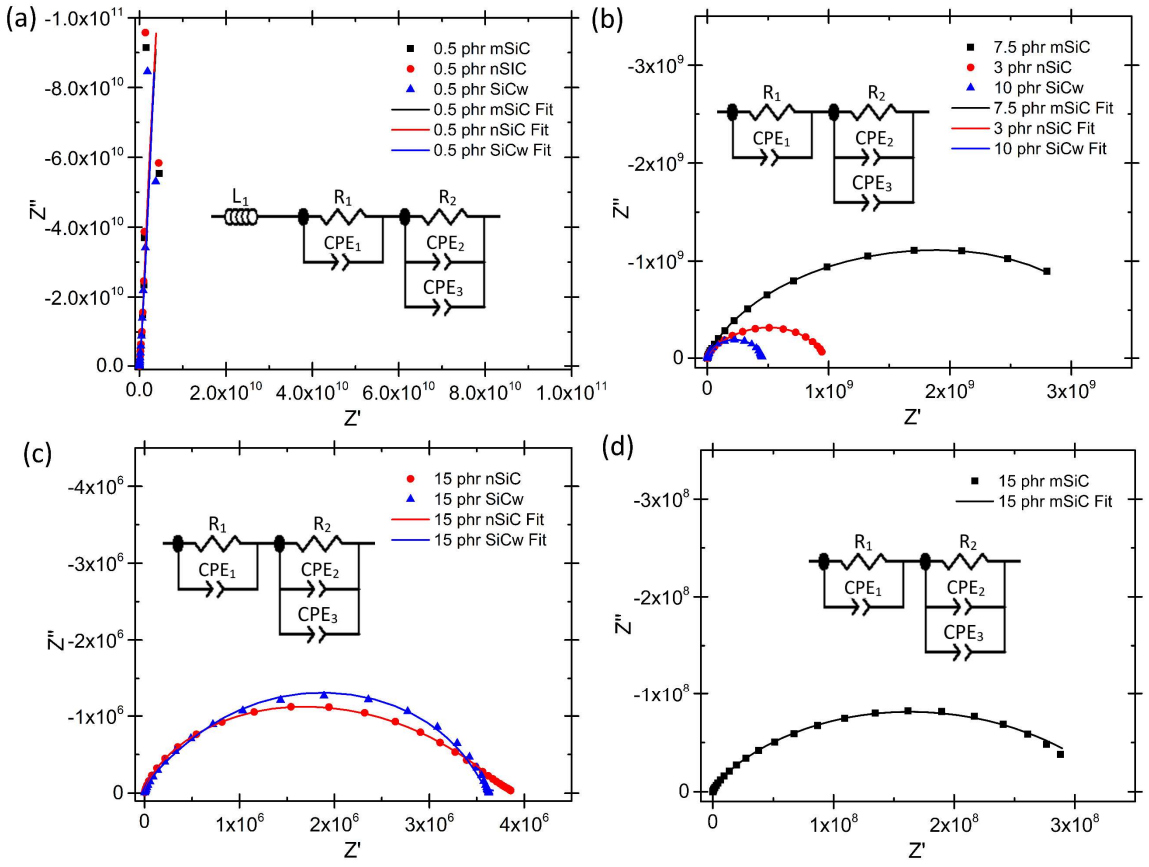

Figure 84 – SiC/PMMA composite equivalent circuit fits from (a) below percolation, (b) near percolation, and (c-d) after percolation for select compositions

9.4 Equivalent Circuit Modeling of the Effect of Particle Size on Electrical Properties (SiC/Glass)

The whisker SiC/PMMA composite equivalent circuit values are shown in Table 20. As concentration increases, resistance decreases (R_1 and R_2), CPE-T increases in all cases,

and CPE_1-P and CPE_3-P increase while CPE_2-P decreases. Since no circuit fit value stays steady with increasing concentration, it is likely that the same phenomena occurred as with the SiC_w/PMMA where the SiC_w length is closer in size to the glass. The SiC_w/glass composites shift between five circuits as concentrations increase. This may be due to the glass being monodispersed (50 μm) rather than polydisperse like the PMMA (10-100 μm). The polydisperse PMMA has a better packing factor than monodisperse glass, and therefore the segregation of the filler to the boundaries of the monodisperse glass is easier than in PMMA. This allows for the filler to be the more dominant factor in determination of the electrical properties which results in more sensitivity to the path formation of the SiC and more equivalent circuits to model the changes.

Table 20 – Equivalent circuit fit values for whisker SiC / borosilicate glass composites (averages of at least 3 samples with ± standard deviation)

phr	Circuit	L_1 (lH)	R_1 (Ω)	CPE_1-T (F)	CPE_1-P (F)	CPE_2-T (F)	CPE_2-P (F)	R_2 (Ω)	CPE_3-T (F)	CPE_3-P (F)	CPE_4-T (F)	CPE_4-P (F)
0.01	a	1.36×10^{-4} ±8.32×10^{-6}	$1.00 \times 10^{+20}$ ±0	8.27×10^{-13} ±3.78×10^{-14}	0.536 ±0.003	5.94×10^{-12} ±6.58×10^{-14}	0.994 ±0.000					
0.1	a	1.46×10^{-4} ±1.37×10^{-5}	$1.00 \times 10^{+20}$ ±0	7.54×10^{-13} ±8.04×10^{-14}	0.556 ±0.029	5.46×10^{-12} ±1.39×10^{-13}	0.994 ±0.000					
0.25	a	1.76×10^{-4} ±4.85×10^{-5}	$1.00 \times 10^{+20}$ ±0	7.89×10^{-13} ±4.24×10^{-15}	0.505 ±0.036	5.03×10^{-12} ±7.10×10^{-13}	0.994 ±0.000					
2.5	a	7.92×10^{-5} ±1.95×10^{-5}	$9.84 \times 10^{+19}$ ±$2.32 \times 10^{+18}$	1.73×10^{-12} ±6.31×10^{-13}	0.434 ±0.033	6.90×10^{-12} ±7.38×10^{-13}	0.984 ±0.003					
5	b		$3.28 \times 10^{+9}$ ±$4.45 \times 10^{+9}$	6.12×10^{-10} ±5.76×10^{-10}	0.417 ±0.051	2.27×10^{-11} ±1.02×10^{-11}	0.928 ±0.025		7.89×10^{-8} ±7.79×10^{-8}	0.748 ±0.125		
7.5	c	5.32×10^{-5}	$2.42 \times 10^{+7}$	2.21×10^{-11}	0.989	4.29×10^{-10}	0.798	$1.64 \times 10^{+7}$	9.68×10^{-10}	0.589	3.12×10^{-11}	0.932
7.5	d	1.22×10^{-4}	$2.53 \times 10^{+10}$	1.06×10^{-10}	0.344	1.02×10^{-11}	0.973	$9.49 \times 10^{+7}$	1.35×10^{-10}	0.919		
10	e		$6.79 \times 10^{+9}$ ±$7.54 \times 10^{+9}$	1.60×10^{-11} ±1.30×10^{-12}	0.952 ±0.008	3.99×10^{-10} ±2.97×10^{-10}	0.304 ±0.074					
12.5	d	9.00×10^{-5} ±6.54×10^{-5}	$8.57 \times 10^{+8}$ ±$1.19 \times 10^{+9}$	2.96×10^{-11} ±1.39×10^{-11}	0.920 ±0.015	1.40×10^{-9} ±1.87×10^{-9}	0.505 ±0.070	$3.89 \times 10^{+8}$ ±$5.41 \times 10^{+8}$	5.22×10^{-8} ±7.20×10^{-8}	0.749 ±0.163		

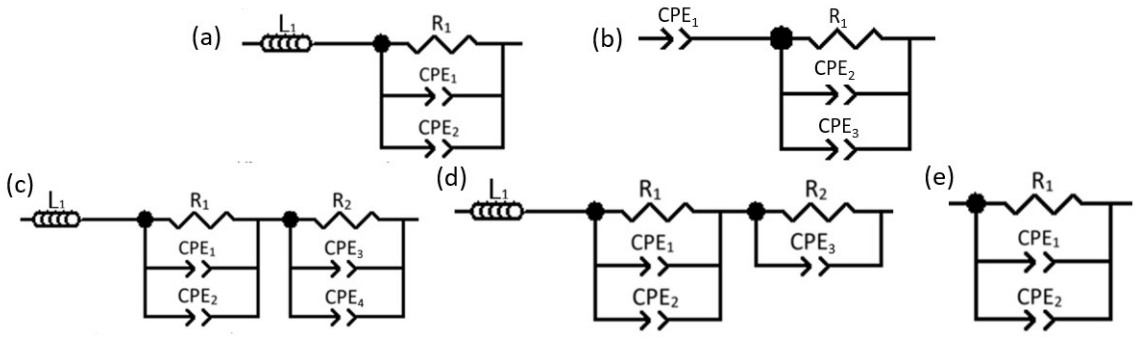

Figure 85 shows the phase angle data and equivalent circuit fits below, at and after percolation of SiC_w/glass composites along with fits for the SiC_w powder. Unlike with the SiC_w/PMMA, there is an inductor within the circuits for most concentrations. This inductance is from the higher concentration of SiC_w.

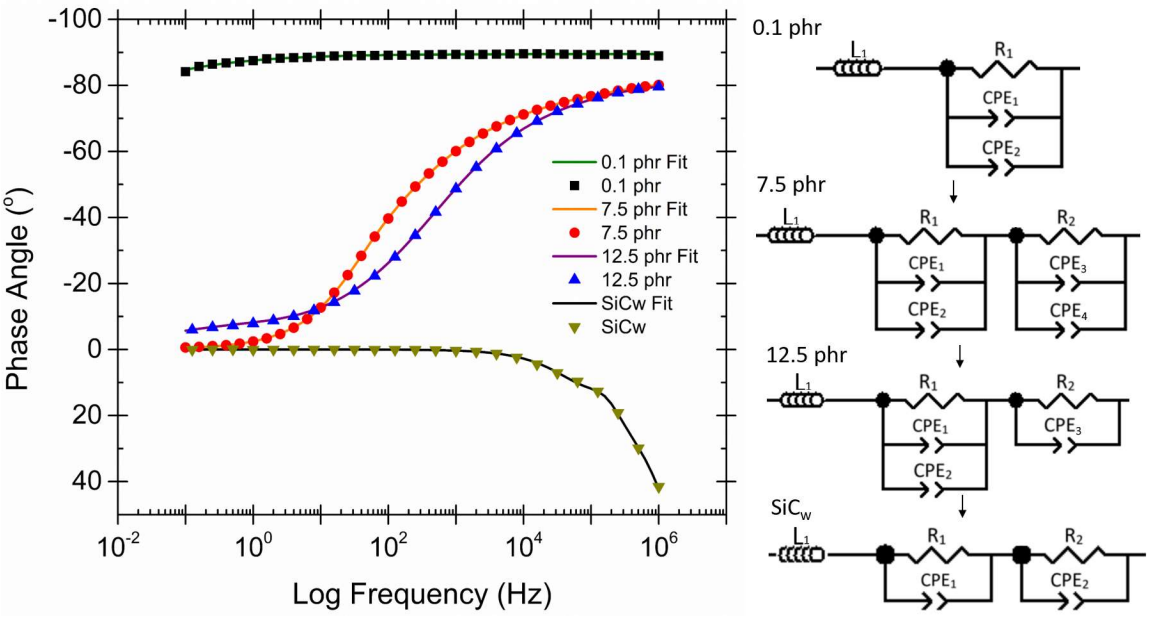

Figure 85 – Phase angle versus frequency for SiC_w/Glass composites and SiC_w powder compressed at 350 MPa

The SiC nanowire /glass composite equivalent circuit values are shown in Table 21. As concentration increases, resistance decreases (R_1 and R_2), CPE_1-T and CPE_4-T remain about the same value, and CPE_2-T increases. The CPE_1-P and CPE_2-P values seem to increase and then decrease, while CPE_3-P does the opposite; it decreases and then increases. Since the SiC nanowires are much smaller than the whiskers, the glass properties show more in the circuit values. CPE_1-T (~10^{-10} F) and CPE_4-T (~10^{-12} F) both have values that correlate to the glass CPE fitting values (Figure 81).

Table 21 – Equivalent circuit fit values for SiC nanowire / borosilicate glass composites (averages of at least 3 samples with ± standard deviation)

phr	Circuit	R_1 (Ω)	CPE_1-T (F)	CPE_1-P (F)	CPE_2-T (F)	CPE_2-P (F)	R_2 (Ω)	CPE_3-T (F)	CPE_3-P (F)	CPE_4-T (F)	CPE_4-P (F)
0	a	6.94×10^{19} ±5.31×10^{19}	1.03×10^{-10} ±1.16×10^{-10}	0.511 ±0.334			3.87×10^{12} ±2.28×10^{12}	1.49×10^{-12} ±3.13×10^{-13}	0.642 ±0.076	5.27×10^{-12} ±2.65×10^{-13}	0.995 ±0
0.01	a	7.55×10^{16} ±1.31×10^{17}	7.28×10^{-11} ±8.35×10^{-11}	0.981 ±0.036			3.46×10^{19} ±5.67×10^{19}	6.78×10^{-12} ±4.74×10^{-13}	0.995 ±0.003	3.27×10^{-11} ±5.12×10^{-11}	0.507 ±0.048
0.05	a	4.41×10^{11} ±4.10×10^{11}	1.68×10^{-11} ±3.91×10^{-12}	0.967 ±0.024			1.00×10^{20} ±0	7.57×10^{-12} ±2.39×10^{-12}	1.019 ±0.023	2.06×10^{-11} ±1.60×10^{-11}	0.498 ±0.025
0.1	a	2.07×10^{11} ±1.13×10^{11}	2.77×10^{-11} ±5.35×10^{-12}	0.970 ±0.026			7.93×10^{19} ±3.58×10^{19}	6.78×10^{-12} ±1.14×10^{-12}	1.008 ±0.014	6.40×10^{-12} ±6.83×10^{-12}	0.632 ±0.216
0.325	a	1.97×10^{11} ±2.48×10^{11}	3.40×10^{-11} ±2.61×10^{-11}	0.997 ±0.062			6.69×10^{19} ±5.73×10^{19}	6.44×10^{-12} ±1.15×10^{-12}	1.006 ±0.025	4.23×10^{-11} ±2.91×10^{-11}	0.346 ±0.072
0.5	a	4.05×10^{10} ±4.03×10^{10}	6.65×10^{-11} ±1.00×10^{-11}	0.955 ±0.040			1.00×10^{20} ±0	5.89×10^{-12} ±5.25×10^{-13}	1.002 ±0.011	2.71×10^{-11} ±1.50×10^{-11}	0.422 ±0.003
0.5	b	2.81×10^{9}	3.56×10^{-12}	1.06	1.70×10^{-10}	0.308	4.75×10^{10}	1.14×10^{-11}	0.960	4.75×10^{-11}	0.669
1	a	2.08×10^{9} ±2.91×10^{9}	2.26×10^{-10} ±1.46×10^{-10}	0.831 ±0.001			2.35×10^{9} ±3.12×10^{9}	8.08×10^{-10} ±8.05×10^{-10}	0.359 ±0.001	2.91×10^{-12} ±9.75×10^{-13}	1.043 ±0.015
1	b	2.53×10^{7}	4.30×10^{-12}	1.030	1.21×10^{-9}	0.470	1.00×10^{20}	1.72×10^{-10}	0.861	5.25×10^{-10}	0.095
1.5	a	2.01×10^{9} ±1.47×10^{9}	1.56×10^{-10} ±5.50×10^{-11}	0.843 ±0.012			1.95×10^{9} ±1.00×10^{9}	4.17×10^{-10} ±8.37×10^{-11}	0.261 ±0.046	3.31×10^{-12} ±1.61×10^{-13}	1.02 ±0.007
3	a	8.84×10^{8} ±7.61×10^{8}	3.77×10^{-10} ±1.49×10^{-10}	0.846 ±0.010			2.05×10^{9} ±1.16×10^{9}	4.12×10^{-10} ±1.05×10^{-10}	0.302 ±0.052	5.19×10^{-12} ±5.02×10^{-13}	1.01 ±0.009
4	a	9.00×10^{8} ±8.70×10^{8}	2.98×10^{-10} ±3.67×10^{-11}	0.846 ±0.017			3.39×10^{9} ±4.40×10^{9}	1.23×10^{-9} ±3.89×10^{-10}	0.274 ±0.086	6.48×10^{-12} ±1.42×10^{-12}	1.01 ±0.038

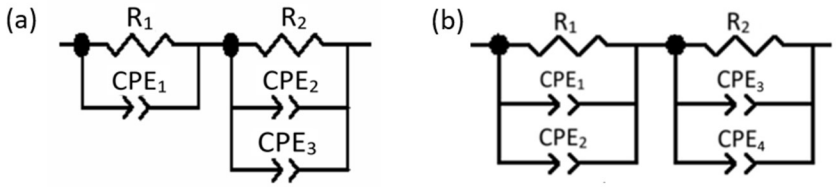

Figure 86 summarizes the change in equivalent circuit fits with increasing concentration for select SiC_w and SiC_{nw} / glass composites. While the trend starts out as the same as the SiC_w/glass with reducing the size of a semicircle (decreasing resistance), it then continues to form a distorted semicircle at the highest concentrations made. These distortions are a representation of a second semicircle (second RC in parallel) showing in the complex impedance graph. Prior to that point, the first semicircle was large enough to obscure the second semicircle. The circuits have multiple resistors and CPEs in parallel

with each other, this indicates multiple semicircles should show within the complex impedance. However, the values of the circuit elements determine if they are visible in relation to each other. Once the conductivity increased, the other elements were no longer obscured by the larger values of the first RC. This is seen in the distorted semicircles in Figure 86 d and e.

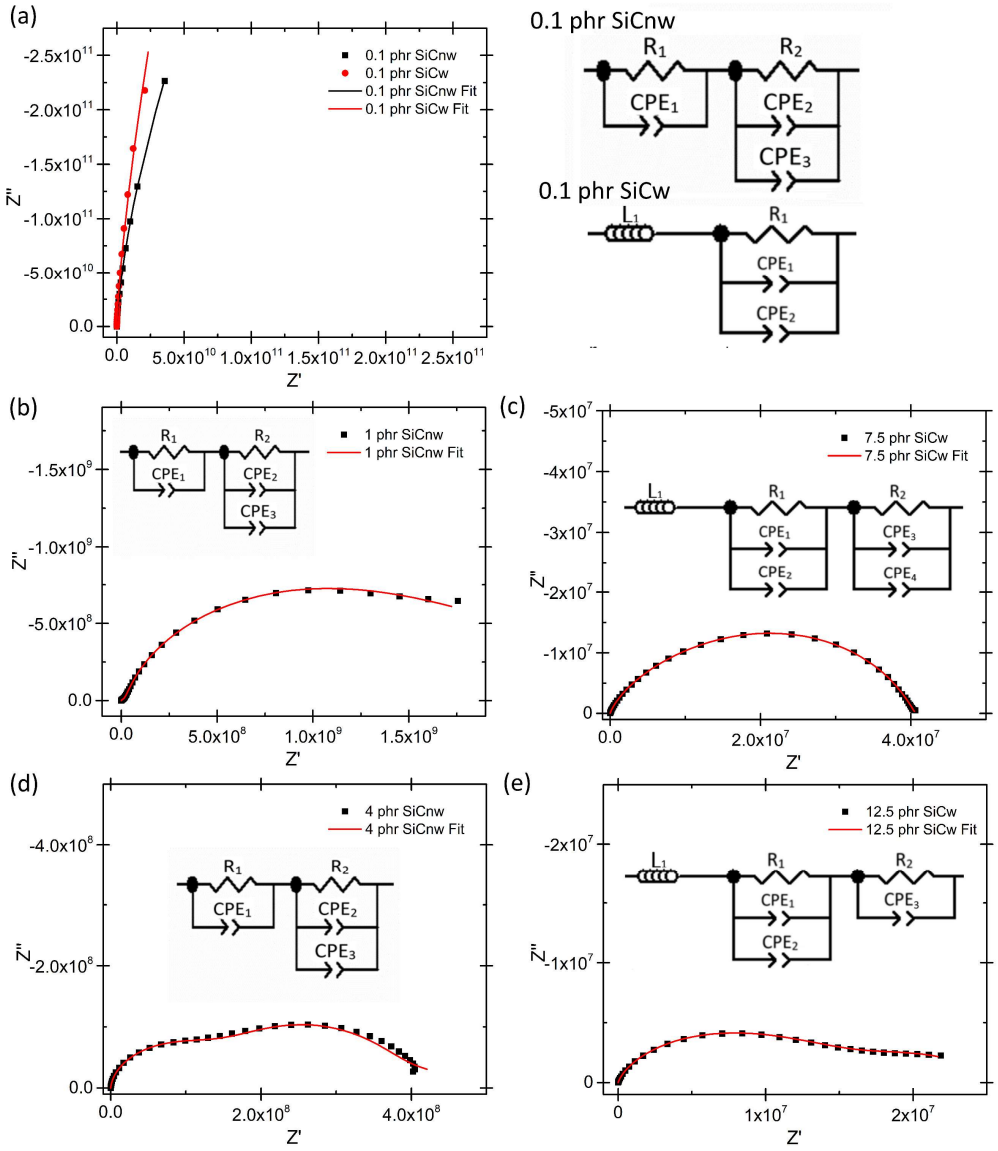

Figure 86 – Complex Impedance and equivalent circuit fit of select SiC_{nw} and SiC_{w} / glass composites at (a) below percolation, (b-c) about percolation, and (d-e) after percolation

9.5 Equivalent Circuit Modeling of the Effect of Humidity on Electrical Properties (SiC_w/Glass)

Table 22 shows the equivalent circuit values of SiC_w/glass composites as they change with increasing humidity. Overall, the equivalent circuits become more complex with increasing circuit elements as both the humidity and the concentration increase. As humidity increases for 0.01 – 7.5 phr, resistance decreases and CPE_1-T increases. For the lower concentrations (0.01 and 0.25 phr), CPE_1-P increases and CPE_2-P decreases with increases in humidity. At 2.5 and 7.5 phr, other than CPE_1-T, there is little change for the CPE values with changing humidity. Lastly, at 12.5 phr the only values that exhibit significant change are R_2, CPE_4-T, and CPE_4-P. Both R_2 and CPE_4-T increase while CPE_4-P decreases. The absorption of water into the glass composites is the reason for all of these changes. At low concentrations, the water particles carry the charge. As the concentration increases, the SiC_w increasingly contribute to the overall conductivity. At 12.5 phr, the water particles appear to increase the natural resistance of the composite rather than increase it [66, 97]. At that stage, the water instead takes away the charge from the SiC_w paths.

Table 22 – Equivalent circuit fit values and circuits for select whisker SiC / borosilicate glass composites at 10-60% humidity (averages of at least 3 samples with ± std. dev.)

Humidity	L_1 (lH)	R_1 (Ω)	CPE_1-T (F)	CPE_1-P (F)	CPE_2-T (F)	CPE_2-P (F)		R_2 (Ω)	CPE_3-T (F)	CPE_3-P (F)	CPE_4-T (F)	CPE_4-P (F)
0.01 phr												
10	1.37 x 10^{-4} ±1.07 x 10^{-5}	9.76 x 10^{+12} ±9.38 x 10^{+11}	7.63 x 10^{-13} ±7.98 x 10^{-14}	0.597 ±0.018	5.76 x 10^{-12} ±1.23 x 10^{-13}	0.995 ±0.000	a					
20	1.42 x 10^{-4} ±8.73 x 10^{-6}	7.86 x 10^{+12} ±1.24 x 10^{+12}	7.95 x 10^{-13} ±1.37 x 10^{-13}	0.613 ±0.011	5.68 x 10^{-12} ±1.62 x 10^{-13}	0.995 ±0.000	a					
30	1.46 x 10^{-4} ±6.05 x 10^{-6}	3.53 x 10^{+12} ±3.20 x 10^{+11}	1.01 x 10^{-12} ±2.26 x 10^{-13}	0.560 ±0.051	5.70 x 10^{-12} ±1.80 x 10^{-13}	0.994 ±0.000	a					
40	9.29 x 10^{-5} ±3.37 x 10^{-5}	6.22 x 10^{+11} ±7.24 x 10^{+11}	4.23 x 10^{-12} ±4.47 x 10^{-12}	0.609 ±0.065	5.70 x 10^{-12} ±2.96 x 10^{-13}	0.997 ±0.002	a					
45	1.38 x 10^{-4}	5.57 x 10^{+10}	1.68 x 10^{-12}	0.612	6.02 x 10^{-12}	0.994	a					
50		5.94 x 10^{+9}	1.43 x 10^{-11}	0.636	4.86 x 10^{-12}	1.01	b					
60		6.28 x 10^{+8}	4.59 x 10^{-12}	1.01	2.30 x 10^{-11}	0.648	b					
60	2.63 x 10^{-4}	2.64 x 10^{+8}	6.56 x 10^{-12}	0.983			c					
0.25 phr												
10	1.62 x 10^{-4} ±3.65 x 10^{-5}	1.26 x 10^{+13} ±7.81 x 10^{+12}	7.43 x 10^{-13} ±3.56 x 10^{-14}	0.571 ±0.007	4.99 x 10^{-12} ±7.29 x 10^{-13}	0.994 0.000	a					
20	1.73 x 10^{-4} ±3.81 x 10^{-5}	3.58 x 10^{+12} ±2.80 x 10^{+12}	3.30 x 10^{-12} ±3.15 x 10^{-12}	0.743 ±0.355	2.76 x 10^{-12} ±2.60 x 10^{-12}	0.781 0.302	a					
30	1.64 x 10^{-4} ±5.95 x 10^{-6}	1.23 x 10^{+13} ±1.44 x 10^{+13}	5.05 x 10^{-12} ±8.08 x 10^{-13}	0.994 ±0.001	8.34 x 10^{-12} ±8.69 x 10^{-12}	0.340 0.082	a					
40		2.63 x 10^{+10} ±1.76 x 10^{+10}	4.65 x 10^{-12} ±8.54 x 10^{-13}	1.00 ±0.003	1.81 x 10^{-11} ±8.66 x 10^{-12}	0.488 0.036	b					
50		1.28 x 10^{+9}	4.36 x 10^{-12}	1.01	2.98 x 10^{-11}	0.631	b					
50		5.76 x 10^{+8}	4.16 x 10^{-12}	1.02	6.32 x 10^{-11}	0.467		4.27 x 10^{+8}	4.93 x 10^{-11}	0.921		d
60		1.42 x 10^{+8} ±8.59 x 10^{+7}	2.31 x 10^{-12} ±2.98 x 10^{-13}	1.10 ±0.001	8.78 x 10^{-11} ±3.47 x 10^{-11}	0.653 ±0.022		8.13 x 10^{+7} ±8.36 x 10^{+7}	3.10 x 10^{-11} ±6.99 x 10^{-12}	0.915 ±0.005		d
2.5 phr												
10	7.92 x 10^{-5} ±1.95 x 10^{-5}	1.00 x 10^{+20} ±0	1.73 x 10^{-12} ±6.31 x 10^{-13}	0.434 ±0.033	6.90 x 10^{-12} ±7.38 x 10^{-13}	0.984 ±0.003	a					
20	8.33 x 10^{-5} ±2.99 x 10^{-5}	1.00 x 10^{+20} ±0	5.88 x 10^{-12} ±4.20 x 10^{-12}	0.479 ±0.047	6.89 x 10^{-12} ±8.20 x 10^{-13}	0.984 ±0.003	a					
30	9.90 x 10^{-5}	1.00 x 10^{+20}	7.42 x 10^{-12}	0.544	7.35 x 10^{-12}	0.982	a					
30		8.23 x 10^{+19}	3.08 x 10^{-11}	0.476	6.04 x 10^{-12}	0.989	b					
40	1.54 x 10^{-4} ±1.06 x 10^{-5}	8.47 x 10^{+10} ±1.05 x 10^{+11}	7.78 x 10^{-11} ±4.80 x 10^{-11}	0.510 ±0.065	6.90 x 10^{-12} ±1.41 x 10^{-12}	1.005 ±0.006		1.79 x 10^{+10} ±1.59 x 10^{+10}	1.79 x 10^{-10} ±1.92 x 10^{-10}	0.891 ±0.052		e
50	1.50 x 10^{-4} ±2.14 x 10^{-5}	4.84 x 10^{+9} ±2.61 x 10^{+9}	1.72 x 10^{-10} ±1.50 x 10^{-10}	0.535 ±0.110	6.03 x 10^{-12} ±1.82 x 10^{-13}	1.011 ±0.013		1.02 x 10^{+9} ±1.41 x 10^{+9}	1.23 x 10^{-10} ±7.56 x 10^{-11}	0.891 ±0.019		e
60	1.59 x 10^{-4}	7.79 x 10^{+8}	5.44 x 10^{-10}	0.447	5.75 x 10^{-12}	1.004		1.11 x 10^{+7}	2.00 x 10^{-10}	0.869		e
7.5 phr												
10	8.69 x 10^{-5} ±4.94 x 10^{-5}	1.26 x 10^{+10} ±1.78 x 10^{+10}	4.57 x 10^{-10} ±4.97 x 10^{-10}	0.475 ±0.185	1.60 x 10^{-11} ±8.27 x 10^{-12}	0.962 ±0.016		5.61 x 10^{+7} ±5.50 x 10^{+7}	3.07 x 10^{-10} ±2.42 x 10^{-10}	0.881 ±0.054		e f
20	6.35 x 10^{-5}	2.43 x 10^{+7}	1.97 x 10^{-11}	0.942	6.34 x 10^{-10}	0.628		1.07 x 10^{+7}	7.31 x 10^{-8}	0.295	1.12 x 10^{-10}	1.01
20	1.36 x 10^{-4}	9.36 x 10^{+8}	8.02 x 10^{-10}	0.401	7.94 x 10^{-10}	0.991		3.55 x 10^{+6}	3.01 x 10^{-10}	0.857	e	f
30	5.83 x 10^{-5}	9.56 x 10^{+6}	3.35 x 10^{-11}	0.930	2.54 x 10^{-9}	0.527		1.70 x 10^{+7}	6.82 x 10^{-8}	0.210	1.30 x 10^{-10}	0.911
30	1.26 x 10^{-4}	1.68 x 10^{+8}	2.29 x 10^{-9}	0.369	7.29 x 10^{-12}	0.986		5.01 x 10^{+3}	1.29 x 10^{-8}	0.709	e	
40	9.80 x 10^{-5} ±8.90 x 10^{-5}	2.37 x 10^{+7} ±2.33 x 10^{+7}	2.74 x 10^{-8} ±2.66 x 10^{-8}	0.299 ±0.063	3.02 x 10^{-11} ±3.18 x 10^{-11}	0.937 ±0.065		1.17 x 10^{+6} ±8.85 x 10^{+5}	4.03 x 10^{-9} ±2.02 x 10^{-10}	0.789 ±0.024	e	
50		6.00 x 10^{+5}	8.72 x 10^{-11}	0.859	2.92 x 10^{-7}	0.223					b	
50	1.20 x 10^{-4}	1.36 x 10^{+7}	1.50 x 10^{-8}	0.330	7.91 x 10^{-12}	0.981		6.23 x 10^{+5}	5.31 x 10^{-9}	0.778	e	
60		5.89 x 10^{+5}	3.62 x 10^{-6}	0.103	4.14 x 10^{-9}	0.690		4.03 x 10^{+4}	2.07 x 10^{-10}	0.840	d	
60	9.88 x 10^{-5}	4.74 x 10^{+6}	2.95 x 10^{-8}	0.324	7.90 x 10^{-12}	0.981		2.54 x 10^{+5}	5.58 x 10^{-9}	0.760	e	
12.5 phr												
10	9.00 x 10^{-5} ±6.54 x 10^{-5}	8.57 x 10^{+8} ±1.19 x 10^{+9}	2.96 x 10^{-11} ±1.39 x 10^{-11}	0.920 ±0.015	1.40 x 10^{-9} ±1.87 x 10^{-9}	0.505 ±0.070		3.89 x 10^{+8} ±5.41 x 10^{+8}	5.23 x 10^{-8} ±7.21 x 10^{-8}	0.749 ±0.163	e	f
20	7.27 x 10^{-5} ±2.76 x 10^{-5}	5.00 x 10^{+19} ±7.07 x 10^{+19}	3.72 x 10^{-10} ±4.97 x 10^{-10}	0.980 ±0.004	1.13 x 10^{-8} ±1.15 x 10^{-8}	0.339 ±0.200		5.70 x 10^{+7} ±6.48 x 10^{+7}	4.56 x 10^{-8} ±6.44 x 10^{-8}	0.642 ±0.405	4.89 x 10^{-10} ±3.95 x 10^{-10}	0.618 ±0.332
30	5.36 x 10^{-5} ±2.89 x 10^{-5}	1.46 x 10^{+7} ±1.45 x 10^{+7}	1.96 x 10^{-11} ±3.68 x 10^{-12}	0.944 ±0.004	8.48 x 10^{-9} ±3.20 x 10^{-9}	0.370 ±0.122		2.68 x 10^{+6} ±4.63 x 10^{+5}	1.84 x 10^{-7} ±2.51 x 10^{-8}	0.555 ±0.027	e	f
40	6.73 x 10^{-5} ±1.65 x 10^{-5}	3.64 x 10^{+6} ±4.57 x 10^{+6}	1.43 x 10^{-11} ±1.45 x 10^{-12}	0.970 ±0.028	8.16 x 10^{-9} ±3.91 x 10^{-9}	0.436 ±0.156		6.79 x 10^{+14} ±9.60 x 10^{+14}	8.11 x 10^{-8} ±1.06 x 10^{-7}	0.867 ±0.188	1.64 x 10^{-7} ±2.31 x 10^{-7}	0.477 ±0.530
50	7.74 x 10^{-5} ±3.56 x 10^{-5}	3.64 x 10^{+6} ±2.56 x 10^{+6}	1.53 x 10^{-11} ±2.01 x 10^{-12}	0.955 ±0.000	6.23 x 10^{+7} ±8.81 x 10^{+7}	0.412 ±0.094		1.00 x 10^{+20} ±0	4.38 x 10^{-8} ±5.29 x 10^{-8}	0.769 ±0.048	2.50 x 10^{-6} ±2.50 x 10^{-6}	0.120 ±0.031
60	6.66 x 10^{-5} ±2.69 x 10^{-5}	5.79 x 10^{+5} ±1.86 x 10^{+5}	1.33 x 10^{-11} ±4.60 x 10^{-12}	0.965 ±0.013	1.51 x 10^{-8} ±1.77 x 10^{-9}	0.434 ±0.047		5.54 x 10^{+19} ±8.53 x 10^{+18}	4.28 x 10^{-8} ±5.20 x 10^{-8}	0.787 ±0.071	3.44 x 10^{-6} ±2.89 x 10^{-6}	0.116 ±0.042

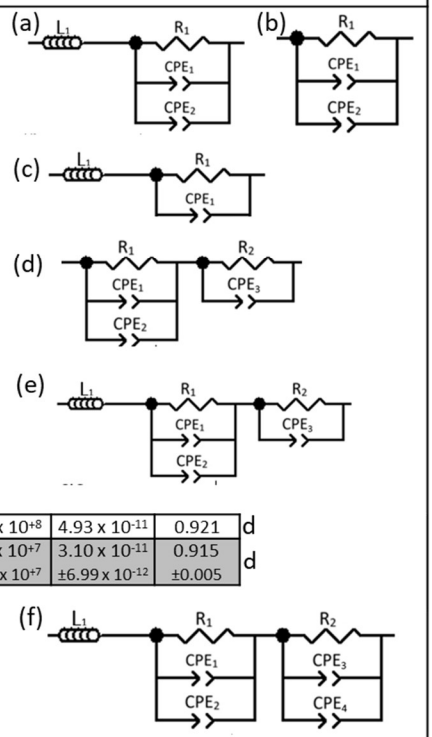

Figure 87 shows the complex modulus graphs and fits of SiC_w/glass at 10% and 60% humidity. The increase in humidity increases the conductivity of 0.1, 0.25, and 2.5 phr composites so that the modulus forms a semicircle where there was only the start of one before (Figure 87 a, b, and c). The humidity increase for 7.5 and 12.5 phr causes the semicircles to change from deformed to more even, indicating that one process related to the humidity dominated over the others (Figure 87 d and c). Figure 87 also contains the circuits for each fit to show the progression with the representative graphs.

Figure 88 contains select graphs of normalized Z", M", and tanδ versus log frequency of the experimental data and equivalent circuit fits for SiC_w/glass at 10% and 60% humidity. These graphs are from the same experimental data as Figure 73 and Figure 74. The normalized fit data also align with the normalized data.

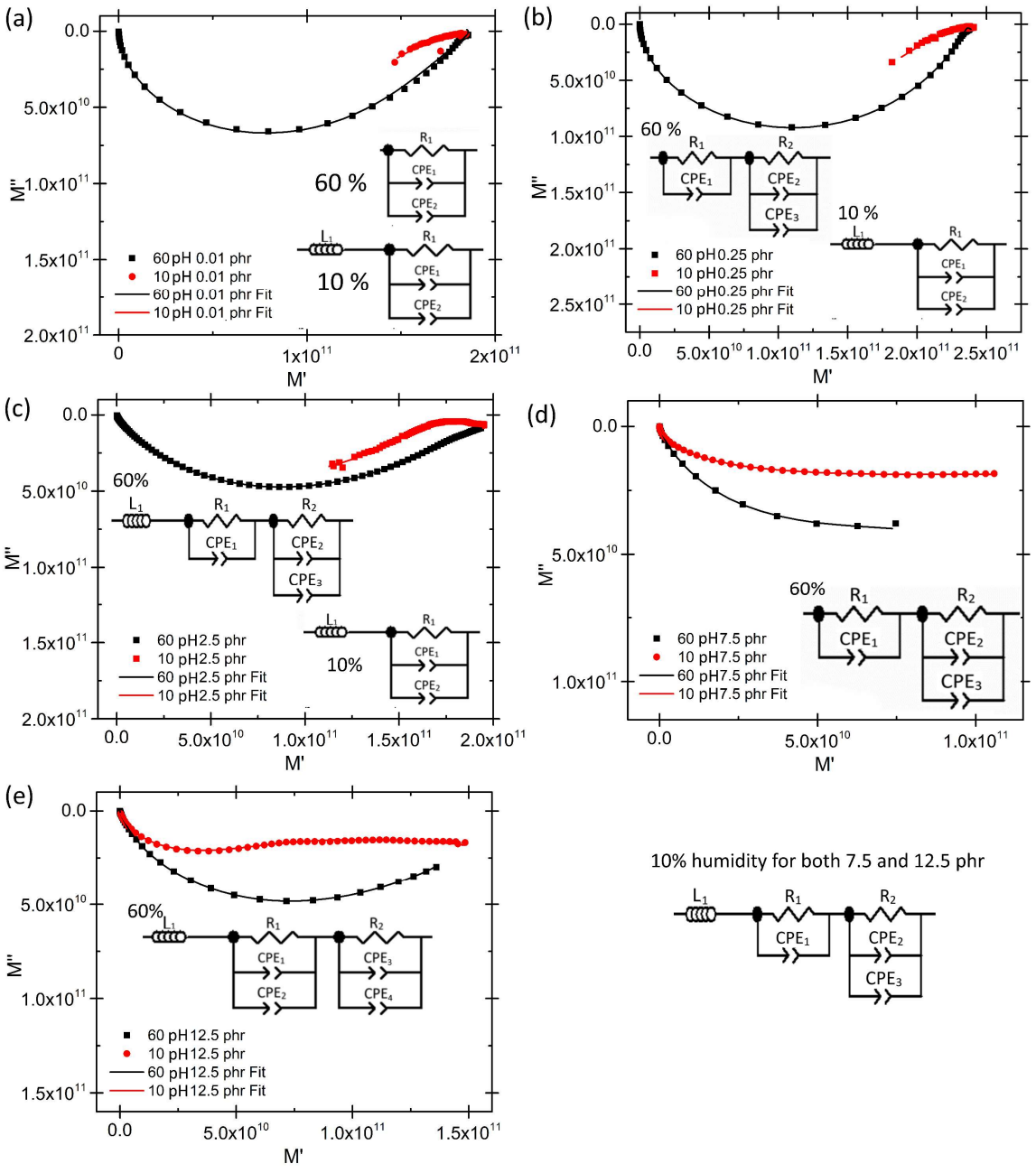

Figure 87 – Complex modulus and equivalent circuit fit of SiC_w / glass composites at (a) 0.01 phr, (b) 0.25 phr, (c) 2.5 phr, (d) 7.5 phr, (e) and 12.5 phr for 10% and 60% humidity

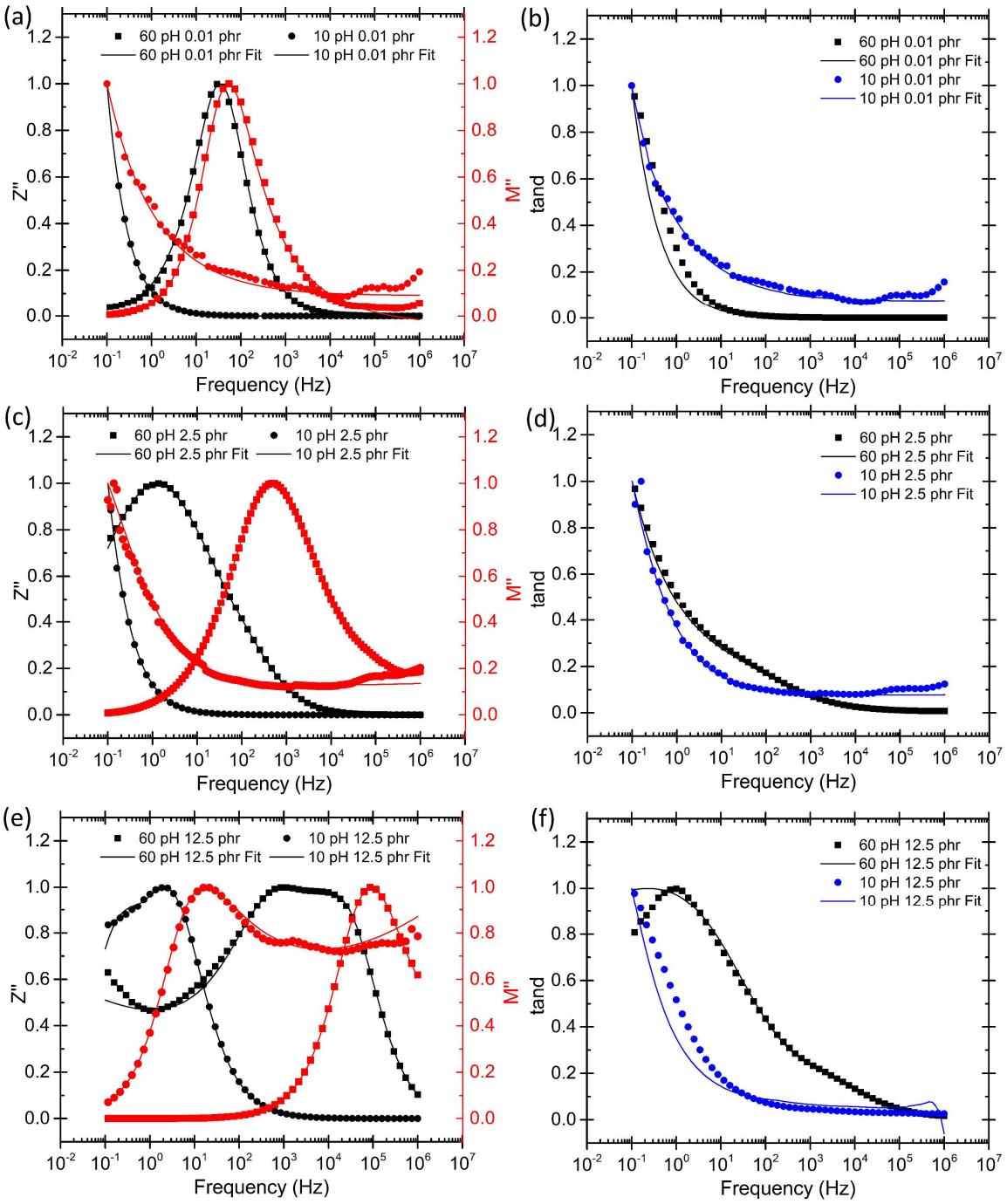

Figure 88 – Normalized impedance, modulus, and tanδ with equivalent circuit fittings of SiC_w / glass composites at (a-b) 0.01 phr, (c-d) 2.5 phr, and (e-f) 12.5 phr for 10% and 60% humidity

9.6 Summary

The impedance spectroscopy data presented in Chapters 4-8 were fit to equivalent circuits. This analysis first fit circuits to the base materials first (MWCNT, SiC, PMMA, and glass). From the base material analysis, circuit fit values from the base materials can be identified within the composite materials. The overall conductivity is determined by the interactions between the filler and matrix materials. This means that changing the processing, filler shape, and filler size all change the circuits and circuit values that represent the composites.

When comparing three different mixing methods for MWCNT/PMMA composites, the equivalent circuit is the same before percolation occurs. After percolation, the circuits are similar but vary more depending on the microstructure and particle interactions. The melt mixed composites have different circuits than the solution and mechanically mixed composites. This is most likely caused by the PMMA having a stronger effect on the electrical properties due to the MWCNT being more evenly distributed. All three types did have the trend from capacitive behavior to more inductive behavior as MWCNT concentration increases.

The difference in particle shape also showed a difference in the circuit values of the SiC/PMMA composites. Since all three were mechanically mixed, it is not surprising that they had the same circuits representing them. There is a difference in the values within the circuits. Both micron- and nano- SiC showed a CPE value that correlated with the CPE of PMMA at all concentrations, indicating that the PMMA still played a strong role in disrupting the conductive particle paths. On the other hand, the same CPE for the SiC_w had

an increase. This is likely because the length of the SiC_w was closer in size to the PMMA particles.

The length of the SiC_w also had the same effect on the SiC_w/glass composites that it did on the SiC/PMMA composites. With the SiC_w/glass, there were no circuit elements that did not change with increasing concentration. It also required five different circuits to show the changing concentration rather than the two circuits developed for SiC_w/PMMA. This is likely due to the glass being monodisperse (50 μm) rather than polydisperse like the PMMA (10- 100 μm). The glass allows the SiC to fit into the boundaries of the glass particles more easily due to the lower packing factor. The SiC_{nw}/glass composites showed two steady circuit elements with values corresponding to that of the glass circuit values, and it only had two circuits to represent the change in concentration. Its smaller size (~32 nm) let it segregate to the grain-like boundaries of the glass particles with less difficulty than the SiC_w (1 μm).

Lastly, humidity at the time of measurement plays a large role in the measured properties of the glass composites. At the lowest concentrations, absorbed water from the atmosphere carries the charge. As the concentration increases, both the filler (SiC_w) and the absorbed water carry the charge. At the highest concentrations, instead of supplementing the conductive paths, it detracts from it and increases the resistance of the composites.

Overall, equivalent circuit fittings successfully broke down the contributions of the individual materials within the composites to the overall electrical properties. It showed this for multiple different composite microstructures and filler morphologies.

10 CONCLUSIONS AND FUTURE WORK

10.1 Conclusions

In this dissertation, MWCNT/PMMA, SiC/PMMA, and SiC/Glass composites were fabricated to study the effect of network formation and particle morphology on the microstructural and electrical properties. The hypothesis of this thesis was that applying equivalent circuit models to the electrical data of the individual materials and the composites would enhance our understanding of conductive filler network formation in insulating matrices using various processing and material types. Applying the equivalent circuit models was hypothesized to show the influence of the individual materials on the overall electrical properties of the composites. Overall, equivalent circuit fittings successfully broke down the contributions of the individual materials within the composites to the overall electrical properties. It showed this for multiple different composite microstructures and filler morphologies.

The MWCNT/PMMA composites were made using three different mixing methods: mechanical, solution, and melt mixing. These mixing methods resulted in segregated network, agglomerated, and distributed microstructures respectively, allowing for the comparison of network formation with three different microstructures. To compare the effect of particle morphology, three types of SiC (micron-sized, nano-sized, and whisker) / PMMA composites were made using mechanical mixing. Lastly, two sizes of anisotropic SiC (whisker and nanowire) were incorporated into glass to make composites to compare the effect of anisotropic filler size. It was demonstrated that the smallest difference in materials and processing may result in very different properties. This study provided direct

comparisons to verify the changes along with equivalent circuit fitting to correlate the contributions of the filler and matrix materials.

For the effect of network formation, the mechanically mixed MWCNT/PMMA resulted in the lowest percolation threshold (0.087 phr) and the closest conductivity value to the value of compressed MWCNT powder. Optical microscopy, SEM and TEM revealed that the mechanically mixed samples had the MWCNT segregated to the boundaries. The melt mixed had both agglomerates and distributed MWCNTs, and solution mixed samples had agglomerates with a lack of MWCNT in the surrounding area of each. The SAXS results confirm that the MWCNT in all cases remain unaffected in wall thickness and diameter by the processing method. The equivalent circuit fitting showed that at compositions before percolation, the same equivalent circuit applies to all composites. After percolation, the circuits varied with the processing method but were overall very similar. The melt mixed samples had the largest number of different circuits which was likely due to PMMA having a stronger effect due to the dispersal of MWCNT. All three types did show the change from capacitive behavior to more inductive behavior as MWCNT concentration increases.

For the effect of particle morphology, the nano-SiC/PMMA composite formed the most defined segregated network composite, with the most stable results and highest conductivity, and a low percolation threshold of 2.35 phr, while the whisker SiC/PMMA composites had a high percolation threshold of 9.8 phr. The length of SiC_w was close in size to the size of the PMMA powder, which may have led to difficulty with segregating to the boundaries of the PMMA. This also was seen from the values of the equivalent circuits. The micron-sized SiC/PMMA composites had results that were not very

reproducible. Both micron- and nano- SiC composites have CPE values that correlate to PMMA circuit values, but whisker SiC composites have that same CPE increase with concentration. Therefore, the size of the SiC_w in relation to the PMMA may have interfered with the PMMA particles more than the others by reducing the ability of the SiC_w to fit into the boundaries of the PMMA particles. Overall, the SiC/PMMA composites were all represented by the same circuits because they are the same type of material and processing but slightly different circuit element values.

For the effect of anisotropic particle size, whisker and nanowire SiC / borosilicate glass composites were made using SPS. It was theorized that the smaller size of the nanowire would allow it to segregate into the grain boundaries easier and create a lower percolation threshold due to the added length aiding the chance of making network connections. This case proved true in that the SiC_{nw}/glass composites did have a lower percolation threshold (1 phr) than SiC_w/glass composites (5 phr). However, the maximum conductivity value achieved was lower, and samples became too fragile to continue increasing the concentration. For the circuit fitting, the SiC_w/glass composites required five different circuits to represent them with increasing concentrations. The increase in the number of equivalent circuits is likely due to a combination of monodisperse glass and the length of the SiC_w, as compared to the polydisperse PMMA. Conversely the SiC_{nw}/glass composites required only two circuits to represent their electrical properties during the change in concentration and had two CPE values correspond to the contribution of the glass.

During the course of this study, it was discovered that the SiC/glass samples had a strong sensitivity to the humidity at the time of testing, whereas PMMA composites were

unaffected by the humidity. From 0-2.5 phr, the conductivity of the SiC_w/glass composites increases with increasing humidity. For 7.5 and 12.5 phr, there is an initial sharp increase then a gradual decrease in conductivity with increasing humidity. For better understanding of the mechanism of conduction with both water and SiC contributing, normalized M" and Z" were plotted together. The separate M" and Z" peaks indicated both localized and long-range conductivity.

10.2 Suggested Future Work

An interesting continuation of this dissertation would be to create SiC nanowire /PMMA composites to compare them to the other three SiC/PMMA composites. This would verify if the nanowire composites would be comparable to the nano-SiC composites. Theoretically, they should be better than nano-SiC/PMMA composites due to their anisotropy.

The SiC_{nw}/glass composites were very fragile after percolation. While the hold temperature of 610°C worked perfectly for SiC_w/glass, it may not be optimal for the SiC_{nw}/glass composites. A single sample at a higher temperature did not appear to give better results or make it less fragile, but a more thorough study may reveal a better temperature to sinter them at.

Some optimization of the SiC_{nw} conversion from MWCNT was done since the original study that created the SiC nanowire did not provide amounts of precursors. The best yield achieved was less than 0.5 grams per run with some powder needing to be run a

second time because of obvious untransformed MWCNT. The gas flow would also need to be optimized during this. If the gas flow was run too high, the closest MWCNT to the entry point would not transform.

The SiC composites may be used in microwave applications due to their high dielectric loss factor and thermal conductivity, which allows them to heat rapidly. While their electrical conductivity ($\sim 10^{-9}$ $(\Omega\text{-cm})^{-1}$) is low in the composites of this thesis, they may be able to be used in electrical dissipation. If the SiC_{nw} composites are studied and optimized as described before, it may be able to achieve higher electrical conductivity.

The high conductivity of the MWCNT/PMMA composites allows them to be used in different applications. Specifically, the criterion for EMI shielding is fulfilled ($\sigma_{dc} > 10^{-1}$ $(\Omega\text{-cm})^{-1}$ [55]) by the MWCNT/PMMA composites of all mixing methods. The knowledge of the three mixing methods effect on the microstructural and electrical properties allows for tailored selection of the fabrication for specific applications. A future study into the mechanical properties would also be useful. General observations of the mechanical properties of the three mixing methods are that the melt mixed composites are the most difficult to break while the mechanically mixed composites are more easily broken. The mechanically mixed composites fracture along the grain-like boundaries. Therefore, the mechanical properties of a given application also need to be considered.

COMSOL modeling and a percolation model has been applied to ideal segregated network composites using truncated octahedral and truncated tetrahedral shapes for the fillers [59, 60]. This thesis explored the microstructures and electrical properties of agglomerated and distributed network composites in addition to segregated network

composites for anisotropic fillers. Using the electrical and microstructural data from this thesis, COMSOL and percolation models could be created for all three microstructures using anisotropic fillers.

Applying electrical circuits to conductive filler composites may later be done by machine learning. To use machine learning, many different composites using different mixing methods and materials would need to be studied. Using percolation models, an approximate percolation threshold could be determined. From there, composites could be made with compositions around the theoretical percolation threshold. The composites could then be impedance tested (which is non-destructive), then fit to equivalent circuits. Machine learning would reduce the time to fit circuit and reduce human error in determining the values. This would allow for insight into the effect of the fabrication methods and materials used to fabricate the composites accurately and efficiently.

11 REFERENCES

[1] D. Stauffer and A. Aharony, *Introduction to percolation theory*. CRC press, 2018.

[2] M. R. Watt and R. A. Gerhardt, "Factors that Affect Network Formation in Carbon Nanotube Composites and their Resultant Electrical Properties," *Journal of Composites Science,* vol. 4, no. 3, p. 100, 2020.

[3] D. He and N. N. Ekere, "Effect of particle size ratio on the conducting percolation threshold of granular conductive–insulating composites," *Journal of Physics D: Applied Physics,* vol. 37, no. 13, pp. 1848-1852, 2004/06/17 2004.

[4] S. Vionnet-Menot, C. Grimaldi, T. Maeder, S. Strässler, and P. Ryser, "Tunneling-percolation origin of nonuniversality: Theory and experiments," *Physical Review B,* vol. 71, no. 6, p. 064201, 2005.

[5] T. L. Pruyn, "Investigation of percolation in borosilicate glass matrix composites containing conducting segregated networks," Doctor of Philosophy, School of Materials Science and Engineering, Georgia Institute of Technology, 2014.

[6] M. R. Watt and R. A. Gerhardt, "Effect of processing on the properties and morphology of MWCNT-polymer networks," *Materials Research Express,* vol. 7, no. 1, p. 015075, 2020/01/21 2020.

[7] R. Socher, B. Krause, R. Boldt, S. Hermasch, R. Wursche, and P. Pötschke, "Melt mixed nano composites of PA12 with MWNTs: Influence of MWNT and matrix properties on macrodispersion and electrical properties," *Composites Science and Technology,* vol. 71, no. 3, pp. 306-314, 2011/02/07/ 2011.

[8] C. McClory, T. McNally, M. Baxendale, P. Pötschke, W. Blau, and M. Ruether, "Electrical and rheological percolation of PMMA/MWCNT nanocomposites as a function of CNT geometry and functionality," *European Polymer Journal,* vol. 46, no. 5, pp. 854-868, 2010/05/01/ 2010.

[9] L. A. Prystaj, "Effect of carbon filler characteristics on the electrical properties of conductive polymer composites possessing segregated network microstructures," Georgia Institute of Technology, 2008.

[10] R. Ou, S. Gupta, C. A. Parker, and R. A. Gerhardt, "Fabrication and Electrical Conductivity of Poly(methyl methacrylate) (PMMA)/Carbon Black (CB) Composites: Comparison between an Ordered Carbon Black Nanowire-Like Segregated Structure and a Randomly Dispersed Carbon Black Nanostructure," *The Journal of Physical Chemistry B,* vol. 110, no. 45, pp. 22365-22373, 2006/11/01 2006.

[11] A. Janoff and R. Gerhardt, "The Effect of Nanotube Length on the Properties of Segregated Network Composites," in *MRS*, San Francisco, CA, 2015.

[12] M. O. Lisunova, Y. P. Mamunya, N. I. Lebovka, and A. V. Melezhyk, "Percolation behaviour of ultrahigh molecular weight polyethylene/multi-walled carbon nanotubes composites," *European Polymer Journal,* vol. 43, no. 3, pp. 949-958, 2007/03/01/ 2007.

[13] A. Mierczynska, M. Mayne-L'Hermite, G. Boiteux, and J. K. Jeszka, "Electrical and mechanical properties of carbon nanotube/ultrahigh-molecular-weight polyethylene composites prepared by a filler prelocalization method," *Journal of Applied Polymer Science,* vol. 105, no. 1, pp. 158-168, 2007.

[14] F. Du, J. E. Fischer, and K. I. Winey, "Coagulation method for preparing single-walled carbon nanotube/poly(methyl methacrylate) composites and their modulus, electrical conductivity, and thermal stability," *Journal of Polymer Science Part B: Polymer Physics,* vol. 41, no. 24, pp. 3333-3338, 2003.

[15] U. Dettlaff-Weglikowska, M. Kaempgen, B. Hornbostel, V. Skakalova, J. Wang, J. Liang, and S. Roth, "Conducting and transparent SWNT/polymer composites," *physica status solidi (b),* vol. 243, no. 13, pp. 3440-3444, 2006.

[16] S. H. Ryu, H.-B. Cho, J. W. Moon, Y.-T. Kwon, N. S. A. Eom, S. Lee, M. Hussain, and Y.-H. Choa, "Highly conductive polymethly(methacrylate)/multi-wall carbon nanotube composites by modeling a three-dimensional percolated microstructure," *Composites Part A: Applied Science and Manufacturing,* vol. 91, pp. 133-139, 2016/12/01/ 2016.

[17] G. Chen, W. Weng, D. Wu, and C. Wu, "PMMA/graphite nanosheets composite and its conducting properties," *European Polymer Journal,* vol. 39, no. 12, pp. 2329-2335, 2003/12/01/ 2003.

[18] M. C. Hermant, N. M. B. Smeets, R. C. F. v. Hal, J. Meuldijk, H. P. A. Heuts, B. Klumperman, A. M. v. Herk, and C. E. Koning, "Influence of the molecular weight distribution on the percolation threshold of carbon nanotube – polystyrene composites," (in English), vol. 9, no. 1, p. 022, 2009.

[19] S. H. Ryu, H.-B. Cho, S. Kim, Y.-T. Kwon, J. Lee, K.-R. Park, and Y.-H. Choa, "The effect of polymer particle size on three-dimensional percolation in core-shell networks of PMMA/MWCNTs nanocomposites: Properties and mathematical percolation model," *Composites Science and Technology,* vol. 165, pp. 1-8, 2018/09/08/ 2018.

[20] R. H. Schmidt, I. A. Kinloch, A. N. Burgess, and A. H. Windle, "The Effect of Aggregation on the Electrical Conductivity of Spin-Coated Polymer/Carbon Nanotube Composite Films," *Langmuir,* vol. 23, no. 10, pp. 5707-5712, 2007/05/01 2007.

[21] H. Chen, H. Muthuraman, P. Stokes, J. Zou, X. Liu, J. Wang, Q. Huo, S. I. Khondaker, and L. Zhai, "Dispersion of carbon nanotubes and polymer nanocomposite fabrication using trifluoroacetic acid as a co-solvent," *Nanotechnology,* vol. 18, no. 41, p. 415606, 2007/09/17 2007.

[22] H. M. Kim, M.-S. Choi, J. Joo, S. J. Cho, and H. S. Yoon, "Complexity in charge transport for multiwalled carbon nanotube and poly(methyl methacrylate) composites," *Physical Review B,* vol. 74, no. 5, p. 054202, 08/03/ 2006.

[23] M. S. Han, Y. K. Lee, W. N. Kim, H. S. Lee, J. S. Joo, M. Park, H. J. Lee, and C. R. Park, "Effect of multi-walled carbon nanotube dispersion on the electrical, morphological and rheological properties of polycarbonate/multi-walled carbon nanotube composites," *Macromolecular Research,* vol. 17, no. 11, pp. 863-869, 2009/11/01 2009.

[24] T. McNally, P. Pötschke, P. Halley, M. Murphy, D. Martin, S. E. J. Bell, G. P. Brennan, D. Bein, P. Lemoine, and J. P. Quinn, "Polyethylene multiwalled carbon nanotube composites," *Polymer,* vol. 46, no. 19, pp. 8222-8232, 2005/09/08/ 2005.

[25] M. Jouni, G. Boiteux, and V. Massardier, "New melt mixing polyethylene multiwalled carbon nanotube nanocomposites with very low electrical percolation threshold," *Polymers for Advanced Technologies,* vol. 24, no. 10, pp. 909-915, 2013.

[26] M. Jouni, J. Faure-Vincent, P. Fedorko, D. Djurado, G. Boiteux, and V. Massardier, "Charge carrier transport and low electrical percolation threshold in multiwalled carbon nanotube polymer nanocomposites," *Carbon,* vol. 76, pp. 10-18, 2014/09/01/ 2014.

[27] M. H. Al-Saleh, "Carbon nanotube-filled polypropylene/polyethylene blends: compatibilization and electrical properties," *Polymer Bulletin,* vol. 73, no. 4, pp. 975-987, 2016/04/01 2016.

[28] M. T. Müller, B. Krause, and P. Pötschke, "A successful approach to disperse MWCNTs in polyethylene by melt mixing using polyethylene glycol as additive," *Polymer,* vol. 53, no. 15, pp. 3079-3083, 2012/07/06/ 2012.

[29] Y.-D. Shi, J. Li, Y.-J. Tan, Y.-F. Chen, and M. Wang, "Percolation behavior of electromagnetic interference shielding in polymer/multi-walled carbon nanotube nanocomposites," *Composites Science and Technology,* vol. 170, pp. 70-76, 2019/01/20/ 2019.

[30] M. Mičušík, M. Omastová, J. Pionteck, C. Pandis, E. Logakis, and P. Pissis, "Influence of surface treatment of multiwall carbon nanotubes on the properties of polypropylene/carbon nanotubes nanocomposites," *Polymers for Advanced Technologies,* vol. 22, no. 1, pp. 38-47, 2011.

[31] S. C. Tjong, G. D. Liang, and S. P. Bao, "Electrical behavior of polypropylene/multiwalled carbon nanotube nanocomposites with low percolation threshold," *Scripta Materialia,* vol. 57, no. 6, pp. 461-464, 2007/09/01/ 2007.

[32] M.-K. Seo and S.-J. Park, "Electrical resistivity and rheological behaviors of carbon nanotubes-filled polypropylene composites," *Chemical Physics Letters,* vol. 395, no. 1, pp. 44-48, 2004/09/01/ 2004.

[33] S. H. Lee, M. W. Kim, S. H. Kim, and J. R. Youn, "Rheological and electrical properties of polypropylene/MWCNT composites prepared with MWCNT masterbatch chips," *European Polymer Journal,* vol. 44, no. 6, pp. 1620-1630, 2008/06/01/ 2008.

[34] M. T. Müller, B. Krause, B. Kretzschmar, and P. Pötschke, "Influence of feeding conditions in twin-screw extrusion of PP/MWCNT composites on electrical and mechanical properties," *Composites Science and Technology,* vol. 71, no. 13, pp. 1535-1542, 2011/09/09/ 2011.

[35] Y. Pan, L. Li, S. H. Chan, and J. Zhao, "Correlation between dispersion state and electrical conductivity of MWCNTs/PP composites prepared by melt blending," *Composites Part A: Applied Science and Manufacturing,* vol. 41, no. 3, pp. 419-426, 2010/03/01/ 2010.

[36] S. Pegel, P. Pötschke, G. Petzold, I. Alig, S. M. Dudkin, and D. Lellinger, "Dispersion, agglomeration, and network formation of multiwalled carbon nanotubes in polycarbonate melts," *Polymer,* vol. 49, no. 4, pp. 974-984, 2008/02/18/ 2008.

[37] P. Pötschke, M. Abdel-Goad, I. Alig, S. Dudkin, and D. Lellinger, "Rheological and dielectrical characterization of melt mixed polycarbonate-multiwalled carbon nanotube composites," *Polymer,* vol. 45, no. 26, pp. 8863-8870, 2004/12/01/ 2004.

[38] L. Chen, X.-J. Pang, and Z.-L. Yu, "Study on polycarbonate/multi-walled carbon nanotubes composite produced by melt processing," *Materials Science and Engineering: A,* vol. 457, no. 1, pp. 287-291, 2007/05/25/ 2007.

[39] P. Pötschke, S. M. Dudkin, and I. Alig, "Dielectric spectroscopy on melt processed polycarbonate—multiwalled carbon nanotube composites," *Polymer,* vol. 44, no. 17, pp. 5023-5030, 2003/08/01/ 2003.

[40] P. Pötschke, T. D. Fornes, and D. R. Paul, "Rheological behavior of multiwalled carbon nanotube/polycarbonate composites," *Polymer,* vol. 43, no. 11, pp. 3247-3255, 2002/05/01/ 2002.

[41] S. Maiti, N. Shrivastava, S. Suin, and B. Khatua, "A strategy for achieving low percolation and high electrical conductivity in melt-blended polycarbonate (PC)/multiwall carbon nanotube (MWCNT) nanocomposites: Electrical and thermo-mechanical properties," *Express Polymer Letters,* vol. 7, no. 6, 2013.

[42] S. H. Jin, D. K. Choi, and D. S. Lee, "Electrical and rheological properties of polycarbonate/multiwalled carbon nanotube nanocomposites," *Colloids and Surfaces A: Physicochemical and Engineering Aspects,* vol. 313-314, pp. 242-245, 2008/02/01/ 2008.

[43] P. V. Kodgire, A. R. Bhattacharyya, S. Bose, N. Gupta, A. R. Kulkarni, and A. Misra, "Control of multiwall carbon nanotubes dispersion in polyamide6 matrix: An assessment through electrical conductivity," *Chemical Physics Letters,* vol. 432, no. 4, pp. 480-485, 2006/12/11/ 2006.

[44] B. Krause, P. Pötschke, and L. Häußler, "Influence of small scale melt mixing conditions on electrical resistivity of carbon nanotube-polyamide composites," *Composites Science and Technology,* vol. 69, no. 10, pp. 1505-1515, 2009/08/01/ 2009.

[45] B. Krause, G. Petzold, S. Pegel, and P. Pötschke, "Correlation of carbon nanotube dispersability in aqueous surfactant solutions and polymers," *Carbon,* vol. 47, no. 3, pp. 602-612, 2009/03/01/ 2009.

[46] J. Z. Kovacs, B. S. Velagala, K. Schulte, and W. Bauhofer, "Two percolation thresholds in carbon nanotube epoxy composites," *Composites Science and Technology,* vol. 67, no. 5, pp. 922-928, 2007/04/01/ 2007.

[47] J. Li, P. C. Ma, W. S. Chow, C. K. To, B. Z. Tang, and J.-K. Kim, "Correlations between Percolation Threshold, Dispersion State, and Aspect Ratio of Carbon Nanotubes," *Advanced Functional Materials,* vol. 17, no. 16, pp. 3207-3215, 2007.

[48] A. Moisala, Q. Li, I. A. Kinloch, and A. H. Windle, "Thermal and electrical conductivity of single- and multi-walled carbon nanotube-epoxy composites," *Composites Science and Technology,* vol. 66, no. 10, pp. 1285-1288, 2006/08/01/ 2006.

[49] C. A. Martin, J. K. W. Sandler, M. S. P. Shaffer, M. K. Schwarz, W. Bauhofer, K. Schulte, and A. H. Windle, "Formation of percolating networks in multi-wall carbon-nanotube–epoxy composites," *Composites Science and Technology,* vol. 64, no. 15, pp. 2309-2316, 2004/11/01/ 2004.

[50] J. Sandler, M. S. P. Shaffer, T. Prasse, W. Bauhofer, K. Schulte, and A. H. Windle, "Development of a dispersion process for carbon nanotubes in an epoxy matrix and the resulting electrical properties," *Polymer,* vol. 40, no. 21, pp. 5967-5971, 1999/10/01/ 1999.

[51] S.-M. Yuen, C.-C. M. Ma, H.-H. Wu, H.-C. Kuan, W.-J. Chen, S.-H. Liao, C.-W. Hsu, and H.-L. Wu, "Preparation and thermal, electrical, and morphological properties of multiwalled carbon nanotubeand epoxy composites," *Journal of Applied Polymer Science,* vol. 103, no. 2, pp. 1272-1278, 2007.

[52] J. K. W. Sandler, J. E. Kirk, I. A. Kinloch, M. S. P. Shaffer, and A. H. Windle, "Ultra-low electrical percolation threshold in carbon-nanotube-epoxy composites," *Polymer,* vol. 44, no. 19, pp. 5893-5899, 2003/09/01/ 2003.

[53] F. H. Gojny, M. H. G. Wichmann, B. Fiedler, I. A. Kinloch, W. Bauhofer, A. H. Windle, and K. Schulte, "Evaluation and identification of electrical and thermal conduction mechanisms in carbon nanotube/epoxy composites," *Polymer,* vol. 47, no. 6, pp. 2036-2045, 2006/03/08/ 2006.

[54] Z. Khattari, M. Maghrabi, T. McNally, and S. Abdul Jawad, "Impedance study of polymethyl methacrylate composites/multi-walled carbon nanotubes (PMMA/MWCNTs)," *Physica B: Condensed Matter,* vol. 407, no. 4, pp. 759-764, 2012/02/15/ 2012.

[55] E. Logakis, C. Pandis, P. Pissis, J. Pionteck, and P. Pötschke, "Highly conducting poly(methyl methacrylate)/carbon nanotubes composites: Investigation on their thermal, dynamic-mechanical, electrical and dielectric properties," *Composites Science and Technology,* vol. 71, no. 6, pp. 854-862, 2011/04/12/ 2011.

[56] Y. Pan, X. Liu, J. Kaschta, X. Hao, C. Liu, and D. W. Schubert, "Viscoelastic and electrical behavior of poly(methyl methacrylate)/carbon black composites prior to and after annealing," *Polymer,* vol. 113, pp. 34-38, 2017/03/24/ 2017.

[57] R. L. Muhlbauer, T. L. Pruyn, W. T. Puckett, and R. A. Gerhardt, "Effect of graphitic filler size and shape on the microstructure, electrical percolation behavior and thermal properties of nanostructured multilayered carbon films deposited onto paper substrates," *Journal of Materials Research,* vol. 29, no. 3, pp. 472-484, 2014.

[58] M. R. Watt and R. A. Gerhardt, "Effect of β-Silicon Carbide Size and Shape on the Properties and Microstructure of PMMA Matrix Nanocomposites," *TechConnect Briefs,* vol. 4, Advanced Manufacturing, Electronics and Microsystems: TechConnect Briefs 2016, pp. 11-15, May 22, 2016 2016.

[59] Y. Jin and R. A. Gerhardt, "Prediction of the Percolation Threshold and Electrical conductivity of Self-Assembled Antimony-Doped Tin Oxide Nanoparticles into Ordered Structures in PMMA/ATO Nanocomposites," *ACS Applied Materials & Interfaces,* vol. 6, no. 24, pp. 22264-22271, 2014/12/24 2014.

[60] J. Waddell, R. Ou, C. J. Capozzi, S. Gupta, C. A. Parker, R. A. Gerhardt, K. Seal, S. V. Kalinin, and A. P. Baddorf, "Detection of percolating paths in polyhedral segregated network composites using electrostatic force microscopy and conductive atomic force microscopy," *Applied Physics Letters,* vol. 95, no. 23, p. 233122, 2009.

[61] C. J. Capozzi, S. Shackelford, R. Ou, and R. A. Gerhardt, "Study of Percolation in PMMA / Indium Tin Oxide Composites," *MRS Proceedings,* vol. 819, p. N3.13, 2004, Art. no. N3.13.

[62] M. R. Watt and R. A. Gerhardt, "A Study of the Effect of Mixing Method and Particle Size on Polymer Composites," presented at the Materials Science and Technology 2019, Portland, OR, 2019.

[63] L. Prystaj, E. A. Lucas, K. Alston, and R. A. Gerhardt, "Effect of Graphitic Filler Characteristics on the Percolation Behavior and Electrical Conductivity of Segregated Network Polymer Composites," *TechConnect Briefs,* vol. 1, Advanced Materials: TechConnect Briefs 2016, pp. 149-152, May 22, 2016 2016.

[64] W. Cao and R. Gerhardt, "Calculation of various relaxation times and conductivity for a single dielectric relaxation process," *Solid State Ionics,* vol. 42, no. 3, pp. 213-221, 1990/10/01/ 1990.

[65] R. A. Gerhardt, "Impedance Spectroscopy and Mobility Spectra," in *Encyclopedia of Condensed Matter Physics*, ed. London: Elsevier, 2005, pp. 350–363.

[66] R. Gerhardt, "Impedance and dielectric spectroscopy revisited: Distinguishing localized relaxation from long-range conductivity," *Journal of Physics and Chemistry of Solids,* vol. 55, no. 12, pp. 1491-1506, 1994/12/01/ 1994.

[67] T. L. Pruyn and R. A. Gerhardt, "Detection of Different Interfaces in Percolated Networks of Antimony Tin Oxide: Borosilicate Glass Composites by Impedance Spectroscopy," *Journal of the American Ceramic Society,* vol. 98, no. 1, pp. 154-162, 2015.

[68] J. R. Macdonald and W. B. Johnson, "Fundamentals of Impedance Spectroscopy," in *Impedance Spectroscopy: Theory, Experiment, and Applications*, Y. Barsukov and J. Macdonald, Eds. 2nd ed. Wiley, 2005.

[69] S. Zhang, N. Nguyen, B. Leonhardt, C. Jolowsky, A. Hao, J. G. Park, and R. Liang, "Carbon-Nanotube-Based Electrical Conductors: Fabrication, Optimization, and Applications," *Advanced Electronic Materials,* vol. 5, no. 6, p. 1800811, 2019.

[70] E. Logakis, C. Pandis, V. Peoglos, P. Pissis, J. Pionteck, P. Pötschke, M. Mičušík, and M. Omastová, "Electrical/dielectric properties and conduction mechanism in melt processed polyamide/multi-walled carbon nanotubes composites," *Polymer,* vol. 50, no. 21, pp. 5103-5111, 2009/10/09/ 2009.

[71] S. Zhang, N. Nguyen, J. G. Park, A. Hao, and R. Liang, "Chapter 14 - Carbon Nanotubes and Their Assemblies: Applications in Electromagnetic Interference Shielding," in *Nanotube Superfiber Materials (Second Edition)*, M. J. Schulz, V. Shanov, Z. Yin, and M. Cahay, Eds.: William Andrew Publishing, 2019, pp. 335-357.

[72] *Thermal properties*. Available: http://www.ioffe.ru/SVA/NSM/Semicond/SiC/thermal.html

[73] *Silar Microwave Flatstone*. Available: http://www.silarwave.com/product_fs.html

[74] J. R. Brandt and R. A. Gerhardt, "Assessment of Homogeneity of Extruded Alumina-SiC Composite Rods Used in Microwave Heating Applications by Impedance Spectroscopy," *MRS Proceedings,* vol. 1538, pp. 323-328, 2013.

[75] *Silicon carbide*. Available: https://en.wikipedia.org/wiki/Silicon_carbide

[76] Y. Jin, "Composites Containing Percolated Networks and/or Core-Shell Structures Useful for Microsystems Applications," PhD, Materials Science and Engineering, Georgia Institute of Technology, 2016.

[77] R. J. Andrews and E. A. Grulke, *Polymer handbook*, 4th ed. New York: Wiley, 1999.

[78] H. Kobayashi, H. Takahashi, and Y. Hiki, "Viscosity measurement of organic glasses below and above glass transition temperature," *Journal of Non-Crystalline Solids,* vol. 290, no. 1, pp. 32-40, 2001/09/01/ 2001.

[79] J. E. Shelby, *Introduction to Glass Science and Technology*. Royal Society of Chemistry, 2005.

[80] T. Rudzik, "Effect Of Process Variables And Sintering Method On The Microstructure And Properties Of ITO/ borosilicate Glass Composites," PhD dissertation, Materials Science and Engineering, Georgia Institute of Technology, 2019.

[81] T. Rudzik, ed, 2019.

[82] T. L. Pruyn and R. A. Gerhardt, "Fabrication and Characterization of Conductive Glass Composites with Networks of Silicon Carbide Whiskers," in *Processing and Properties of Advanced Ceramics and Composites VI*, I. John Wiley & Sons, Ed. Hoboken, 2014, pp. 27-36.

[83] R. Wu, K. Zhou, Z. Yang, X. Qian, J. Wei, L. Liu, Y. Huang, L. Kong, and L. Wang, "Molten-salt-mediated synthesis of SiC nanowires for microwave absorption applications," *CrystEngComm,* 10.1039/C2CE26510A vol. 15, no. 3, pp. 570-576, 2013.

[84] *Malvern PANalytical Empyrean*. Available: https://mcf.gatech.edu/tools/panalytical-empyrean/

[85] *Scanning Electron Microscope, SEM (Phenom ProX) with Elemental Analysis (Energy Dispersive X-ray Analysis – EDX)*. Available: https://mill.mse.gatech.edu/equipment-teams/characterization-team-updated/

[86] J. Ilavsky, G. G. Long, A. J. Allen, and C. C. Berndt, "Evolution of the void structure in plasma-sprayed YSZ deposits during heating," *Materials Science and Engineering: A,* vol. 272, no. 1, pp. 215-221, 1999/11/15/ 1999.

[87] G. Long, S. Krueger, P. R. Jemian, D. Black, H. E. Burdette, J. P. Cline, and R. Gerhardt, "Small-Angle-Scattering Determination of the Micro-structure of Porous Silica Precursor Bodies," *Journal of Applied Crystallography - J APPL CRYST,* vol. 23, pp. 535-544, 12/01 1990.

[88] A. J. Allen, "Characterization of Ceramics by X-Ray and Neutron Small-Angle Scattering," *Journal of the American Ceramic Society,* vol. 88, no. 6, pp. 1367-1381, 2005.

[89] F. Peyronel and D. A. Pink, "Chapter 9 - Ultra-Small Angle X-ray Scattering: A Technique to Study Soft Materials," in *Structure-Function Analysis of Edible Fats (Second Edition)*, A. G. Marangoni, Ed.: AOCS Press, 2018, pp. 267-285.

[90] J. Ilavsky and P. R. Jemian, "Irena: tool suite for modeling and analysis of small-angle scattering," *Journal of Applied Crystallography,* vol. 42, no. 2, pp. 347-353, 2009.

[91] R. J. Iwanowski, K. Fronc, W. Paszkowicz, and M. Heinonen, "XPS and XRD study of crystalline 3C-SiC grown by sublimation method," *Journal of Alloys and Compounds,* vol. 286, no. 1, pp. 143-147, 1999/05/05/ 1999.

[92] D.-H. Wang, D. Xu, Q. Wang, Y.-J. Hao, G.-Q. Jin, X.-Y. Guo, and K. N. Tu, "Periodically twinned SiC nanowires," *Nanotechnology,* vol. 19, no. 21, p. 215602, 2008/04/21 2008.

[93] Y.-F. Zhu, C. Ma, W. Zhang, R.-P. Zhang, N. Koratkar, and J. Liang, "Alignment of multiwalled carbon nanotubes in bulk epoxy composites via electric field," *Journal of Applied Physics,* vol. 105, no. 5, p. 054319, 2009.

[94] T. J. Rudzik and R. A. Gerhardt, "Effect of Spark Plasma Sintering Current and Voltage on the Microstructure and Electrical Properties of Borosilicate Glass–Indium Tin Oxide Composites," *Advanced Engineering Materials,* vol. 22, no. 5, p. 1901431, 2020.

[95] R. L. Muhlbauer, "Investigation Of The Structure-Property-Processing Relationships In Paper And Carbon Nanotube Composite Materials," Doctor of Philosophy, School of Materials Science and Engineering, Georgia Institute of Technology, 2014.

[96] B. D. Bertram, R. A. Gerhardt, and J. W. Schultz, "Impedance response and modeling of composites containing aligned semiconductor whiskers: Effects of dc-bias partitioning and percolated-cluster length, topology, and filler interfaces," *Journal of Applied Physics,* vol. 111, no. 12, p. 124913, 2012.

[97] G. Zhang, "Effects of Alkali Ions on the Dielectric Properties of Porous Silica Prepared by a Colloidal Processing Method," Master, Georgia Institute of Technology, 1993.